NATURAL SCIENCE REVIEW 3 200605 (2026)
nsr.jinr.int

Computational schemes based on the continuous analogue of Newton's method in the numerical study of complex physical systems at JINR

E. V. Zemlyanaya* [1,2,3] and O. Chuluunbaatar† [1,4,5]

[1] *Joint Institute for Nuclear Research, 141980 Dubna, Russia*
[2] *Dubna State University, 141980 Dubna, Russia*
[3] *Branch of Lomonosov Moscow State University in Dubna, 141980 Dubna, Russia*
[4] *Institute of Mathematics and Digital Technology, Mongolian Academy of Sciences, 13330 Ulaanbaatar, Mongolia*
[5] *School of Applied Sciences, Mongolian University of Science and Technology, 14191 Ulaanbaatar, Mongolia*

Abstract

The Continuous analogue of Newton's method (CANM), developed at JINR since the 1970s, is one of the most important areas of research at Laboratory of Computing Techniques and Automation (LCTA) — Meshcheryakov Laboratory of Information Technologies (MLIT). CANM and its generalization are powerful tools for the effective numerical solution of nonlinear problems within a wide range of complex physical systems studied at JINR. This review article provides a general framework for the CANM-based approach, the main stages in the development and applications of CANM for solving various types of nonlinear problems that have been on the agenda in different years. The results of the development and application of CANM-based iterative methods, obtained over the past 20 years, are presented in more detail.

Keywords: Newtonian iteration, computer modeling, nonlinear problem, complex physical system

DOI: 10.54546/NaturalSciRev.200605

Contents

*Corresponding author e-mail address: elena@jinr.ru
†Corresponding author e-mail address: chuka@jinr.ru

Received: 12 January 2026; Revised: 17 January 2026; Accepted: 26 January 2026; Published: 12 March 2026

1. Introduction: historical preamble and our days

One of the most important research areas at LCTA-MLIT is the development and application of computational schemes based on the Continuous analogue of Newton's method (CANM). CANM and its generalization provide broad capabilities for constructing computational schemes that flexibly address the specific needs of specific problems arising in the mathematical modeling of complex systems in nuclear physics, quantum mechanics, condensed matter physics,

astrophysics, and other fields of science. The CANM approach ensures a rapid convergence and high accuracy of the resulting numerical solutions.

At present, the term "Continuous analogue of Newton's method" and the abbreviation CANM are used in a broad sense, encompassing the entire set of computational schemes based on "classical" CANM formulated in [1], its generalization [2] and its various modifications in combination with other numerical methods.

For many years, the recognized leader of this field, heading the theoretical development of CANM and its generalization, as well as work on the use of Newtonian iterative schemes for the numerical study of a number of nonlinear physical systems at MLIT and JINR, was the honored scientist, Professor Igor Viktorovich Puzynin.

The theoretical study and practical use of CANM-based iteration schemes started at LCTA with the publication of the paper by E. P. Zhidkov and I. V. Puzynin [3] in 1967, where a modified Newton-type process with the introduction of an auxiliary continuous parameter was considered and successfully employed for the numerical solution of a boundary value problem (BVP) for a nonlinear differential equation. Since then, such a numerical approach (termed by the "Continuous analogue of Newton's method" similar to [4], where a consideration of standard iterative method continuous analogues was proposed) was intensively developed by scientists at LCTA in collaboration with colleagues from the other Laboratories of JINR. The long-term practical use of the CANM approach in the computational analysis of various problems confirmed its effectiveness and yielded new knowledge within the relevant areas of nuclear physics, quantum mechanics, and condensed matter physics. Most achievements in the development and application of CANM in 1967–2007 were summarized in review papers [1, 2, 5] published in 1973, 1999, and 2007.

In the first review article [1] published in 1973 by E. P. Zhidkov, G. I. Makarenko, and I. V. Puzynin, the convergence properties of CANM iterations for several classes of nonlinear problems, including the Dirichlet problem for a quasi linear elliptic equation, a nonlinear integral equation, a nonlinear equation within the inverse scattering problem, a BVP for a nonlinear differential equation within the statistical nuclear physics model, are considered.

In the following years, CANM-based computational schemes were elaborated and successfully employed at the Department of Computational Mathematics of LCTA headed by E. P. Zhidkov for the numerical analysis of nonlinear problems arising within the mathematical description of a wide range of complex physical systems.

The paper [6], where a modified CANM-based iteration method is considered for the eigenvalue problem of an integro-differential equation, is noteworthy. In [7], the CANM iteration scheme is constructed and applied to calculate single-particle quasi stationary states in spherical and deformed nuclei. In [8], the numerical solution of a quantum-mechanical scattering problem is reduced to the CANM-based numerical solution of the respective eigenvalue problem. In [9], CANM-based computational schemes are considered for numerically solving singular BVPs within the models of quantum mechanics and quantum field theory. The papers [10–12] consider CANM-based approaches for solving various multi-channel and multi-dimensional scattering problems. In [13], the CANM numerical scheme is used in the numerical analysis of solitons and critical currents within the model of Josephson junctions with microinhomogeneities. A CANM-based numerical study of the stability of moving bubble-like solutions in a system of interacting bosons was performed in [14].

An important direction in 1975–1990 was the development and application of numerical methods for solving the quantum-mechanical three-body problem within the muon catalysis theory [15]. A series of studies were conducted on the development of new methods for the

numerical solution of the singular Sturm-Liouville problem for systems of a large number of integro-differential Schrödinger equations. Algorithms and computer programs on the basis of CANM were successfully applied to high-precision calculations of the physical characteristics of mesomolecular and nuclear processes. The numerically predicted energy levels of weakly bound states of mesomolecules $dd\mu$ and $dt\mu$ were confirmed by experiments performed at the Dzhelepov Laboratory of Nuclear Problems of JINR. The accuracy of the numerical results was comparable to the accuracy of particle mass measurements available at that time. These results were a basis for further investigations of the muon catalysis process within other theoretical and numerical approaches. In 1986, the participants of the investigations D. D. Bakalov, S. I. Vinitsky, A. D. Gocheva, M. S. Kaschiev, V. I. Korobov, V. S. Melezhik, I. V. Puzynin, T. P. Puzynina, L. N. Somov, and N. F. Truskova were awarded the JINR Prize for the project "Creation of methods for solving the quantum-mechanical three-body problem and their application to the problem of muon catalysis of nuclear fusion reactions". The discovery of weakly bound states in the muonic molecules of deuterium and tritium [16–18] is one of the world-class achievements at JINR, made possible by the use of the CANM method. The mathematical and physical contexts of this problem, details of the numerical approach, results of the calculations, and respective references are presented in [5].

Another area of application of the CANM approach is the numerical study of multi-parameter self-consistent nonlinear models, such as the polaron model, solvated electron model, quantum-field binucleon model, QCD-inspired quarkonium model, and others. Stationary particle-like states in these models are found by means of the numerical solution of singular BVPs and spectral problems for systems of nonlinear multi-parameter differential, integro-differential and integral equations. In these numerical studies, modified computational schemes were employed on the basis of the generalization of "classical" CANM. As shown in the theoretical analysis of I. V. Puzynin and T. Zhanlav [19] and in the numerical studies of I. V. Puzynin, P. G. Akishin, I. V. Amirkhanov, T. P. Puzynina, Yu. S. Smirnov, T. A. Strizh, E. V. Zemlyanaya, and T. Zhanlav, generalized CANM improves the convergence of the iteration process for these classes of nonlinear problems and opens additional possibilities in constructing high accuracy computational schemes [12]. These results are discussed in detail in the second review paper [2].

The most recent review article [5] was published in 2007 and discusses new numerical approaches based on the combination of CANM and generalized CANM with other methods in the context of the numerical investigation of a wide range of complex physical systems. The results of I. V. Puzynin, I. V. Barashenkov, T. L. Boyadzhiev, O. Chuluunbaatar, T. P. Puzynina, O. I. Streltsova, S. I. Vinitsky, E. V. Zemlyanaya, and others on the investigation of numerous physical systems, including the calculation of energy levels within the adiabatic mesomolecule model, the numerical solution of a scattering problem within three-particle systems, the analysis of the existence and stability of multi-soliton complexes and travelling waves in the damped-driven nonlinear Schorödinger equation with self-focusing and de-focusing nonlinearity, the investigation of instabilities of spinor solitons, critical regimes in nonlinear models of astrophysics and Josephson junction systems, are presented.

In 2007–2025, the research continues in both directions of improving CANM iterative schemes and extending the application of CANM in the numerical analysis of various problems within thematic projects at JINR and its Member States.

New algorithms for calculating the CANM iteration parameter [20, 21], aimed at achieving a faster convergence of CANM-based iterations, were proposed by I. V. Puzynin, T. P. Puzynina, and V. T. Thach, and their effectiveness in solving a number of problems was demonstrated. Another algorithm for the CANM iteration parameter was proposed by T. Zhanlav and O. Chu-

luunbaatar for the CANM-based solution of an eigenvalue problem for a system of differential equations. Two- and three-step iteration processes within the CANM approach were developed by T. Zhanlav and O. Chuluunbaatar and proved to be effective for special classes of nonlinear problems. The convergence of the CANM process for iteration parameter values greater than 1 was also considered, and the corresponding convergence theorem was proved. These studies were performed within collaboration between JINR and the Institute of Mathematics and Digital Technology of the Mongolian Academy of Sciences and published in the monograph [22].

The combined use of the CANM iteration with the predictor-corrector continuation technique and Numerov's finite-difference approximation made it possible to obtain and investigate new localised states in systems described by various versions of the damped-driven nonlinear Schrödinger equation, including travelling multisoliton complexes [23], time-periodic and quasiperiodic localised structures [24, 25]. Later, the corresponding numerical approaches were adapted and are used for the numerical study of three-dimensional oscillons in the ϕ^4 theory based on their approximation by standing waves in a ball of finite radius [26]. These studies were conducted by E. V. Zemlyanaya, N. A. Alexeeva, I. V. Barashenkov, and others within collaboration between JINR and the University of Cape Town.

CANM-based computational schemes, developed previously by T. L. Boyadzhiev and coauthors, were extended for the numerical study of the complexity of coexisting multifluxon states in the long Josephson junction system within a model based on the double sine-Gordon equation [27–31]. These studies were conducted in collaboration with Bulgarian colleagues, as well as with colleagues from the Bogoliubov Laboratory of Theoretical Physics of JINR (P. Kh. Atanasova, T. L. Boyadzhiev, Yu. M. Shukrinov, E. V. Zemlyanaya, and others).

Computational schemes with the use of the finite element method (FEM) within the CANM iteration were elaborated and employed by O. Chuluunbaatar, A. A. Gusev, S. I. Vinitsky, and others for the numerical study of several models of few-particle systems in multidimensional domains with complex boundary geometry [32–36].

I. V. Puzynin, I. G. Hristov, and others proposed modified iterative schemes based on the CANM method and Taylor expansion, which made it possible to obtain new families of solutions of a special type to the three- body problem on a plane with high accuracy (see, i.e. [37, 38]). Based on CANM, an algorithm for the mathematical modeling of charged particle transport in accelerators was developed in [39]. In [40], the CANM-based approach is used within the context of point approximation in three-dimensional space by a set of parallel planes based on the orthogonal least squares method. Furthermore, the CANM approach and the NINE program [41] is used in the recent work [42] for the numerical solution of a nonlinear BVP arising in theoretical studies of scalar vortex generation in a rotational frame.

Despite the wide range of practical applications of CANM, the most significant results were obtained in two major areas: the numerical study of problems arising within the few-body models of nuclear physics and quantum mechanics, and the study of particle-like states and localised structures within the nonlinear models of field theory and quantum field theory. Taking this into account, this article is organised as follows. In Section 2, the general principles of constructing iteration schemes based on CANM are considered. New variants of choice of the CANM iteration parameter are also discussed in Section 2. In Sections 3 and 4, representative cases of CANM-based numerical studies of localised structures in nonlinear media and investigations of complex few-body systems over the past twenty years are presented.

2. Modified iterations on the basis of CANM and its generalization

The mathematical modeling of complex physical systems typically results in non-stationary, spatially non-one-dimensional, multi-parameter, nonlinear, singular systems of integral, integro-differential, or differential equations. In practice, for theoretical and numerical studies of such systems, one way or another, a transition to simpler formulations occurs [2, 5]. In some, relatively few cases, it is possible to make theoretical estimates of the accuracy of the aforementioned simplifications. In other cases, to assess the accuracy and reliability of the obtained numerical results, it is necessary to conduct comparative calculations on a sequence of expanding intervals, condensing grids, an increasing number of basis functions, etc. Thus, in many cases, the numerical study of models of complex physical systems can be reduced to solving multi-parameter BVPs for stationary systems of equations of various types and to spectral problems for such systems. Their characteristic feature remains nonlinearity (and hence the possible non-uniqueness of the solution and the presence of bifurcations), as well as multi-parametricity.

Such problems can be uniformly formulated as a nonlinear functional equation [5]:

$$F(\boldsymbol{a}, \Psi) = 0, \tag{1}$$

where $\boldsymbol{a} \in \mathcal{R}_l$ is the vector of parameters of the physical model, Ψ is an element from some region of the Banach space $\mathcal{Y}$, and $\mathcal{R}_l$ is the Euclidean space of the dimension l. The nonlinear function F, given the vector of parameters $\boldsymbol{a}$, maps the elements Ψ from the region of $\mathcal{Y}$ to $\mathcal{U}$, where $\mathcal{U}$ is the Banach space and $\mathcal{U} \supseteq \mathcal{Y}$. In spectral problems $\Psi = \{\boldsymbol{\lambda}, y\}$, where y is an element from some region of Banach space $\mathcal{Y}$, and $\boldsymbol{\lambda} \in \mathcal{R}_m$ is the vector of eigenvalues. The nonlinear function F maps the elements Ψ from the region of $\mathcal{R}_m \times \mathcal{Y}$ to $\mathcal{R}_m \times \mathcal{U}$.

The problems under consideration are characterized by the following features noted in [2, 5].

- Some preliminary information about the existence and qualitative behavior of the desired solutions is known from the physical properties of the processes under study and from the consideration of simplified models, especially in asymptotic ranges of parameter variation
- In problems representing approximations to more complex multidimensional problems, as well as when moving from infinite to finite ranges of independent variables, problems in estimating the accuracy of the approximations used arise. In most cases, such estimates can only be obtained numerically, by performing calculations for certain values of the approximation parameters.

Thus, in formulation (1), the vector of "external" parameters $\boldsymbol{a}$ expands and, in addition to the "physical" parameters of the model, contains the approximation parameters of the problem, including those of the computational scheme. Therefore, a numerical study always embraces checking the adequacy of the selected discrete approximation parameters and verifying the theoretical and actual accuracy of the computational scheme. As a result, a numerical study of a model typically involves conducting large-scale calculations over a wide range of these parameters. This enables, on the one hand, to study the properties of the models under consideration, i.e., the behavior of solutions depending on the "physical" parameters, and, on the other hand, to control the accuracy of the obtained results depending on the approximation parameters of the original problems.

Modified schemes based on CANM and its generalizations are an effective method for numerically solving a wide range of problems of type (1) for the given parameter vector $\boldsymbol{a}$. This method, while maintaining the quadratic convergence of iterations in the vicinity of a local root, allows one, by choosing the iteration parameter, to expand the convergence region of Newtonian

iterations compared to the "classical" Newton method. The simple logic of constructing schemes based on the CANM generalization, on the one hand, and the flexibility of this approach, which allows it to be combined with other computational methods, thereby taking into account the specifics of a particular problem and the architectural features of modern computing systems, on the other hand, make it a powerful and widely used tool in computational physics.

As already mentioned, multi-parametricity is a characteristic feature of the problems under study, making it relevant to develop methods of continuation by parameters, taking into account the specific characteristics of specific problems and research objectives. Combining CANM with new efficient continuation schemes, ensures a stable convergence of Newtonian iterations and provides a promising basis for successful numerical studies of the functional dependencies of solutions on parameters in nonlinear multi-parameter models of complex systems [5].

Since the development of the CANM approach is largely a product of experience in solving a variety of practical problems, the schemes developed based on it reflect the most attractive aspects of several other well-known methods widely used in solving physics problems. These are perturbation theory schemes [43], the parameter continuation method [44], and the parameter differentiation method [45] (in nuclear physics problems, this method is known as the coupling constant evolution method [46]). As a result, the developed computational schemes possess the properties of such well-known methods as the splitting method [47], multigrid methods [48], and some regularization methods [49].

Iterative schemes based on the CANM generalization, while maintaining the quadratic convergence of iterations in the region of a local root, make it possible, by choosing the iteration parameter, to expand the region of convergence of Newtonian iterations (the "bottleneck" of the classical Newton method).

In the iterative schemes developed on the basis of the CANM generalization, the problem of choosing initial approximations is constructively solved for certain classes of problems. The solution of a linear problem with respect to iterative corrections is simplified, i.e., the iterative process without inverting the linear operator in this problem.

In spectral problems of quantum mechanics, the developed generalization of CANM can serve as a unified theoretical basis for describing a number of well-known methods, such as the inverse iteration method, the inverse iteration method with a shift, and the inverse iteration method with a Rayleigh quotient [50]. Computational schemes for problems of this type are discussed in reviews [51, 52], see also [2, 5] for details and references.

2.1. CANM iteration process

In [4], a group of one-step iterative methods for solving a nonlinear equation in Banach space is considered[1]

$$F(\Psi) = 0, \tag{2}$$

in which, at each step k of the iteration process, the correction $\Delta\Psi_k$ to the approximation Ψ_k of the desired solution known from the previous step is calculated by the formula

$$\Delta\Psi_k = \psi(\Psi_k), \quad \Psi_{k+1} = \Psi_k + \Delta\Psi_k, \quad k = 0, 1, 2, \ldots,$$

where Ψ_0 is a given element. The method for constructing the function $\psi(\Psi)$ is determined depending on the iterative method used. In particular, for Newton's method

$$\psi(\Psi) = -(F'(\Psi))^{-1} F(\Psi),$$

[1]In those formulas where it is not essential, the dependence of the function $F(\boldsymbol{a}, \Psi)$ on $\boldsymbol{a}$ is omitted.

where $F'(\Psi)$ is a linear operator, the Fréchet derivative of the function $F(\Psi)$. It is shown that for each iterative process of this type, a continuous analogue can be constructed by replacing the discrete variable k ($k = 0, 1, 2, \ldots$) with the continuous parameter t ($0 \leqslant t < \infty$). Assuming the continuous dependence $\Psi = \Psi(t)$ and introducing the derivative $d\Psi(t)/dt$ instead of the increment $\Delta\Psi_k$, a differential equation is obtained

$$\frac{d}{dt}\Psi(t) = \psi(\Psi(t)), \quad \Psi(0) = \Psi_0, \tag{3}$$

and then

$$\frac{d}{dt}F(\Psi(t)) = -F(\Psi(t)), \quad \Psi(0) = \Psi_0 \tag{4}$$

This implies the existence of the integral $F(\Psi(t)) = e^{-t}F(\Psi_0)$ which converges to the solution Ψ^* as $t \to \infty$ [4].

As a result, finding a solution to Eq. (2) is accomplished by solving the Cauchy problem (3) on the semiaxis $0 \leqslant t < \infty$. In [4], a number of assertions regarding the convergence of continuous analogues of iterative methods for $t \to \infty$ to the isolated solution Ψ^* of Eq. (2) are proved.

The review [1] describes the simplest one-step method for the approximate integration of problem (3), which is the Euler method for CANM. This method on a discrete grid $\{t_k, k = 0, 1, 2, \ldots; t_{k+1} - t_k = \tau_k\}$ leads to a sequence of linear problems

$$F'(\Psi_k)v_k = -F(\Psi_k), \quad \Psi_{k+1} = \Psi_k + \tau_k v_k, \quad k = 0, 1, 2, \ldots, \tag{5}$$

where Ψ_0 is a given element. For $\tau_k \equiv 1$, the result is a sequence of iterations of Newton's method. The convergence conditions of the iteration process (5) are considered in [3].

In the practical implementation of Newtonian iterative schemes, Eq. (2) is replaced by an equation approximating it in the grid space

$$F_h(\Psi_h) = 0. \tag{6}$$

Let Ψ_h^* be the exact solution of Eq. (6). Then, in the grid norm, the following estimate is valid:

$$\|\Psi^* - \Psi_h^k\| \leqslant \|\Psi^* - \Psi_h^*\| + \|\Psi_h^* - \Psi_h^k\|, \tag{7}$$

where Ψ_h^k is the approximation to the solution obtained after the k-th iteration under the condition

$$\delta_k = \|F_h(\Psi_h^k)\| \leqslant \varepsilon, \quad 0 < \varepsilon \ll 1. \tag{8}$$

Since

$$\|\Psi^* - \Psi_h^*\| \leqslant O(h^p) \quad \text{and} \quad \|\Psi_h^* - \Psi_h^k\| \leqslant \tilde{B}\|F_h(\Psi_h^k)\|,$$

where $\tilde{B} > 0$ is a constant that determines the neighborhood of the desired solution [53], then for $\tilde{B}\|F_h(\Psi_h^k)\| \ll O(h^p)$ (which is satisfied by specifying sufficiently small ε in relation (8)), the accuracy of the obtained approximate solution is close to the theoretical estimate of the chosen difference approximation method for Eq. (2):

$$\|\Psi^* - \Psi_h^k\| \sim O(h^p). \tag{9}$$

This can be studied in detail on a sequence of condensing grids. In this case, it is possible to refine the difference solution using Padé or Richardson extrapolation (see, for example, [48]).

If the original problem is singular, a term characterizing the error in approximating the singular problem by the corresponding regular problem is added to the accuracy estimate. This error can be estimated by performing successive calculations on expanding intervals. In this case, a ratio of the computational scheme parameters is achieved such that the error in the difference solution accounts for the main contribution, i.e., so that relation (9) is satisfied.

It is known [54] that the stability and convergence of the difference solution of a nonlinear BVP are closely related to the approximation properties of the corresponding linearized problem. The construction of an almost extremely compact $O(h^4)$ accuracy scheme within Newtonian iterations, approximating the linear problem for inverting the Fréchet derivative operator, enables us to expect the stability of such a scheme. Then, under conditions of sufficient smoothness (Lipschitz condition) of the coefficients of the linearized problem, the corresponding finite-difference scheme for the nonlinear BVP has, in the neighborhood of the exact isolated solution of the differential problem, a unique solution for sufficiently small h that converges to this solution (such schemes are implemented, for example, in the SLIPH4 [55] and PROGS2H4 [56] programs).

Thus, three factors that determine the convergence properties and accuracy of the CANM iteration process should be selected taking into account special features of each nonlinear problem: the choice of the initial guess; the algorithm of the iteration parameter calculation; the method and accuracy of calculating the inverse operator to the Fréchet derivative.

2.2. Iteration parameter in CANM

The choice of the parameter τ_k can be accomplished in different ways and presents a special problem. As a result of practical experience and theoretical research by a number of authors [53, 54, 57–59], several algorithms for calculating this parameter are developed, expanding the region of the CANM convergence and reducing the number of Newtonian iterations.

The algorithm proposed in [59] is defined by the formula

$$\tau_k = \frac{\tilde{\delta}_{k-1}}{\tilde{\delta}_{k-1} + \tilde{\delta}_k(1)}, \tag{10}$$

where

$$\tilde{\delta}_k = \|F_h(\Psi_h^k)\|^2, \tag{11}$$

and $\tilde{\delta}_k(1)$ is the value of $\tilde{\delta}_k$ at the k-th iteration calculated in the case $\tau = 1$. As shown in [59], this algorithm ensures a quadratic reduction in the residual $\tilde{\delta}$ and the convergence of the iterative process in a small number of steps in the case of a well-chosen initial approximation. Its drawback is the need to calculate the value of $\tilde{\delta}_k(1)$ at each iteration, which, when solving complex problems (integro-differential equations, spatially multi-dimensional systems of equations, etc.), can require a significant increase in computation time.

In [53], the local convergence of iterations (5) is proved in the case of the iteration parameter calculation by means of the formula:

$$\tau_k = \begin{cases} \min\left(1, \tilde{\tau}_k\right), & \text{for} \quad \|F(\Psi_k)\| < \|F(\Psi_{k-1})\|, \\ \max\left(\tau_0, \tilde{\tau}_k\right), & \text{for} \quad \|F(\Psi_k)\| \geqslant \|F(\Psi_{k-1})\|, \end{cases} \tag{12}$$

where $\tilde{\tau}_k = \|F(\Psi_k)\|^{-1}\|F(\Psi_{k-1})\|\tau_{k-1}$. As shown in [53], algorithm (12) provides a sequence of $\{\tau_k\}$ close to optimal and, at a certain stage, the transformation of the CANM process (5)

to the classical Newton method. It is also demonstrated in [53] that the convergence region of CANM-based iterations with this choice of τ_k is wider than that of the classical Newton method. In particular, practical calculations confirm that by decreasing the value of τ_0 in (12), one can expand the convergence region of CANM-based iterations. On the other hand, increasing τ_0 allows one to significantly reduce the number of Newton iterations in cases where the convergence of the iterative process is ensured by the choice of the initial approximation (for example, within the parameter continuation method).

2.2.1. Choice of the initial value of the iteration parameter

Formula (12) requires the initial value τ_0 of the iteration parameter. In most cases, the value of $\tau_0 = 0.1$ provides a stable convergence of the CANM process even at the rough initial guess Ψ_0. Conversely, with this value of τ_0 the number of iterations remains quite large even with a very good initial guess.

In [20, 21], two adaptive algorithms for choosing the initial value of the iteration parameter are proposed, providing a larger or smaller value of τ_0 depending on the quality of the initial guess. These algorithms are defined by the following formulas:

$$\text{Variant 1}: \qquad \tau_0 = \frac{\delta_0}{2\delta_1(1)}, \tag{13}$$

$$\text{Variant 2}: \qquad \tau_0 = \frac{1}{2}\left|1 - \frac{\delta_1(1)}{\delta_0}\right|. \tag{14}$$

Here the residual δ_0 can be determined as in Eq. (8) or (11), and $\delta_1(1)$ is the residual in the case $k = 1$, $\tau = 1$. To exclude too small or too large values of τ_0, the constraint $\tau_{\min} \leqslant \tau_0 \leqslant 1$, $\tau_{\min} = 0.1$ is introduced.

In addition to the two variants (13) and (14), the third variant of the τ_0 calculation is proposed and tested in [41]. It is based on the combination of the algorithms: the initial value of the iteration parameter τ_0 is calculated using formulas (10), (11), then formulas (8), (12) are used to calculate the iteration parameter. The test calculations show that all three methods provide a decrease in the number of iterations compared to $\tau_0 = 0.1$, while the number of iterations is comparable to the number of iterations when using the method determined by formulas (10), (11). It should be highlighted that calculating τ_0 requires a one-time additional calculation of the residual for the case $\tau = 1$ at $k = 0$, which does not lead to a significant increase in the volume of calculations.

2.2.2. Convergence of the CANM process for iteration parameter values greater than 1

As shown in [22], the value of the CANM iteration parameter can exceed the "classical" value 1 without the loss of the convergence.

Let us assume that the following conditions are satisfied:

(c_1) $\|F'(\Psi) - F'(\tilde{\Psi})\| \leqslant L\,\|\Psi - \tilde{\Psi}\|, \quad \Psi, \tilde{\Psi} \in \mathcal{Y},$

(c_2) $\|(F'(\Psi_0))^{-1}\| \leqslant \beta,$

(c_3) $\|(F'(\Psi_0))^{-1}F(\Psi_0)\| \leqslant \eta, \quad a_0 = L\beta\eta,$

(c_4) $L\,\|(F'(\Psi_k))^{-1}\|\,\|(F'(\Psi_k))^{-1}F(\Psi_k)\| \leqslant a_k, \quad k = 0, 1, \ldots,$

and consider the open level set $L_\alpha = \{\Psi \in \mathcal{Y};\ \|F(\Psi)\| < \eta/\beta = \alpha\}$. In [22] the following Theorem is proved.

Theorem 1 *Let us assume that the conditions* (c_1)–(c_4) *are satisfied and the iteration parameter* τ_k *is chosen from the interval* I_k*, where*

$$I_k = \begin{cases} \left(0, \dfrac{-1+\sqrt{1+8a_k}}{2a_k}\right) \subseteq (0,2), & \text{for} \quad 0 < a_k < 1, \\ \left(0, \dfrac{1}{a_k}\right] \subseteq (0,1], & \text{for} \quad 1 \leqslant a_k < \infty. \end{cases} \tag{15}$$

Then the sequence $\{\Psi_k\}$ *obtained by iteration (5) is well defined, remains in* L_α*, and converges to some* Ψ^* *with* $F(\Psi^*) = 0$*.*

Theorem 1 gives us the opportunity to expand the τ-region of the CANM convergence from $\tau_k \in (0,1)$ to $\tau_k \in (0,2)$. It is clear from the condition (c_4) and from Eq. (15) that in the neighborhood of $a_k < 1$ one can choose the iteration parameter $\tau_k > 1$. Surely, the theorem does not provide the exact value of the right boundary point of the interval I_k for each k-th iteration. However, in some nonlinear problems, the empirical choice of the iteration parameter $\tau_k > 1$ provides a better convergence compared to $\tau_k = 1$. For example, within the continuation process of ϕ^4 standing waves in a ball of finite radius, the parameter τ_k is determined by formula (12) where τ_0=0.9, and the maximal value of τ_k is 1.5. Such an algorithm ensures a stable and quick convergence of the CANM process within the numerical continuation procedure in numerical studies presented in Section 3.2.

2.3. Generalization of CANM and applications

Various modifications of CANM are developed and widely used, enhancing its effectiveness for specific classes of problems and expanding its scope of application. One such modification, employed in a number of studies, is a generalization of CANM, according to which the parametrization of Eq. (2) with respect to the additional parameter t is carried out with an explicit dependence of F on t. In this case, the continuous parameter t is introduced into Eq. (2), so that at $t = 0$ a simple equation is obtained

$$F(0, \Psi(0)) \equiv F_0(\Psi_0) = 0, \tag{16}$$

which can be easily solved, and $\lim_{t\to\infty} F(t, \Psi(t)) = F(\Psi)$.

Thus, for the nonlinear functional (2), an evolution equation is constructed in the continuous parameter t, similar to Eq. (4):

$$\frac{d}{dt}F(t, \Psi(t)) = -F(t, \Psi(t)), \quad 0 \leqslant t < \infty \tag{17}$$

with the initial condition $\Psi(0) = \Psi_0$. From Eq. (17), denoting $A(t) = F'_\Psi(t, \Psi(t))$, we obtain:

$$\frac{d\Psi}{dt} = -[A(t)]^{-1}[F(t, \Psi(t)) + F'_t(t, \Psi(t))]. \tag{18}$$

Since the integral of Eq. (17) is $F(t, \Psi(t)) = e^{-t}F(0, \Psi_0)$, then as $t \to \infty$ $||F(t, \Psi(t))|| \to 0$, and one should expect the asymptotically stable convergence $\Psi(t)$ to the desired solution Ψ^*.

When approximating Eq. (18) using the Euler scheme, the continuous parameter $t : (t_0, t_1, \ldots$ $\ldots, t_k)$ is discretized; $t_0 = 0$, $t_{k+1} - t_k = \tau_k$ and the resulting iteration sequence is

$$\Psi_{k+1} = \Psi_k + \tau_k V_k, \tag{19}$$

where

$$V_k = -B_k[F(t_k, \Psi_k) + F'_t(t_k, \Psi_k)], \quad B_k = [A(t_k)]^{-1}. \tag{20}$$

By calculating the iterative correction V_k and the step τ_k for each value t_k, a new approximation Ψ_{k+1} to the solution Ψ^* is obtained. The iterative process (19), (20) must continue until the inequality

$$\delta_k = \|F(t_k, \Psi_k)\| < \epsilon. \tag{21}$$

One variant of parametrization based on the CANM generalization can be performed using a scalar function $g(t)$ [19], the so-called perturbation inclusion function, such that $g(0) = g(\infty) - 1 = g'(\infty) = 0$ and a representation of the function $F(t, \Psi(t))$ as a sum

$$F(t, \Psi(t)) = F_0(\Psi(t)) + g(t)[F(t, \Psi(t)) - F_0(\Psi(t))]. \tag{22}$$

For the equation $F_0 = 0$, the solution is easily found or, by assumption, known. This variant can be viewed as a combination of CANM and the parameter variation method [45]. In [60], the function $g(t)$ is calculated iteratively through an iterative correction. In [61, 62], the functional dependence $g(t)$ is specified explicitly. More details and references are given in [2]. The convergence conditions for the Newtonian evolution process (19), (22) for $g(t) = 1 - \exp(-t)$ are considered in [19].

One of the advantages of the presented approach is its constructive solution to the problem of choosing the initial approximation, which can be a known solution to the equation $F_0(\Psi) = 0$.

Another possible application of the approach under consideration is the construction of modified iterative schemes, where instead of inverting the operator F'_Ψ at each iteration, the derivative of a specially selected operator F_0 with a simple structure is inverted. The convergence issues of such schemes are also discussed in [19].

In [12], a parametrization of this type is used to develop efficient computational schemes with increased accuracy. Later, the same numerical scheme is used [63] to calculate multisoliton complexes in nonlinear ac-driven, damped Schrödinger equation with the sixth accuracy order.

In [61], a numerical scheme based on the CANM generalization is used for solving the eigenvalue problem for a nonlinear differential equation within the polaron model [64]. The integral part in the equation is considered as a perturbation and is introduced through an inclusion function. The presence of an integral operator in problems of this kind necessitates the inversion of filled high-order matrices approximating it at each iteration. The approach under consideration avoids this computationally intensive operation and significantly simplifies the solution to the problem. It is noteworthy that the polaron model is also investigated within other mathematical formulations of the problem: the multi-parameter BVP for a system of nonlinear differential equations and the eigenvalue problem for a system of nonlinear differential equations, see [2] for details and references. In [65], a three-dimensional system of differential equations is formulated within the polaron model and solved by means of the modified CANM numerical scheme.

The modified numerical scheme on the basis of the CANM generalization is used to numerically solve the eigenvalue problem for a system of integral equations within the QCD-inspired quarkonium model with various effective potentials [66]. The results are published in a series of papers listed and overviewed in [2].

2.4. CANM in spectral problems and applications

According to [67], classical spectral problems for linear operators can be treated as nonlinear functional equations. For this purpose, the eigenvalue problem of the form

$$\varphi(\lambda, y) \equiv \mathcal{D}y - \lambda y = 0$$

is supplemented by the normalization condition for the eigenelement

$$\Gamma(y) = 0,$$

where Γ is the normalization functional. In this formulation, the eigenvalue problem is a nonlinear functional equation

$$F(\Psi) = \begin{Bmatrix} \mathcal{D}y - \lambda y \\ \Gamma(y) \end{Bmatrix} = 0 \tag{23}$$

with respect to unknown $\Psi = \{\lambda, y\}$. In this case, iterative schemes represent various combinations of the Newtonian iterative process with inverse iterations. They are described in detail in [1, 2]. For example, when

$$\Gamma(y) = (y, y) - 1$$

the iteration procedure is as follows:

$$y_{k+1} = y_k + \tau_k v_k, \quad \lambda_{k+1} = \lambda_k + \tau_k \mu_k, \tag{24}$$

where the iteration corrections v_k and μ_k at each k are determined by formulas:

$$v_k = v_{1k} + \mu_k v_{2k}, \quad \mu_k = \frac{1 - (y_k, y_k) - 2(v_{1k}, y_k)}{2(v_{2k}, y_k)},$$

and the expressions for v_{1k}, v_{2k} have the form:

$$v_{1k} = -y_k, \quad v_{2k} = -[\varphi_y(\lambda_k, y_k)]^{-1} \varphi_\lambda(\lambda_k, y_k).$$

Such approaches are implemented in the SLIP1 [57], SLIPH4 [55], SLIPS2 [68], SNIDE [61], and SYSINT(SYSINTM) [69] programs in application to various classes of eigenvalue problems.

The generalization of this approach provides iterative schemes with the parametric asymptotic dependence of solutions [62] and numerical continuation schemes with the simultaneous calculation of the unknown parameter [70] (see [2, 5] for more details and references therein).

2.4.1. *Optimal choice of the CANM iteration parameter for a generalized algebraic eigenvalue problem*

Let us consider a generalized algebraic eigenvalue problem [22]

$$\begin{cases} (\mathbf{A} - \lambda \mathbf{B})\, \boldsymbol{y} = 0, \\ (\boldsymbol{y}, \mathbf{B}\boldsymbol{y}) - 1 = 0, \end{cases} \tag{25}$$

where $\mathbf{A}$ is the symmetric real- or complex-valued matrix, $\mathbf{B}$ is the symmetric positive definite real-valued matrix.

By applying CANM to Eq. (25), as described in the previous Section 2.4, the following iteration procedure in vector form is obtained

$$\boldsymbol{y}_{k+1} = \boldsymbol{y}_k + \tau_k \boldsymbol{v}_k, \quad \lambda_{k+1} = \lambda_k + \tau_k \mu_k. \tag{26}$$

The iteration corrections $\boldsymbol{v}_k$ and μ_k are determined by formulas:

$$\boldsymbol{v}_k = -\boldsymbol{y}_k + \mu_k \boldsymbol{\theta}_k, \quad \mu_k = \frac{1 + (\boldsymbol{y}_k, \mathbf{B}\boldsymbol{y}_k)}{2\,(\boldsymbol{\theta}_k, \mathbf{B}\boldsymbol{y}_k)}, \tag{27}$$

where $\boldsymbol{\theta}_k$ is the solution of a system of linear algebraic equations

$$(\mathbf{A} - \lambda_k \mathbf{B})\,\boldsymbol{\theta}_k = \mathbf{B}\boldsymbol{y}_k. \tag{28}$$

Now let us consider the residual of Eq. (25) in the k-th iteration

$$\boldsymbol{r}_k = (\mathbf{A} - \lambda_k \mathbf{B})\boldsymbol{y}_k. \tag{29}$$

Using (29), (26), and (27), it is easy to show that

$$\boldsymbol{r}_{k+1} = (1 - \tau_k)\boldsymbol{r}_k - \tau_k^2 \mu_k \mathbf{B}\boldsymbol{v}_k. \tag{30}$$

Therefore, we have

$$\|\boldsymbol{r}_{k+1}\|^2 = (1 - \tau_k)^2 \|\boldsymbol{r}_k\|^2 - 2(1 - \tau_k)\tau_k^2 \mathrm{Re}(\boldsymbol{r}_k^*, \mu_k \mathbf{B}\boldsymbol{v}_k) + \tau_k^4 \|\mu_k \mathbf{B}\boldsymbol{v}_k\|^2. \tag{31}$$

Here b^* and $\mathrm{Re}(b)$ denote the complex conjugate and real part of b, respectively.

We denote $f(\tau_k) = \|\boldsymbol{r}_{k+1}\|^2$ and calculate its derivative with respect to τ_k

$$f'(\tau_k) = 2(\tau_k - 1)\|\boldsymbol{r}_k\|^2 - 2(2\tau_k - 3\tau_k^2)\mathrm{Re}(\boldsymbol{r}_k^*, \mu_k \mathbf{B}\boldsymbol{v}_k) + 4\tau_k^3 \|\mu_k \mathbf{B}\boldsymbol{v}_k\|^2. \tag{32}$$

It is evident that $f'(0) = -2\|r_k\|^2 < 0$ and $f'(2) = 2f(2) > 0$. Hence, it follows that the function $f(\tau_k)$ has at least one minimum in the interval $(0, 2)$. If it has three roots in the interval $(0, 2)$, then $f(\tau_k)$ has minimums at the smallest and largest roots, and one should choose the root that yields the smallest value of $f(\tau_k)$. Thus, it is possible to find the optimal value of the iteration parameter $\tau_k^{\mathrm{opt}} = \tau_k$ by calculating the roots of the cubic equation $f'(\tau_k) = 0$.

Applying this algorithm to numerous calculations of the generalized eigenvalue problem confirms that the optimal iteration parameter τ_k^{opt} is indeed chosen from the interval $(0, 2)$, as shown in Section 2.2.2. The iteration procedure (26) with the optimal iteration parameter τ_k^{opt} provides the best convergence with respect to the iteration number k compared to other algorithms for calculating τ_k in the interval $(0, 1)$.

The approach described above is implemented in the KANTBP 4M [71] and KANTBP 5M [72] programs on the Maple system for various classes of problems of calculating metastable states.

2.4.2. Nonlinear eigenvalue problem

Consider a nonlinear eigenvalue problem [22]

$$\begin{cases} \mathbf{A}(\lambda)\boldsymbol{y} = 0, \\ (\boldsymbol{y}, \mathbf{B}\boldsymbol{y}) - 1 = 0, \end{cases} \tag{33}$$

where $\mathbf{A}(\lambda)$ is a real- or complex-valued matrix nonlinearly dependent on the spectral parameter λ, and $\mathbf{B}$ is a symmetric positive definite real-valued matrix that does not depend on the spectral parameter λ. The application of CANM to solve Eq. (33) reduces to the equation

$$\mathbf{A}(\lambda_k)\boldsymbol{\theta}_k = -\mathbf{A}'(\lambda_k)\boldsymbol{y}_k. \tag{34}$$

Here, $\mathbf{A}'(\lambda)$ is the derivative of the matrix $\mathbf{A}(\lambda)$ with respect to the spectral parameter λ. Suppose that the correction μ_k is calculated by formula (27), and the following approximations for $\boldsymbol{y}_{k+1}$, λ_{k+1} are found by formula (26), and the discrepancy is determined by the expressions

$$\overline{\boldsymbol{r}}_k = \mathbf{A}(\lambda_k)\boldsymbol{y}_k. \tag{35}$$

Then, it is easy to show that

$$\overline{\boldsymbol{r}}_{k+1} = (1-\tau_k)\overline{\boldsymbol{r}}_k + \tau_k^2\mu_k\mathbf{A}'(\lambda_k)\boldsymbol{v}_k + O\left(\tau_k^2\mu_k^2\right). \tag{36}$$

A comparison of (36) with (30) shows that the discrepancies $\overline{\boldsymbol{r}}_{k+1}$ and $\boldsymbol{r}_{k+1}$ have the same main part with $\mathbf{B} = -\mathbf{A}'(\lambda_k)$. Therefore, it is possible to find the optimal value of the iteration parameter $\tau_k^{\rm opt} = \tau_k$ in the interval $(0, 2)$ as shown in the previous section 2.4.1.

2.5. Summary to Section 2

This Section presents the fundamentals of an approach to constructing iterative schemes based on CANM, and provides a summary of various modified CANM-based schemes and their applications to the investigation of complex physical systems at JINR and its Member States. Results on the theoretical development and improvement of the convergence of iterative procedures based on CANM, obtained over the past two decades, are also demonstrated.

In general, CANM can be classified as a first-choice recipe for the numerical solution of nonlinear BVPs and spectral problems of various types due to the quadratic convergence of the iterative process in the vicinity of a local solution and the flexible ability to take into account the specific characteristics of specific problems due to the presence of an iterative parameter and the introduction of an auxiliary function within the CANM generalization.

A bottleneck of CANM, which can require the consideration of alternative numerical approaches, is the need to calculate the inverse Fréchet derivative operator at each iteration. In some cases, this takes significant computer time and, if the operator is ill-conditioned, degrades the convergence of the iterations. It should be noted that in a number of cases, the aforementioned problems can be resolved through various modifications of CANM, such as derivative-free iterative schemes, including those described in two detailed previous reviews [2, 5].

The following sections present the methods and results of numerical studies conducted over the past two decades at JINR and its Member States on several physically significant problems, in which CANM-based computational schemes were widely used.

3. CANM in the numerical study of time-oscillating localised structures

In this Section, a numerical study of time-oscillating, spatially localised structures in two well-known nonlinear equations of mathematical physics is discussed. Both equations describe a wide range of complex physical phenomena. In both cases, the numerical study is reduced to solving a nonlinear two-dimensional BVP over a wide range of parameters. For this purpose, a CANM-based solver of BVPs is used within the previously developed [5, 73] and many times practically proven CANM-based computational scheme adapted to the problems under consideration in Section 3. The computational procedure is based on path-following the solutions of the aforementioned BVPs with respect to a parameter, identifying the turning points on the bifurcation curves and reaching new branches of coexisting solutions (examples of such branches can be seen below in Figures 1, 2, 3, and 8). The CANM approach used for each parameter value in the numerical solution of the nonlinear two-dimensional BVP ensures high accuracy and the rapid convergence of the iteration process. The numerical technique is described in more detail in Section 3.1 for the numerical study of time-periodic solitons in a parametrically driven, damped nonlinear Schrödinger equation. In Section 3.2, the computational procedure is organized similarly, therefore, its description is briefer, with a focus on its distinctive features.

3.1. Time-periodic solutions in a parametrically driven, damped nonlinear Schrödinger equation

A parametrically driven, damped nonlinear Schrödinger equation is investigated

$$\imath\frac{\partial\psi(x,t)}{\partial t}+\frac{\partial^2\psi(x,t)}{\partial x^2}+2|\psi(x,t)|^2\psi(x,t)-\psi(x,t)=h\psi^*(x,t)-\imath\gamma\psi(x,t), \tag{37}$$

where $\gamma>0$ is the damping coefficient, $h>0$ is the amplitude of the parametric driver. Eq. (37) describes a large number of resonant phenomena in various physical media listed in [74, 75] and in references therein.

Eq. (37) exhibits different classes of soliton solutions existing on the (h,γ)-plane over the straight line $h=\gamma$. Two stationary solitons $\psi_+(x)$ and $\psi_-(x)$ are available in analytic form [76]:

$$\psi_\pm(x)=A_\pm e^{-\imath\theta_\pm}\mathrm{sech}(A_\pm x), \tag{38}$$

where

$$A_\pm=\sqrt{1\pm\sqrt{h^2-\gamma^2}},\quad \theta_+=\frac{1}{2}\arcsin\frac{\gamma}{h},\quad \theta_-=\frac{\pi}{2}-\theta_+.$$

The soliton $\psi_-(x)$ is known to be unstable for all h and γ. Stability properties of the soliton $\psi_+(x)$ for various h and γ are examined in [76].

Other localised attractors of Eq. (37) are obtained by means of the CANM-based numerical study (stationary multi-soliton complexes [77], uniformly travelling solitons and complexes [74, 75]), and in direct numerical simulations (time-periodic and quasi-periodic solitons [78, 79]).

Time-periodic attractors of Eq. (37), which arise as a Hopf bifurcation of a stable stationary soliton solution, were re-obtained in [80–84] as solutions of a two-dimensional BVP for Eq. (37). This approach allowed understanding complexity and interconnection of coexisting types of soliton solutions in Eq. (37). Full results of analytical and numerical studies of bifurcations and the complexity of coexisting stationary, time-periodic and quasi-periodic states of Eq. (37) for both strong and weak damping are presented in [24, 25]. In this Section, the CANM-based numerical approach for the analysis of time-periodic solitons is described, and representative numerical results on transformations of periodic one- and multi-soliton branches are demonstrated.

3.1.1. Mathematical statement of a two-dimensional boundary value problem

Time-periodic solutions of Eq. (37) are considered as solutions of a BVP on the two-dimensional domain $(-\infty,\infty)\times(0,T)$. The boundary conditions have the form

$$\psi(x,t)=0\quad\text{as}\quad x\to\pm\infty,\quad\text{and}\quad\psi(x,t+T)=\psi(x,t). \tag{39}$$

The two-dimensional BVP (37), (39) is solved numerically with respect to the unknown period T and the function $\psi(x,t)$.

Letting $\tilde{t}=t/T$ $(0<\tilde{t}<1)$ and defining $\tilde{\psi}(x,\tilde{t})=\psi(x,t)$, the BVP (37), (39) can be reformulated on the rectangle $(-L,L)\times(0,1)$ (where L is chosen to be sufficiently large):

$$\begin{cases}\mathbf{F}\equiv\imath\dfrac{\partial\tilde{\psi}(x,\tilde{t})}{\partial\tilde{t}}+T\Phi(\tilde{\psi}(x,\tilde{t}),h,\gamma)=0,\\ \tilde{\psi}(\pm L,\tilde{t})=0,\\ \tilde{\psi}(x,0)=\tilde{\psi}(x,1).\end{cases} \tag{40}$$

Here,

$$\Phi(\tilde{\psi}(x,\tilde{t}),h,\gamma)=\frac{\partial^2\tilde{\psi}(x,\tilde{t})}{\partial x^2}+2|\tilde{\psi}(x,\tilde{t})|^2\tilde{\psi}(x,\tilde{t})-\tilde{\psi}(x,\tilde{t})-h\tilde{\psi}^*(x,\tilde{t})+\imath\gamma\tilde{\psi}(x,\tilde{t}). \tag{41}$$

Eq. (40) is supplemented with an additional equation borrowed in [85]:

$$\mathrm{Re}\left(\Phi(\tilde{\psi}(x^*,\tilde{t}^*),h,\gamma)\right)=0,\quad x^*=t^*=0. \tag{42}$$

The solutions $(T,\tilde{\psi}(x,\tilde{t}))$ of the two-dimensional BVP (40), (42) are path-followed in h for fixed γ, with the Hopf bifurcation points of the static solution used as starting points in the continuation process. At each value of the parameter h, the CANM iteration scheme presented in 3.1.2 is employed. The continuation algorithm is described in 3.1.3. Below, the tildes above ψ and t are omitted.

For the graphical representation of solutions, the averaged energy, defined by

$$\bar{E}=\frac{1}{T}\int_0^T dt\int_{-\infty}^{\infty}dx\,E(x,t), \tag{43}$$

is used, where

$$E(x,t)=\left|\frac{\partial\psi(x,t)}{\partial x}\right|^2+|\psi(x,t)|^2-|\psi(x,t)|^4+h\mathrm{Re}(\psi^2(x,t)). \tag{44}$$

The stability of solutions is classified by examining the Floquet multipliers of the corresponding linearised equation. Details are in [24, 80].

3.1.2. Newtonian iteration scheme

The iteration process is based on CANM [5]. Within this approach, the additional continuous parameter $\mathcal{T}$ is introduced, and a set of equations is formulated for system (40)–(42) with respect to the auxiliary unknown function $\mathcal{V}=\psi_{\mathcal{T}}$ and the parameter $\mu=T_{\mathcal{T}}$:

$$\begin{cases}\imath\dfrac{\partial\mathcal{V}(x,t)}{\partial t}+\mu\Phi(\psi(x,t),h,\gamma)\\ \quad+T\left(\dfrac{\partial^2\mathcal{V}(x,t)}{\partial x^2}+(2|\psi(x,t)|^2+4|\psi(x,t)|\psi(x,t)\right.\\ \qquad\left.-1+\imath\gamma)\mathcal{V}(x,t)-h\mathcal{V}^*(x,t)\right)=-\mathbf{F}(\psi(x,t),T),\\ \mathcal{V}(\pm L,t)=-\psi(\pm L,t),\\ \mathcal{V}(x,0)-\mathcal{V}(x,1)=-[\psi(x,0)-\psi(x,1)];\end{cases} \tag{45}$$

$$\begin{aligned}&\mathrm{Re}\left(\frac{\partial^2\mathcal{V}(x,t)}{\partial x^2}+[2|\psi(x,t)|^2+4|\psi(x,t)|\psi(x,t)-1+\imath\gamma]\mathcal{V}(x,t)-h\mathcal{V}(x,t)\right)\\ &\qquad=-\mathrm{Re}[\Phi(\psi(x,t),h,\gamma)],\quad x=x^*=t=t^*=0.\end{aligned} \tag{46}$$

Here, $T=T(\mathcal{T})$, $\mu=\mu(\mathcal{T})=T_{\mathcal{T}}$, $\psi(\mathcal{T})=\psi(x,t)$ and $\mathcal{V}=\mathcal{V}(x,t)=\psi_{\mathcal{T}}$. As $\mathcal{T}\to\infty$, the solution of (45), (46) tends to the solution of system (40)–(42). Writing $T_k\equiv T(\tau_k)$, $\mu_k\equiv\mu(\tau_k)$, $\psi_k\equiv\psi(t_k)$, $\mathcal{V}_k\equiv\mathcal{V}(\tau_k)$, and approximating the $\mathcal{T}$-derivatives $\mathcal{V}$ and μ in Eqs. (45), (46) by

one-step Euler's formula give the following iteration algorithm. The $(k+1)$-th guess to the function ψ and the period T is calculated as:

$$\psi_{k+1} = \psi_k + \xi_k \mathcal{V}_k; \quad T_{k+1} = T_k + \xi_k \mu_k; \tag{47}$$

where k is the number of Newtonian iterations, $0 < \xi \leqslant 1$ is the numerical parameter calculated by means of the adaptive formula (12),

$$\mathcal{V}_k = v_k^{(1)} + \mu_k v_k^{(2)}; \tag{48}$$

the functions $v_k^{(1)}$ and $v_k^{(2)}$ are the numerical solutions of two linear two-dimensional BVPs

$$\begin{cases} \imath \dfrac{\partial}{\partial t} v_k^{(1)} + T_k \dfrac{\partial^2}{\partial x^2} v_k^{(1)} + \hat{A}_k v_k^{(1)} + \hat{B}_k v_k^{(1)*} = -\mathbf{F}_k, \\ v_k^{(1)}(\pm L, t) = \psi_k(\pm L, t), \\ v_k^{(1)}(x,0) - v_k^{(1)}(x,1) = -[\psi_k(x,0) - \psi_k(x,1)]; \end{cases} \tag{49}$$

$$\begin{cases} \imath \dfrac{\partial}{\partial t} v_k^{(2)} + T_k \dfrac{\partial^2}{\partial x^2} v_k^{(2)} + \hat{A}_k v_k^{(2)} + \hat{B}_k v_k^{(2)*} = -\Phi_k, \\ v_k^{(2)}(\pm L, t) = 0, \\ v_k^{(2)}(x,0) - v_k^{(2)}(x,1) = 0. \end{cases} \tag{50}$$

Here, $\mathbf{F}_k$ and Φ_k are defined by Eqs. (40) and (41), respectively, A_k and B_k have a form:

$$A_k = 4T_k \psi_k \psi_k^* - T_k - \imath\gamma T_k; \quad B_k = 2T_k (\psi_k)^2 - hT_k. \tag{51}$$

The formulas for calculating the μ_k quantity at each iteration follow from Eq. (46):

$$\mu_k = \frac{-G - R}{F}, \tag{52}$$

where

$$F = \frac{\partial^2 v_R^{(2)}}{\partial x^2} + 6\psi_R^2 v_R^{(2)} + 4\psi_I \psi_R v_I^{(2)} + 2\psi_I^2 v_R^{(2)} - v_R^{(2)} - h v_R^{(2)} - \gamma v_I^{(2)},$$

$$G = \frac{\partial^2 v_R^{(1)}}{\partial x^2} + 6\psi_R^2 v_R^{(1)} + 4\psi_I \psi_R v_I^{(1)} + 2\psi_I^2 v_R^{(1)} - v_R^{(1)} - h v_R^{(1)} - \gamma v_I^{(1)},$$

$$R = \frac{\partial^2 \psi_R}{\partial x^2} + 2\psi_R^3 + 2\psi_I^2 \psi_R - \psi_R - h\psi_R - \gamma\psi_I,$$

$$\psi_R = \operatorname{Re} \psi_k(x^*, 0); \quad \psi_I = \operatorname{Im} \psi_k(x^*, 0);$$

$$v_R^{(1,2)} = \operatorname{Re} v_k^{(1,2)}(x^*, 0); \quad v_I^{(1,2)} = \operatorname{Im} v_k^{(1,2)}(x^*, 0).$$

Iteration procedures (47) and (52) are iterated until the inequality

$$\|\mathbf{F}\| \leqslant \delta$$

holds true, where $\|\cdot\|$ is the standard C-norm, and $\delta > 0$ is a small number chosen beforehand. Typically, $\delta = 10^{-8}$ is taken. Within the numerical continuation procedure described below,

the initial value of the residual $\|\mathbf{F}\|$ is about 0.1, and 4–5 iterations are required at each value of h.

For the finite-difference approximation of t- and x-derivatives, standard five-point formulae of the fourth-order accuracy are used. Following the ideas of [12], the five-point uniform discretization is organized to produce a system of linear algebraic equations with a block-tridiagonal matrix for the linear BVPs (49) and (50). This algebraic system is numerically solved by means of an algorithm that can be considered as the matrix generalization of the standard Thomas method (see, i.e. [86]).

Most calculations are performed on the domain $(-L, L) = (-50, 50)$, with the stepsizes of discrete meshes in x and t, being $\Delta x = 0.05$ and $\Delta t = 0.01$.

3.1.3. Numerical continuation algorithm

To trace the transformations and bifurcations of solutions of BVP (40)–(42)as the parameter h changes, the numerical study is organized as a sequential solution of the BVP for parameter values with a certain increment. For each solution, the energy value that characterizes the solution and helps organize the path-following process along the branch $\bar{E}(h)$ is calculated. The continuation algorithm must account for the possibility that, for a certain parameter value, forward continuation is impossible, since the function $\bar{E}(h)$ at this point merges with another branch corresponding to another solution coexisting with the one already found. Therefore, it is necessary to establish a criterion for identifying this point, which is checked during continuation with respect to the parameter. Compared to alternative approaches (see, for example, [85, 87]), the algorithm described here does not complicate the problem being solved at each parameter step, since the continuation method and the solver are independent of each other. This computational scheme was proposed for the numerical study of stationary multisoliton complexes and was subsequently used in the numerical analysis of various problems, including the works [23, 77, 88, 89] and others. A general description of the method is given in [5, 70, 73]. Here, the continuation procedure is described for the problem considered in this section.

At each $(i+1)$-th step of numerical continuation procedure, the initial guess of the function ψ and the period T for the Newtonian process is constructed using the results obtained for two previous, i-th and $(i-1)$-th, values of the parameter h:

$$\psi(h_{i+1}) = \psi(h_i) + (h_{i+1} - h_i) \cdot \frac{\psi(h_i) - \psi(h_{i-1})}{h_i - h_{i-1}}, \tag{53}$$

$$T(h_{i+1}) = T(h_i) + (h_{i+1} - h_i) \cdot \frac{T(h_i) - T(h_{i-1})}{h_i - h_{i-1}}. \tag{54}$$

The $(i+1)$-th increment $\Delta h_{i+1} = h_{i+1} - h_i$ is calculated as follows

$$\Delta h_{i+1} = \Delta h_i \cdot \frac{\bar{E}(h_{i-1}) - \bar{E}(h_{i-2})}{\bar{E}(h_i) - \bar{E}(h_{i-1})}. \tag{55}$$

The turning points of the bifurcation curve $\bar{E}(h)$ (where the direction of continuation changes when moving to a new branch) are identified with the help of the following relation, which is tested at each step of numerical continuation:

$$\left| \frac{h_i - h_{i-1}}{\bar{E}(h_i) - \bar{E}(h_{i-1})} \right| < \varepsilon. \tag{56}$$

where $\varepsilon > 0$ is a small known quantity. It should be pointed out that (56) is a simple approximation of the equality $dh/dE = 0$, which is valid at the turning points of the curve $h(\bar{E})$.

In case of running into a turning point, the sign of the h-increment should be changed.

The choice of the initial guess in the form (53), (54) and the use of the adaptive formula (55) for the increment Δh prevent the continuation from reversing to the previous branch $\bar{E}(h)$ and provide a quick convergence of the CANM iteration process at each step of numerical continuation. Naturally, the start value of the parameter increment should be tuned manually to provide the stable convergence of the CANM iteration.

3.1.4. Few-mode approximation

In addition to the analysis of time-periodic solitons as solutions of a two-dimensional BVP, the possibility of using a truncated Fourier expansion to reduce the computationally expensive two-dimensional BVP to a problem on a one-dimensional interval is explored.

Let us start by decomposing $\psi(\bar{x},\bar{t})$ as

$$\psi(\bar{x},\bar{t}) = A_+[U(\bar{x},\bar{t}) + \imath V(\bar{x},\bar{t})]e^{-\imath\theta_+},$$

where A_+ and θ_+ are as in Eq. (38), and $\bar{t} = A_+^2 t$, $\bar{x} = A_+ x$. This casts Eq. (37) in the following form:

$$\begin{cases} -\dfrac{\partial V(x,t)}{\partial t} - 2\Gamma V(x,t) = -\dfrac{\partial^2 U(x,t)}{\partial x^2} + U(x,t) - 2[U^2(x,t)+V^2(x,t)]U(x,t), \\ +\dfrac{\partial U(x,t)}{\partial t} + 2HV(x,t) = -\dfrac{\partial^2 V(x,t)}{\partial x^2} + V(x,t) - 2[U^2(x,t)+V^2(x,t)]V(x,t), \end{cases} \tag{57}$$

where the bars above x and t are omitted. Here $\Gamma = \gamma/A_+^2$ and $H = \sqrt{h^2-\gamma^2}/A_+^2$ are introduced. Near the Hopf bifurcation point, the periodic functions $U(x,t)$ and $V(x,t)$ can be expanded in the Fourier series. The crudest approximation is obtained by retaining only the first and zeroth harmonics. The resulting three-mode reduced system has the following form:

$$\begin{cases} \dfrac{\partial^2 u}{\partial x^2} - u + 2(u^2+v^2)u + 4(3|\mathcal{A}|^2+|\mathcal{B}|^2)u + 4(\mathcal{A}\mathcal{B}^* + \mathcal{A}^*\mathcal{B})v - 2\Gamma v = 0, \\ \dfrac{\partial^2 v}{\partial x^2} - v + 2(u^2+v^2)v + 4(|\mathcal{A}|^2+3|\mathcal{B}|^2)v + 4(\mathcal{A}\mathcal{B}^* + \mathcal{A}^*\mathcal{B})u + 2Hv = 0, \\ \dfrac{\partial^2 \mathcal{A}}{\partial x^2} - \mathcal{A} + 2(3u^2+v^2)\mathcal{A} \\ \qquad + 2(3|\mathcal{A}|^2+2|\mathcal{B}|^2)\mathcal{A} + 2(2uv+\mathcal{A}^*\mathcal{B})\mathcal{B} - 2\Gamma\mathcal{B} - \imath\Omega\mathcal{B} = 0, \\ \dfrac{\partial^2 \mathcal{B}}{\partial x^2} - \mathcal{B} + 2(u^2+3v^2)\mathcal{B} \\ \qquad + 2(2|A|^2+3|\mathcal{B}|^2)\mathcal{B} + 2(2uv+\mathcal{B}^*\mathcal{A})A + 2H\mathcal{B} + \imath\Omega\mathcal{A} = 0. \end{cases} \tag{58}$$

Here, $\Omega = 2\pi/(A_+^2 T)$ and the solution $u = \mathrm{sech}(x)$, $v = \mathcal{A} = \mathcal{B} = 0$ corresponds to the stationary soliton $\psi_+(x)$ of Eq. (37). A nontrivial homoclinic solution corresponding to the periodically oscillating soliton of Eq. (37) bifurcates from it as H is increased for fixed Γ. The bifurcation point corresponds to the point of the Hopf bifurcation of the stationary soliton within Eq. (37).

The numerical solution of system (58) is based on the CANM iteration and Numerov's finite-difference approximations of the fourth accuracy order. The numerical continuation procedure is organized as in [73].

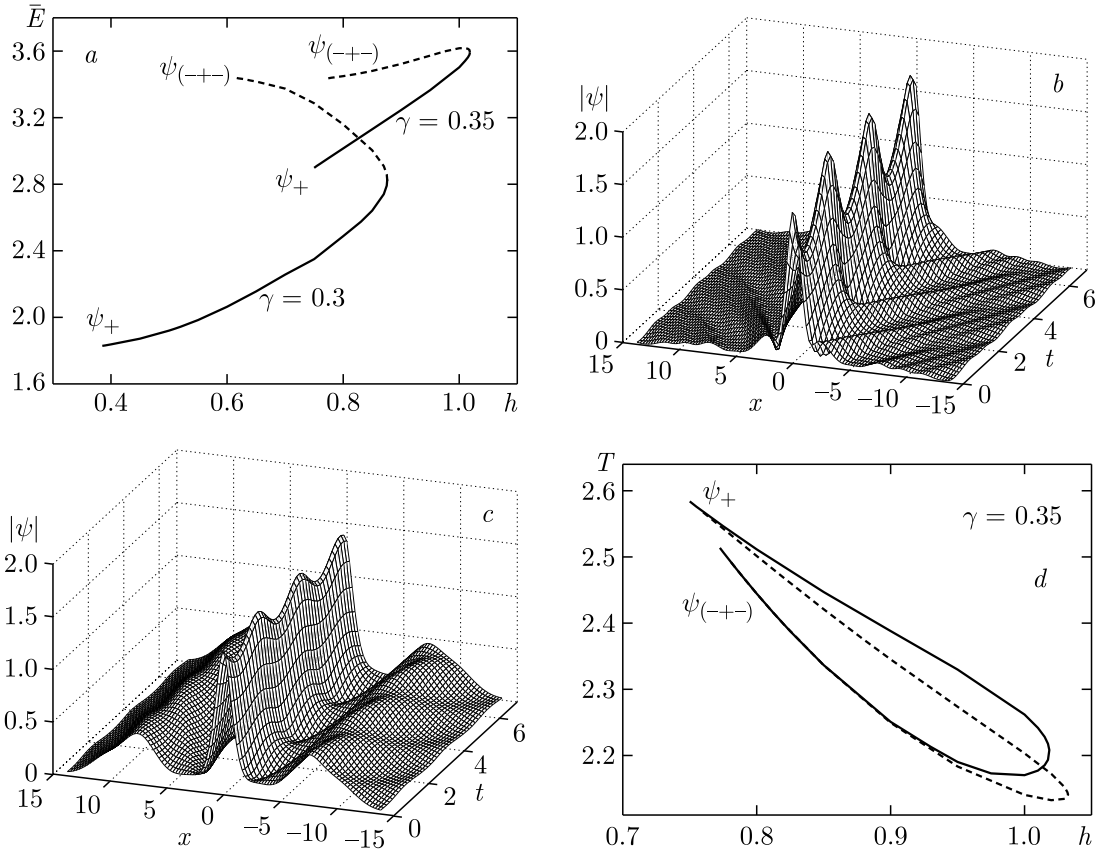

Figure 1. *a*) Energy of periodic solutions with $\gamma = 0.30$ and $\gamma = 0.35$ in dependence on parameter h. The solid curves show the stable branch, and the dashed ones show the unstable branch. The absolute value of the periodic solution with $\gamma = 0.35$: *b*) $h = 0.95$, $T = 2.329$, stable time-periodic one-soliton solution. *c*) $h = 0.85$, $T = 2.337$, unstable time-periodic three-soliton solution. In each case, several oscillation periods are demonstrated. *d*) $T(h)$ branch for the full system (solid curve) and few-mode approximation (dashed curve) in the case of $\gamma = 0.35$.

3.1.5. Results of the numerical study

In [24, 25, 80–82], the above numerical approach is applied to periodic single-soliton solutions and multi-soliton complexes with $\gamma = 0.41$, 0.38, 0.35, 0.3, 0.265, and to periodic two-soliton solutions with the strong damping $\gamma = 0.565$ as representative sections of various parts of the attractor chart in [79]. Here, the representative results are given for the case of $\gamma \simeq 0.35$ for which the one- and two-soliton solutions coexist. Indeed, the $\psi_+(x)$ solutions undergo the Hopf bifurcation for $\gamma < 0.356$ [76]. Conversely, stable stationary two-soliton complexes $\psi_{(++)}(x)$ (and the corresponding Hopf bifurcation points) exist only for $\gamma > 0.345$ [77].

Each Hopf bifurcation gives rise to a temporally periodic soliton solution. Thus, in the case of $\gamma = 0.35$, the time-periodic one-soliton solution coexists with periodic two-soliton complexes; however, our calculations show that the corresponding branches are not connected.

In Figure 1, *a*, the numerical continuation starts from the Hopf bifurcation point $h_H = 0.75$ in the case of $\gamma = 0.35$. The transformation of the solution is similar to the one in the case of $\gamma = 0.30$ (the corresponding Hopf bifurcation point is $h_{H0} = 0.385$). The left h_{H0} endpoint of each of the two curves in Figure 1, *a* corresponds to the stationary single-soliton solution $\psi_+(x)$. At this value of h, a stable time-periodic soliton is born. Near the leftmost point of the $\bar{E}(h)$ curve in Figure 1, *a*, the periodic solution looks like a single soliton with a periodically oscillating amplitude and width, see Figure 1, *b*.

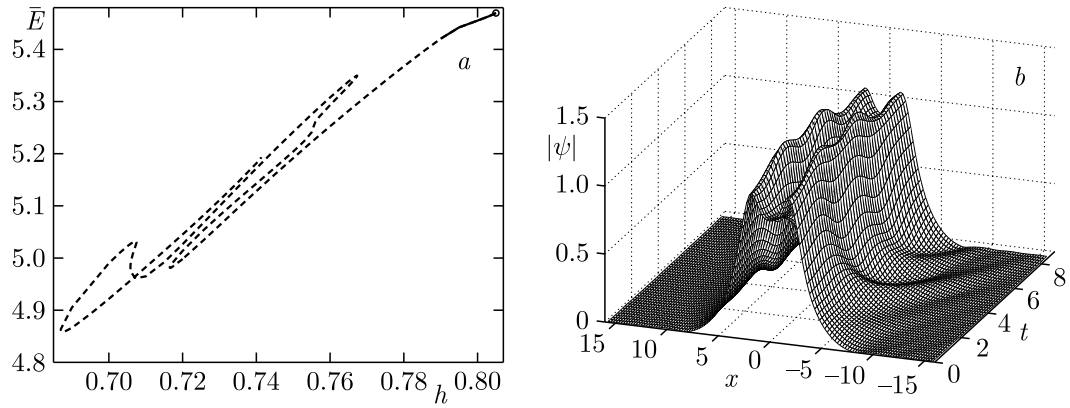

Figure 2. *a*) The "lower" $\bar{E}(h)$ branch of the two-soliton periodic solution for $\gamma = 0.35$. The solid curve marks the stable branch, and the dashed one marks the unstable branch.The circle indicates the starting point $h_{H1} = 0.806$ of thecontinuation. *b*) Stable two-soliton periodic solution with $\gamma = 0.35$, $h = 0.795$, $T = 8.788$, shown over one period.

The periodic solution loses its stability at the turning point $h_{\rm sn}$; $h_{\rm sn} = 0.8761$ for $\gamma = 0.30$ and $h_{\rm sn} = 1.0186$ for $\gamma = 0.35$. As we continue moving back along the unstable branch of the curve $\bar{E}(h)$, the oscillating solution evolves into a three-hump structure, which can be interpreted as a triplet of solitons, see Figure 1, *c*. The end point of the unstable branch ($h = 0.61$ for $\gamma = 0.30$ and $h = 0.760$ for $\gamma = 0.35$) corresponds to the stationary unstable three-soliton complex $\psi_{(-+-)}(x)$.

Figure 1, *d* compares results obtained using the few-mode reduced system (58) to the solution of the full partial differential equation (PDE) (37) for $\gamma = 0.35$. The solid curve is obtained by solving Eqs. (37), (39) on the (x, t)-domain. The dashed curve results from the solution of the system (58). It is seen that the few-mode approximation can qualitatively reproduce the transformation of periodic solitons with varying h. However, the first and zeroth harmonics alone are not enough to reproduce the shape of the corresponding bifurcation curve. To make the approximation better, it is needed to increase the number of modes. The case of the five-mode approximation is considered in [83, 84].

As mentioned above, there are two Hopf bifurcation points at the branch of the stationary two-soliton complex in the case of $\gamma = 0.35$: the "lower" Hopf bifurcation occurs at $h_{H1} = 0.806$, and the "upper" Hopf bifurcation occurs at $h_{H2} = 0.832$ [24]. The "lower" Hopf bifurcation is supercritical; for $h < h_{H1}$, the unstable stationary two-soliton solution is replaced by a stable periodic two-soliton complex. The results of numerical continuation from the start point are presented in Figure 2, *a* with $h_{H1} = 0.806$.

As the periodic complex continues in the direction of smaller h, the periodic solution is stable while $0.79 < h < 0.806$; the representative stable solution is shown in Figure 2, *b* for $h = 0.795$. At $h = 0.79$, it loses its stability to a double-periodic complex of two solitons. As the unstable branch $\bar{E}(h)$ continues, it makes a number of turns (Figure 2, *a*), the spatiotemporal complexity of the solution increases, but it never regains its stability.

The "upper" Hopf bifurcation $h_{H2} = 0.832$ is subcritical: the emerging periodic branch is unstable and coexists with the stable stationary branch (i.e., the periodic branch continues in the direction of lower h, see Figure 3, *a*). The entire branch is unstable in the case of $\gamma = 0.35$.

However, the increase of γ results in the stabilization of the periodic two-soliton solution. This is exemplified by $\gamma = 0.38$; the corresponding "upper" Hopf bifurcation point is $h_{H2} = 0.89$. The second branch in Figure 3, *a* features the stable interval $h_1 < h < h_2$, with $h_1 = 0.9415$

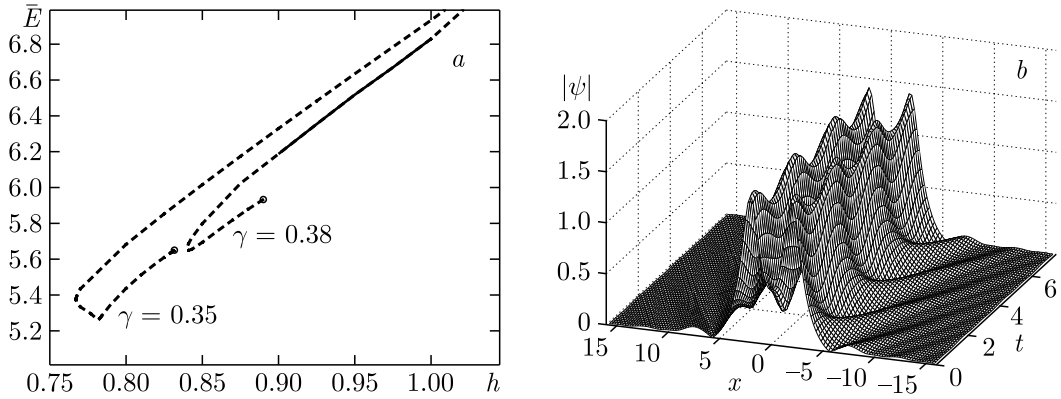

Figure 3. *a*) The "upper" $\bar{E}(h)$ branches of the two-soliton periodic solution for $\gamma = 0.35$ and $\gamma = 0.38$. The solid curve marks the stable branch, and the dashed one marks the unstable branch. The circles indicate the starting point of the continuation (the point where the stationary two-soliton complex undergoes the Hopf bifurcation). *b)* Two-soliton periodic solution on the stable branch. Here $\gamma = 0.38$, $h = 0.95$, $T = 2.476$. Several oscillation periods are shown.

and $h_2 = 1.015$ in case $\gamma = 0.38$. Figure 3, *b* demonstrates the stable periodic solution for $h = 0.95$. At the bifurcation points $h_{1,2}$, the periodic two-soliton solution loses stability to a quasi-periodic two-soliton complex. Quasiperiodic solutions cannot be obtained within the numerical approach presented above. They are obtained in the direct numerical simulation of Eq. (37). A pseudospectral method [78, 90, 91] based on the Fourier discretization in space and the numerical solution of the resulting initial-value ordinary differential equation problem with the help of the Runge-Kutta algorithm is employed.

3.1.6. Summary to Section 3.1

The time-periodic solitons of the parametrically driven, damped nonlinear Schrödinger equation are obtained numerically as solutions of the two-dimensional BVP of Eq. (37). The CANM-based numerical approach allows one to find new temporally periodic two-soliton solutions and investigate the transformations of time-periodic solitons and interconnection between coexisting branches of stable and unstable oscillating solitons and complexes.

The stationary two-soliton solution shown in Figure 4, *a* for $\gamma = 0.38$, $h = 0.85$ is stable in the yellow color region of the diagram in Figure 4, *b* reproduced from [25]. This diagram summarizes the numerical results on stationary and periodic two-soliton attractors. The stability domain of time-periodic complexes consists of stability regions of complexes emerging in the Hopf bifurcation points (blue color domains). A schematic position of the quasiperiodic stability domain is also given as a result of direct numerical simulations, see the magenta color region in Figure 4, *b*.

Stationary and time-periodic solitons are shown to coexist with stationary, time-periodic and quasiperiodic two-soliton solutions. For example, for $\gamma = 0.35$, the periodic free-standing soliton and the periodic two-soliton complex coexist between $h = 0.806$ and $h = 0.832$. However, the time-periodic one- and two-soliton branches are not connected. Another observation concerns the coexistence of stationary and periodic complexes. At this stage, only a small portion of this bistability domain (indicated by the black mark in Figure 4, *b*) is marked.

Details of the analysis of the complexity, bifurcations and stability of time-periodic solitons at a wide range of parameters γ an h are presented in [24, 25, 80–83].

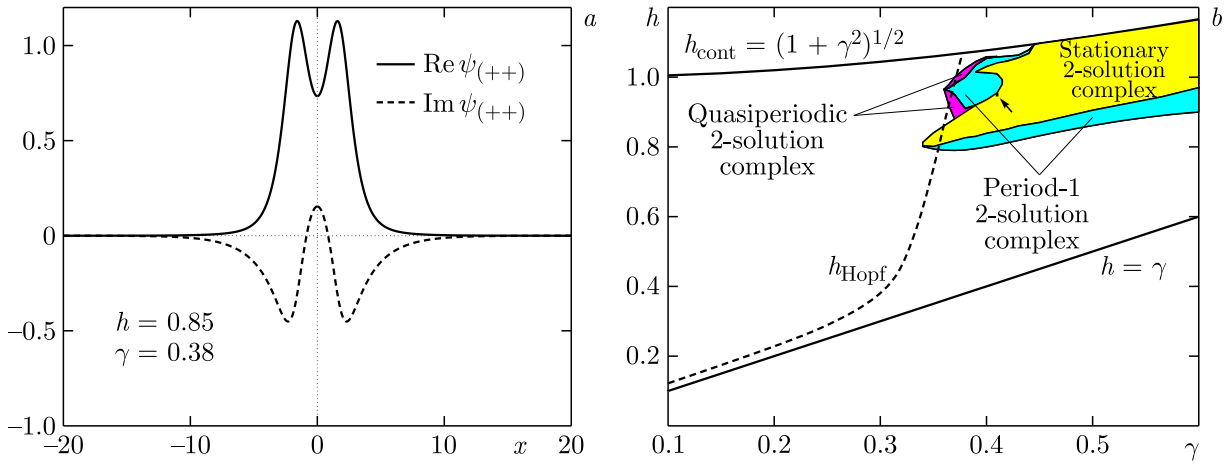

Figure 4. *a*) Stable stationary two-soliton complex for $\gamma = 0.38$, $h = 0.85$. *b*) Two-soliton attractor chart. The black mark (pointed to by the arrow) indicatesthe periodic/stationary bistability region. The dashed curve is the lineof the Hopf bifurcation of the stationary $\psi_+(x)$ soliton.

3.2. ϕ^4 oscillons as standing waves in a ball of finite radius

In this section, the ϕ^4 equation is considered

$$\frac{\partial^2\Phi(r,t)}{\partial t^2} - \Delta\Phi(r,t) - \Phi(r,t) + \Phi^3(r,t) = 0, \quad \Delta = \frac{1}{r^2}\frac{\partial}{\partial r}r^2\frac{\partial}{\partial r}. \tag{59}$$

Eq. (59) is widely used as a model of various physical processes supporting nonlinear waves. Localised long-lived pulsating states in the three-dimensional ϕ^4 theory are known since 1975 [92]. Subsequent computer simulations [93, 94] revealed the formation of long-lived, large-amplitude, localised states that oscillate almost periodically. Such states, termed "oscillons" in [95–98], occur in a number of physical and mathematical applications, including cosmology and relativistic physics, see [26, 99, 100] for review and details.

With their permanent loss of energy to the second-harmonic radiation, oscillons are not exactly time-periodic. In [26], these infinite-space solutions are approximated by standing waves in a ball of a large but finite radius. Unlike oscillons, standing waves are periodic and can be determined as solutions of a BVP on a cylindrical surface. Thus, the spatio-temporal structure and properties of the spherically symmetric oscillon of Eq. (59) are studied by examining the periodic standing wave in a ball of finite radius. For that, a two-dimensional BVP for a nonlinear PDE on the domain $[0,T]\times[0,R]$ (where T is the period, and R is the radius) is formulated. The numerical studies [26, 101, 102] concentrate mainly on the dependence of the spatio-temporal structure of standing waves and their bifurcations on the frequency of pulsation. In [103], we focused on the radius-dependence of the structure and stability properties of ϕ^4 standing waves.

3.2.1. Mathematical statement of a two-dimensional boundary value problem

The study of the spherically symmetric standing wave of ϕ^4 Eq. (59) in a ball of finite radius R can be reduced by $\phi(r,t) = \Phi(r,t) - \Phi_0$ (where $\Phi_0 = -1$ is one of the vacuum solutions as $r \to \infty$) to the consideration of the following BVP in the two-dimensional domain $[0,T]\times[0,R]$:

$$\frac{\partial^2\phi(r,t)}{\partial t^2} - \frac{1}{r^2}\frac{\partial}{\partial r}r^2\frac{\partial\phi(r,t)}{\partial r} + 2\phi(r,t) - 3\phi^2(r,t) + \phi^3(r,t) = 0, \tag{60}$$

$$\left.\frac{\partial\phi(r,t)}{\partial r}\right|_{r=0} = \phi(R,t) = 0, \quad \phi(r,T) = \phi(r,0). \tag{61}$$

Then, letting $\tau = t/T$ and defining $\psi(r,\tau) = \phi(r,t)$ yield a BVP in the two-dimensional domain $[0,1]\times[0,R]$ [101, 102]:

$$\mathcal{L} \equiv \frac{\partial^2\psi(r,\tau)}{\partial\tau^2} + T^2\left(-\frac{1}{r^2}\frac{\partial}{\partial r}r^2\frac{\partial\psi(r,\tau)}{\partial r} + 2\psi(r,\tau) - 3\psi^2(r,\tau) + \psi^3(r,\tau)\right) = 0, \tag{62}$$

$$\left.\frac{\partial\psi(r,\tau)}{\partial r}\right|_{r=0} = \psi(R,\tau) = 0, \quad \psi(r,1) = \psi(r,0). \tag{63}$$

Any solution of Eq. (60) can be characterised by its energy E and its corresponding frequency $\omega = 2\pi/T$:

$$E = 4\pi\int_0^R\left(\frac{1}{2}\left(\frac{\partial\phi(r,t)}{\partial t}\right)^2 + \frac{1}{2}\left(\frac{\partial\phi(r,t)}{\partial r}\right)^2 + \phi^2(r,t) - \phi^3(r,t) + \frac{\phi^4(r,t)}{4}\right)r^2\,dr. \tag{64}$$

If the solution with the frequency ω does not change appreciably as R is increased — in particular, if the energy (64) does not change — one can conclude that this standing wave provides a fairly accurate approximation for the periodic solution in the infinite space.

3.2.2. Numerical approach

The solutions of BVP (62), (63) are path-followed in R for the selected values of T and in T for the selected values of R. The CANM-based computational scheme is similar to that described in Section 3.1.3. Thus, each step of numerical continuation along the branch $E(T)$ or $E(R)$ involves the following stages:

- Calculation of the initial guess for the CANM iteration process using the results at two previous parameter values (analog of formula (53) in Section 3.1.3).
- CANM-calculation of the solution of BVP (62).
- Checking the turning point criterion (analog of the inequality (56) in Section 3.1.3).
- Choice of the value of the parameter increment (analog of formula (55) in Section 3.1.3).

In (53), (55), (56), the parameter R or T should be used instead of h.

Unlike the problem considered in Section 3.1, only the function ψ is unknown, while the period T is a given parameter. For each value of T, BVP (62), (63) is solved numerically using the standard CANM iteration, as described in Section 2. Initially, the derivatives in (62), (63) were approximated by standard second-order three-point finite differences. Later, in order to improve the accuracy of numerical solutions and corresponding Floquet multipliers, the five-point finite difference approximation of the fourth accuracy order was implemented. A system of linear algebraic equations is formed as a result of the discrete approximation of the linear BVP formulated in the standard manner at each CANM iteration and is solved numerically on the basis of the same approach as in 3.1, adapted to the block-pentadiagonal structure of the matrix. The discrete steps in t and r are taken to be $1/100$ and $R/1000$, respectively. At each iteration, the Newtonian iteration parameter τ_k is determined by formula (12) where τ_0=0.9, and the maximal value of τ_k is 1.5. The Newtonian process is terminated when the inequality $||\mathcal{L}|| < \epsilon$ is true. Here $||\cdot||$ is the standard C-norm, and $\epsilon > 0$ is a small number chosen beforehand. Within the numerical procedure providing an initial guess with $||\mathcal{L}|| \sim 0.2$, the CANM calculation takes 4–7 iterations for the case of $\epsilon = 10^{-9}$.

3.2.3. Stability analysis

The stability of the resulting standing waves against spherically symmetric perturbations is classified on the basis of the following linearised equation [26]:

$$\begin{aligned} &\frac{\partial^2 y(r,t)}{\partial t^2} - \frac{1}{r^2}\frac{\partial}{\partial r} r^2 \frac{\partial y(r,t)}{\partial r} - y(r,t) + 3(\phi-1)^2 y(r,t) = 0, \\ &\left.\frac{\partial y(r,t)}{\partial r}\right|_{r=0} = y(R,t) = 0. \end{aligned} \tag{65}$$

Expanding $y(r,t)$ in a Fourier sine series

$$y(r,t) = \sum_{n=1}^{N} u_n(t)\, \sin(k_n r), \quad k_n = \frac{\pi n}{R}, \quad u_n(t) = \frac{2}{R}\int_0^R y(r,t)\, \sin(k_n r)\, dr$$

produces a system of $2N$ ordinary differential equations for Fourier expansion coefficients:

$$\frac{\partial u_m(t)}{\partial t} = v_m(t), \quad \frac{\partial v_m(t)}{\partial t} + \mathcal{F}_m(t) = 0, \quad 1 \leqslant m \leqslant N, \tag{66}$$

where

$$\begin{aligned} \mathcal{F}_m(t) = (2 + k_m^2) u_m(t) - 3\sum_{n=1}^{N} (A_{m-n}(t) - A_{m+n}(t)) u_n(t) \\ + \frac{3}{2}\sum_{n=1}^{N} (B_{m-n}(t) - B_{m+n}(t)) u_n(t), \end{aligned}$$

and $A_{m\pm n}(t)$, $B_{m\pm n}(t)$ are the T-periodic functions of t:

$$A_{m\pm n}(t) = \frac{2}{R}\int_0^R \phi(r,t)\, \cos(k_{m\pm n} r)\, dr, \quad B_{m\pm n}(t) = \frac{2}{R}\int_0^R \phi^2(r,t)\, \cos(k_{m\pm n} r)\, dr.$$

The set of $2N$ linearly independent solutions of system (66), evaluated numerically at $t = T$, forms a monodromy matrix [104]. The standing-wave solution $\phi(r,t)$ is deemed stable if all $2N$ eigenvalues of the monodromy matrix (Floquet multipliers) lie on the unit circle and unstable if there are multipliers outside the unit circle. In our calculations, waves are identified as stable if the absolute values of all Floquet multipliers are smaller 1.005. The parallel MATLAB implementation of the Floquet multiplier calculation provides a speedup of calculations about 20 times compared to serial calculations, see [101] for details of the parallel algorithm.

3.2.4. Results of the numerical study

The numerical continuation of standing waves in T for several values of R shows that the $E(\omega/\omega_0)$ curve consists of a sequence of resonant spikes joined by the low envelope curve. As shown in [26], the number and positions of spikes are R-sensitive while the low envelope curve does not depend on the radii. This is illustrated in Figure 5 where fragments of the $E(\omega/\omega_0)$ diagrams are shown in the cases of $R = 100$ and $R = 150$.

The emergence of spikes in $E(\omega/\omega_0)$ is explained by the resonance between the asymptotic frequencies of two co-existing types of standing waves interconnected via the period doubling

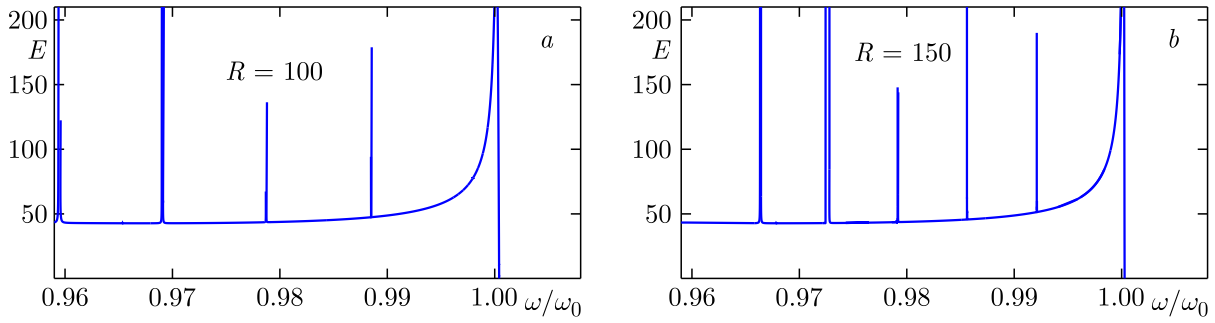

Figure 5. Energy-frequency diagram produced by the numerical continuation of solutions of the BVP (62), (63) for the cases of R=100 (a) and R=150 (b).

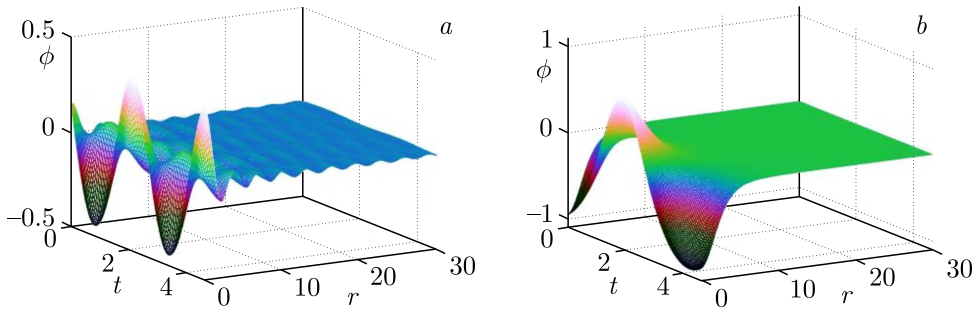

Figure 6. Functions $\phi(r,t)$ for two coexisting waves at $R = 150$, $\omega = 0.9802\omega_0$: a) the Bessel-like wave, b) "standard" wave.

bifurcation. The first type is the "standard" nonlinear standing wave with an exponentially localised pulsating core and a small-amplitude slowly decaying second-harmonic tail. The second type is the Bessel-like wave without an explicitly localised core, which branches off the zero solution and decays in proportion to r^{-1} as $r \to R$. The two types of waves are demonstrated in Figure 6 in the case of $R = 150$, $\omega = 0.9802\omega_0$. The spike structure, where the branches $E(\omega/\omega_0)$ of the two types of waves interconnect is analysed in [26].

Another observation is that the $E(\omega/\omega_0)$ function has a single minimum which is the same for all values of R: $\omega_{\min} = \omega/\omega_0 = 0.967$, $E_{\min} = 42.74$. This minimum is clearly seen in Figure 7 (left panel). This Figure demonstrates a fragment of the energy-frequency diagram obtained in the numerical continuation of ϕ^4 standing waves in the case of $R = 100$ from $\omega/\omega_0 = 1$ to lower frequencies. Our numerical study shows that the location of regions of stability of standing waves to spherically symmetric perturbations depends on R, but all stability regions exist only for frequencies lower than $\omega_{\min}$.

To clarify the properties of the $E(R)$-function in dependence on frequency, various values of ω are chosen, and standing waves from $R = 100$ in the $R > 100$ direction are path-followed. Four representative values of frequencies are denoted by brown circles in Figure 8 (left panel). One of the points, $\omega/\omega_0 = 0.973$, is larger than $\omega_{\min}$. The other frequencies are smaller than $\omega_{\min}$.

Our calculations reveal the periodic structure of the $E(R)$ curves, which consist of alternating energy peaks and "flat" regions. The right panel of Figure 8 demonstrates the interconnection of the coexisting $E(R)$ branches in the region of the $E(R)$-peak for the case of $T = 4.8$ ($\omega = 0.9256\omega_0$). The branches of "standard" nonlinear waves are shown by solid lines, the dashed line represents the branch of the Bessel-like wave. Both slopes of the $E(R)$ peak in the right panel of Figure 8 join the branch of the Bessel-like waves at period-doubling bifurcation

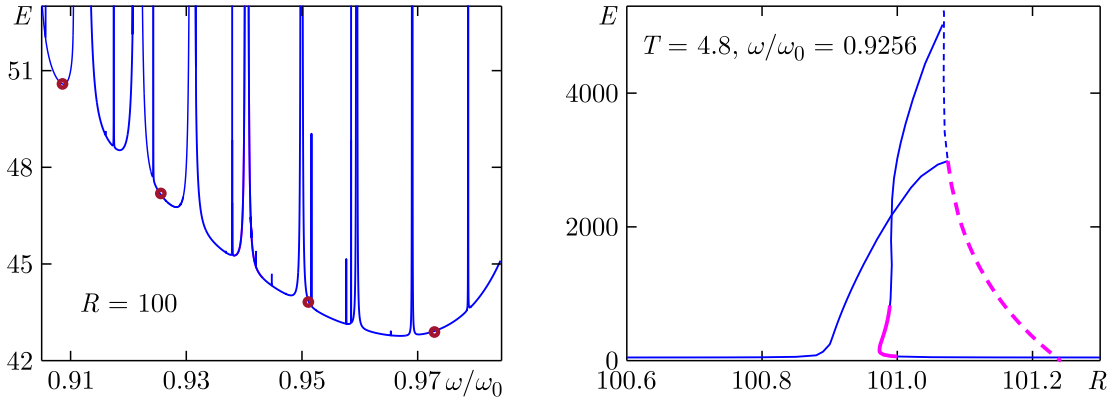

Figure 7. Left: fragment of the $E(\omega/\omega_0)$ diagram from [26]. The brown circles indicate the values of ω/ω_o used in R-pathfollowing plotted in Figure 8. Right: interconnection of the $E(R)$ branches of coexisting waves in the region of the energy peak. The solid lines correspond the "standard" nonlinear wave, the dashed curve shows the Bessel-like branch. The stability regions are marked by thick (solid and dashed) magenta lines.

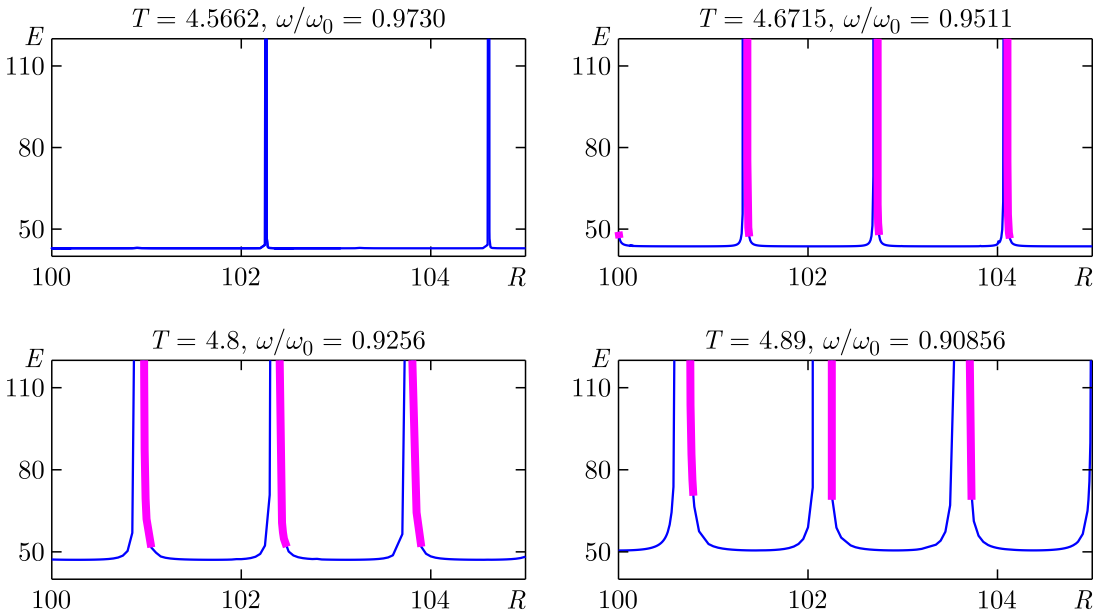

Figure 8. $E(R)$ curves for the frequencies which are marked by brown circles in the $E(\omega/\omega_0)$ diagram (Figure 7, right panel). The thick magenta lines show regions of stability.

points. The Bessel-like wave is stable in the interval between zero energy and the lowest bifurcation point. This interval is shown by the thick magenta dashed line. The stable region of the "standard" wave marked by the thick magenta solid line lies between $E = 51.0881$ and $E = 811.0981$.

The $E(R)$ curves for various values of frequencies marked in the right panel of Figure 8 the are plotted in Figure 8. It is seen that the distance between the peaks depends on ω. Stability intervals are also periodically repeated and located at the foot of the right slopes of the energy peaks. They are marked by thick magenta lines in Figure 8. The regions of stability of standing waves on the $E(R)$ diagram are found only for the case of $\omega/\omega_0 < \omega_{\min}$:

Table 1. Period of the $E(R)$ function and minimum energy of stability depending on ω/ω_0

ω/ω_0	0.9730	0.9511	0.9256	0.9086
T	4.5662	4.6715	4.800	4.8900
Period of the $E(R)$ function	1.3847	1.3786	1.4335	1.4771
Minimum value of E where the "standard" wave is stable		46.3212	51.0881	68.4974

$\omega/\omega_0 = 0.9511, 0.9256, 0.90856$. It is noteworthy that the minimum energy at which the standing wave can be stable increases as ω decreases, see Table 1.

3.2.5. Summary to Section 3.2

The CANM-based numerical study shows that, despite the fact that the number and positions of the spikes of the $E(\omega/\omega_0)$ diagram are R-sensitive, the energy curve can be considered as an approximation of the radius-independent envelope of nearly-periodic oscillons in the infinite space. The existence of energy spikes on both the $E(R)$ and $E(\omega/\omega_0)$ dependences is due to the resonance between the asymptotic frequencies of two co-existing types of standing waves.

A periodical dependence of the structure and properties of ϕ^4 standing waves on the radius is established. The distance between the E-peaks of the $E(R)$ functions is frequency-dependent. For each $\omega/\omega_0 < \omega_{\min}$, there is an equidistant sequence of R for which standing waves are stable. It is established that for ω/ω_0 in the [0.85, 1.0] range, the minimum energy E for which standing waves are stable increases as the frequency decreases. This hypothesis needs to be numerically confirmed for lower values of ω.

The results of a study of three-dimensional oscillons in the ϕ^4 theory based on their approximation by standing waves in a sphere of finite radius are presented in [26, 101–103]. Research in this area is currently ongoing.

4. CANM in the numerical study of few-body complex physical systems

This Section is devoted to the applications of CANM for numerical study of three physical problems.

The first problem concerns the ionization of helium by fast electrons and protons. The corresponding matrix elements contain the wave function of the ground state of helium and are expressed as multi-dimensional integrals in the coordinate space. In Section 4.1, the possibilities of constructing a multi-parametric ground state wave function, which provides good accuracy to the ground state energy of helium using few variational exponential basis functions, are studied. The corresponding generalized eigenvalue problem is solved by CANM with the optimal choice of the iteration parameter algorithm described in Section 2.4.1.

The second problem, related to the calculation of the spectra of the ground and metastable states of the beryllium dimer by the high-order FEM, is considered in Section 4.2. The calculation of the spectrum of complex-valued eigenenergies of the metastable state problem is reduced to the generalized eigenvalue problem in which the stiffness matrix depends on the sought eigenvalue. To solve this problem, CANM with the optimal choice of the iteration parameter algorithm described in Section 2.4.2 is used.

The last problem is calculations of the $1\sigma_g$ state relativistic energy of the one-electron two-center Coulomb Dirac equation using Slater-type orbitals with non-integer principal quantum numbers. Relativistic approaches oriented to the calculation of properties of heavy atoms which

start with the Dirac Hamiltonian encounter difficulties directly related to the presence of the negative energy continuum in the Dirac spectrum. Section 4.3 presented an iterative scheme for the minimax procedure based on CANM in combination with negative curvature direction methods, which do not give spurious solutions for the Dirac Hamiltonian.

4.1. Ionization process of helium by fast electron and proton impact

In [105–108] there is a discussion about the influence of cusp conditions on the differential cross sections (DCSs) of (e,3e) reactions. In this model, the helium final state is treated using a 3C wave function [109], which contains the product of three two-particle Coulomb waves, and the ground state is given by the Pluvinage (PL) wave function [110, 111]

$$\Psi(r_1,r_2,r_{12}) = \Psi_{PL}(r_1,r_2,r_{12}) = N_{PL} e^{-Z(r_1+r_2)} e^{-\imath k r_{12}} {}_1F_1\left(1-\imath\frac{1}{2k},2,2\imath k r_{12}\right), \tag{67}$$

where r_i is the distance between the nucleus and the i-th electron ($i=1,2$) and r_{12} is the distance between the electrons; ${}_1F_1(a,b,c)$ is the confluent hypergeometric function; N_{PL} is the normalization constant; k is the variational parameter; and $Z=2$ for helium. This wave function satisfies the cusp conditions of Kato [112]:

$$\frac{\partial\Psi(r_1,r_2,r_{12})}{\partial r_i}\bigg|_{r_i\to 0} \Big/ \Psi(r_1,r_2,r_{12})|_{r_i\to 0} = -Z, \quad \frac{\partial\Psi(r_1,r_2,r_{12})}{\partial r_{12}}\bigg|_{r_{12}\to 0} \Big/ \Psi(r_1,r_2,r_{12})|_{r_{12}\to 0} = \frac{1}{2}, \tag{68}$$

where $i=1,2$. However, from the spectroscopic point of view, it gives a poor accuracy for the ground state energy, $E_{PL} = -2.878\,8$ au at $k=0.410$. At the same time, the proposed model surprisingly well describes the most of experimental data by Lahmam-Bennani et al. [113], in which the coplanar $(e,3e)$ angular distributions of double ionization of helium are measured at an incident radiation energy of 5.6 keV and a small projectile scattering angle of 0.45°. In [105] there are proposed two more wave functions also giving poor energy values while satisfying Kato's cusp conditions, which similarly describe the experiment well. In this connection, the employment of "poor" wave functions is mainly conditioned by difficulties in constructing a variational wave function that gives an accurate energy value while satisfying the cusp conditions.

4.1.1. Construction of a helium ground state wave function on the exponential basis

To clarify the evolving discussion, two relatively simple wave functions satisfying Kato's cusp conditions and yielding an accurate energy value are constructed. Variational wave functions are chosen in the form intensively exploited in [114, 115]

$$\Psi(r_1,r_2,r_{12}) = \sum_{j=1}^{N} D_j \left(e^{-\alpha_j r_1-\beta_j r_2} + e^{-\alpha_j r_2-\beta_j r_1}\right) e^{-\gamma_j r_{12}}, \tag{69}$$

where the real positive parameters α_j, β_j, and γ_j are generated in a quasirandom manner for the given number N of the basis functions:

$$\begin{aligned}
\alpha_j &= \left\{\frac{1}{2}j(j+1)\sqrt{p_\alpha}\right\}(A_2-A_1)+A_1, \quad 0\leqslant A_1<A_2,\\
\beta_j &= \left\{\frac{1}{2}j(j+1)\sqrt{p_\beta}\right\}(B_2-B_1)+B_1, \quad 0\leqslant B_1<B_2,\\
\gamma_j &= \left\{\frac{1}{2}j(j+1)\sqrt{p_\gamma}\right\}(C_2-C_1)+C_1, \quad 0\leqslant C_1<C_2.
\end{aligned} \tag{70}$$

Here $\{x\}$ is the fractional part of x. $[A_1, A_2]$, $[B_1, B_2]$ and $[C_1, C_2]$ are the variational intervals to be optimized. p_α, p_β and p_γ are some prime numbers. The values $p_\alpha = 2$, $p_\beta = 3$ and $p_\gamma = 5$ are used. It should be noted that the final results for α_j, β_j, and γ_j are practically insensitive to the variation of the above prime numbers.

In the perimetrical (radial) coordinates for two-electron S states the non-relativistic Hamiltonian in the case of infinite nuclear mass takes the form

$$H(r_1, r_2, r_{12}) = -\frac{1}{2}\left(\frac{1}{r_1^2}\frac{\partial}{\partial r_1}r_1^2\frac{\partial}{\partial r_1} + \frac{1}{r_2^2}\frac{\partial}{\partial r_2}r_2^2\frac{\partial}{\partial r_2}\right) - \frac{1}{r_{12}^2}\frac{\partial}{\partial r_{12}}r_{12}^2\frac{\partial}{\partial r_{12}} - \\ -\frac{r_1^2 - r_2^2 + r_{12}^2}{2r_1 r_{12}}\frac{\partial^2}{\partial r_1 \partial r_{12}} - \frac{r_2^2 - r_1^2 + r_{12}^2}{2r_2 r_{12}}\frac{\partial^2}{\partial r_2 \partial r_{12}} - \frac{Z}{r_1} - \frac{Z}{r_2} + \frac{1}{r_{12}}. \tag{71}$$

The radial part of the integration volume element can be rewritten in the following way:

$$\int \boldsymbol{dr}_1 \int \boldsymbol{dr}_2 F(r_1, r_2, r_{12}) = 8\pi^2 \int_0^\infty r_1 dr_1 \int_0^\infty r_2 dr_2 \int_{|r_1 - r_2|}^{r_1 + r_2} r_{12} dr_{12} F(r_1, r_2, r_{12}). \tag{72}$$

The matrix elements $\mathbf{A}$ and $\mathbf{B}$ of the corresponding generalized eigenvalue problem

$$\mathbf{A}\boldsymbol{D} = E\mathbf{B}\boldsymbol{D}, \quad \boldsymbol{D} = (D_1, \ldots, D_N)^T, \tag{73}$$

with given variational parameters A_1, A_2, B_1, B_2, C_1, and C_2 consist of three-dimensional integrals, where "^{T}" denotes the transpose of the vector. They are reduced to the analytical form using the Fourier transform with respect to the variable r_{12}.

In principle, one can supplement the variational procedure with Kato's cusp conditions (68). However, this is extremely difficult to realize in practice, since in this case the wave function (69) should satisfy the two-particle cusp ratios locally, i.e., in each two-particle coalescence point of configuration space. Therefore, in the variational procedure, the averaged two-particle cusp ratios, which follow from Eq. (68) and traditionally occur in variational calculations (see, for instance, [114]), are utilized:

$$\nu_i = \frac{\left\langle \Psi(r_1, r_2, r_{12}) \middle| \delta(\boldsymbol{r}_i) \middle| \dfrac{\partial \Psi(r_1, r_2, r_{12})}{\partial r_i} \right\rangle}{\langle \Psi(r_1, r_2, r_{12}) | \delta(\boldsymbol{r}_i) | \Psi(r_1, r_2, r_{12}) \rangle} = -Z, \\ \nu_{12} = \frac{\left\langle \Psi(r_1, r_2, r_{12}) \middle| \delta(\boldsymbol{r}_{12}) \middle| \dfrac{\partial \Psi(r_1, r_2, r_{12})}{\partial r_{12}} \right\rangle}{\langle \Psi(r_1, r_2, r_{12}) | \delta(\boldsymbol{r}_{12}) | \Psi(r_1, r_2, r_{12}) \rangle} = \frac{1}{2}, \tag{74}$$

where $i = 1, 2$. These two-particle cusp conditions can be regarded as "weak", since they are less stringent than those given by Eq. (68). The wave function satisfying the two-particle cusp conditions given by Eq. (74) will be referred to as 2PC. From Kato's cusp conditions (68), one can also derive cusp ratios in the three-particle coalescence point. They are given by [116, 117]:

$$\mu_i = \frac{\left.\dfrac{\partial \Psi(r_1, r_2, r_{12})}{\partial r_i}\right|_{r_1, r_2, r_{12} \to 0}}{\Psi(r_1, r_2, r_{12})|_{r_1, r_2, r_{12} \to 0}} = -Z, \quad \mu_{12} = \frac{\left.\dfrac{\partial \Psi(r_1, r_2, r_{12})}{\partial r_{12}}\right|_{r_1, r_2, r_{12} \to 0}}{\Psi(r_1, r_2, r_{12})|_{r_1, r_2, r_{12} \to 0}} = \frac{1}{2}. \tag{75}$$

where $i = 1, 2$. The wave function satisfying these three-particle cusp conditions will be referred to as 3PC.

To find variational parameters, the Newton-type minimization method [118] is used for the function:

$$F(A_1, A_2, B_1, B_2, C_1, C_2) = E - E_{\text{upper}} + \begin{cases} (\nu_1 + Z)^2 + \left(\nu_{12} - \dfrac{1}{2}\right)^2, & \text{for Eq. (74)}, \\ (\mu_1 + Z)^2 + \left(\mu_{12} - \dfrac{1}{2}\right)^2, & \text{for Eq. (75)}. \end{cases} \tag{76}$$

Here E_{upper} is the upper estimate of the ground state energy and is equal to $-2.903\,724\,377$ au [119].

In the above minimization procedure (76), CANM with the optimal choice of the iteration parameter for calculating the generalized eigenvalue problem (73), as described in section 2.4.1, is used as an internal iteration. Numerical experiments confirm that the optimal iteration parameter from the interval $(0, 2)$ provides the best convergence with respect to the iteration number compared to other algorithms with an iteration parameter in the interval $(0, 1)$. This advantage allows one to speed up the calculation of the generalized eigenvalue problem (73) with different variational parameters A_1, A_2, B_1, B_2, C_1, and C_2 for the minimization procedure (76).

Table 2 presents the minimized helium ground state energy E (in au) and the calculated values of $\nu_1 = \nu_2$, ν_{12} for the optimized parameters A_1, A_2, B_1, B_2, C_1 and C_2 in the case of 2PC conditions (74) for different values of N in Eq. (69). For comparison, the values $\mu_1 = \mu_2$, μ_{12} are also given. Table 3 presents the analogous results in the case of 3PC conditions (75). As seen, in both cases the calculated cusp ratios for $N = 60$ are in good agreement with the exact ones, $E = -2.903\,724$ au, $\nu_1 = \nu_2 = -2$, $\nu_{12} = 0.5$ and $E = -2.903\,721$ au, $\mu_1 = \mu_2 = -2$, $\mu_{12} = 0.5$, respectively. It is also noteworthy that if the 2PC and 3PC conditions are ignored,

Table 2. Minimized ground state energy E (in au) and calculated values of $\nu_1 = \nu_2$, ν_{12} for optimized parameters as functions of N in the case of 2PC conditions. For comparison, the values $\mu_1 = \mu_2$, μ_{12} are also given.

N	E	$\nu_1 = \nu_2$	ν_{12}	$\mu_1 = \mu_2$	μ_{12}
10	$-2.903\,630\,0$	-1.9999	0.4999	-1.9319	0.4425
20	$-2.903\,704\,9$	-2.0000	0.5000	-1.9356	0.4112
30	$-2.903\,720\,0$	-2.0000	0.5000	-1.9594	0.4238
40	$-2.903\,720\,8$	-1.9999	0.4999	-1.9538	0.4557
50	$-2.903\,723\,1$	-2.0000	0.5000	-1.9513	0.4476
60	$-2.903\,724\,2$	-1.9999	0.4999	-1.9550	0.4625

Table 3. Minimized ground state energy E (in au) and calculated values of $\mu_1 = \mu_2$, μ_{12} for optimized parameters as functions of N in the case of 3PC conditions. For comparison, the values $\nu_1 = \nu_2$, ν_{12} are also given.

N	E	$\mu_1 = \mu_2$	μ_{12}	$\nu_1 = \nu_2$	ν_{12}
10	$-2.903\,315\,9$	-1.9999	0.4999	-1.9925	0.6125
20	$-2.903\,649\,4$	-2.0000	0.4999	-2.0034	0.5288
30	$-2.903\,691\,1$	-2.0000	0.4999	-2.0106	0.4803
40	$-2.903\,696\,1$	-1.9999	0.5000	-1.9991	0.5135
50	$-2.903\,708\,3$	-1.9999	0.4999	-2.0062	0.5345
60	$-2.903\,721\,1$	-2.0000	0.4999	-2.0020	0.5019

then the minimized ground state energy E is equal to $-2.903\,717$ au and $-2.903\,724$ au already for $N = 10$ and 20, respectively.

Our numerous calculations of the DCSs for various ionization processes using different types of variational helium ground state wave functions, such as

1. weakly correlated wave functions with a poor accuracy of the ground state energy and not satisfying Kato's cusp conditions (68) and the 2PC (74), 3PC (75) conditions: the Hylleraas ($E = -2.847\,7$ au) [120], the Roothaan-Hartree-Fock ($E = -2.861\,7$ au) [121], the Hylleraas-Eckart-Chandrasehkar ($E = -2.875\,7$ au) [122–124], and the Silverman-Platas-Matsen ($E = -2.895\,2$ au) [125];
2. the Pluvinage wave function (67) with a poor accuracy of the ground state energy ($E = -2.878\,8$ au) while satisfying Kato's cusp conditions (68) and the 2PC (74), 3PC (75) conditions;
3. highly correlated wave functions with a good accuracy of the ground state energy but not satisfying Kato's cusp conditions (68) and the 2PC (74), 3PC (75) conditions: the Mitroy ($E = -2.903\,1$ au) [126], the Bonham-Kohl ($E = -2.903\,5$ au) [127], and (69) at $N = 10$ ($E = -2.903\,7$ au);
4. highly correlated wave functions (69) at $N = 60$ with a good accuracy of the ground state energy ($E = -2.903\,7$ au) and satisfying the 2PC (74) or 3PC (75) conditions,

show that all wave functions that provide a good accuracy of the energy give very similar results, while wave functions that provide a poor accuracy of the energy give different results. It follows that for DCS calculations it is important to use correlated variational wave functions, which give a good accuracy of the ground state energy, regardless of whether they satisfy Kato's cusp conditions or not.

After that, further calculations using the wave function (69) at $N = 10$, which gives the ground state energy $E = -2.903\,717$ au, were performed and several important physical results for the single and double ionization processes of helium by electron and proton impact, presented in [128–137], etc., were obtained. Some startling results of these applications are considered in Sections 4.1.2 and 4.1.3.

The main advantage of this wave function is that with a relatively small number of basis functions it gives the ground state energy of helium with an accuracy of 10^{-7} compared to, for example, the highly correlated configuration interaction wave function Mitroy [126], which consists of more than 550 terms, with $E = 2.903\,146$ au. Another advantage is that, due to the positive parameters of γ_j, the Fourier transform can be used to reduce the multiplicity of scattering amplitude integrals for some ionization processes.

4.1.2. Numerical results: single ionization of helium by fast proton impact

In this section, the problem of single ionization of helium by a fast proton with an energy of 1 MeV is considered. This energy allows the proton to be described by a plane wave. In [131], the energy of the ejected electron is $E_e = 6.5$ eV. The corresponding experiment was performed at the Institut für Kernphysik, University of Frankfurt, Germany.

In the following, unless otherwise stated, atomic units are used, i.e., $e = m_e = \hbar = 1$.

The value of the momentum transfer $\boldsymbol{Q} = \boldsymbol{p}_i - \boldsymbol{p}_s$ is rather small, namely $Q = 0.75$ au. The law of momentum conservation

$$\boldsymbol{Q} + \boldsymbol{p}_e + \boldsymbol{K}_{\rm ion} = 0, \tag{77}$$

illustrates that the velocity of the residual ion $K_{\rm ion}/(m_N + 1)$ is negligible, considering its comparably high mass ($m_N \approx 4m_p = 7344.6$ au). This enables to assume it to be at rest during

the reaction and to choose it as the center of the laboratory coordinate system. Here $\boldsymbol{p}_i$, $\boldsymbol{p}_s$ are the incident and scattered projectile momenta, and $\boldsymbol{p}_e$ is the ejected-electron momentum.

The matrix element is given by:

$$T_{fi} = \sqrt{2} Z_p \int \boldsymbol{dR} \int \boldsymbol{dr}_1 \int \boldsymbol{dr}_2 \Psi_f^{-*}(\boldsymbol{R}, \boldsymbol{r}_1, \boldsymbol{r}_2; \boldsymbol{p}_s, \boldsymbol{p}_e) \Phi_i(\boldsymbol{r}_1, \boldsymbol{r}_2) \times \\ \times e^{\imath \boldsymbol{R} \cdot \boldsymbol{p}_i} \left(\frac{2}{R} - \frac{1}{|\boldsymbol{R} - \boldsymbol{r}_1|} - \frac{1}{|\boldsymbol{R} - \boldsymbol{r}_2|} \right). \tag{78}$$

The factor $\sqrt{2}$ accounts for the identity of the electrons labeled as 1 and 2. The wave function $\Phi_i(\boldsymbol{r}_1, \boldsymbol{r}_2)$ describes helium in its initial (ground) state, and $\Psi_f^-(\boldsymbol{R}, \boldsymbol{r}_1, \boldsymbol{r}_2; \boldsymbol{p}_s, \boldsymbol{p}_e)$ is the wave function of the full Hamiltonian with final boundary conditions describing the singly ionized state. $\boldsymbol{R}$ corresponds to the distance between heavy particles within the immovable nucleus model.

The energy conservation law

$$E = \frac{p_i^2}{2m_p} + \varepsilon_0^{He} = \frac{(\boldsymbol{p}_i - \boldsymbol{Q})^2}{2m_p} + \varepsilon_0^{He^+} + \frac{p_e^2}{2} + \frac{K_{\rm ion}^2}{2(m_N + 1)} \tag{79}$$

allows one to obtain the longitudinal and transversal components of the momentum transfer with respect to the incident proton momentum, $Q_z = (-\varepsilon_0^{He} + \varepsilon_0^{He^+} + E_e)/v_p = 0.18$ au and $Q_\perp \approx m_p v_p \theta_s = 0.73$ au, respectively, where θ_s is the scattering angle of the proton. In Eq. (79), the $Q^2/(2m_p)$ and $K_{\rm ion}^2/(2(m_N + 1))$ terms are neglected, in line with our frozen nucleus approximation.

The final state of the reaction contains three charged particles in the continuum, namely p, e, and the He^+ ion.

First of all, simple models for the initial and final state wave functions are chosen. The final state wave function is described by:

$$\Psi_f^-(\boldsymbol{R}, \boldsymbol{r}_1, \boldsymbol{r}_2; \boldsymbol{p}_s, \boldsymbol{p}_e) = e^{\imath \boldsymbol{R} \cdot \boldsymbol{p}_s} \, \Phi_f^-(\boldsymbol{r}_1, \boldsymbol{r}_2; \boldsymbol{p}_e). \tag{80}$$

In turn, the final He state with one-electron in the continuum wave function $\Phi_f^-(\boldsymbol{r}_1, \boldsymbol{r}_2; \boldsymbol{p}_e)$ has the form

$$\Phi_f^-(\boldsymbol{r}_1, \boldsymbol{r}_2; \boldsymbol{p}_e) = \psi^C(\boldsymbol{r}_1; \boldsymbol{p}_e) \psi_0^{\rm He^+}(\boldsymbol{r}_2). \tag{81}$$

Here

$$\psi_0^{\rm He^+}(\boldsymbol{r}_2) = \sqrt{\frac{8}{\pi}} \, e^{-2r_2} \tag{82}$$

is a hydrogen-like He^+ ground state wave function, and

$$\psi^C(\boldsymbol{r}_1; \boldsymbol{p}_e) = e^{-\pi\zeta/2} \, \Gamma(1 - \imath\zeta) e^{\imath \boldsymbol{p}_e \cdot \boldsymbol{r}_1} \, {}_1F_1(\imath\zeta, 1, -\imath(p_e r_1 + \boldsymbol{p}_e \cdot \boldsymbol{r}_1)) \tag{83}$$

is the wave function of the ejected electron in the Coulomb field of the residual He^+ ion with $\zeta = -1/p_e$.

The helium ground state $\Phi_i(\boldsymbol{r}_1, \boldsymbol{r}_2)$ is presented by two variational wave functions: a weakly correlated Roothaan-Hartree-Fock wave function (RHF) [121] (we call it FBA for brevity, and here both the ground and final helium states are loosely correlated) and a strongly correlated wave function (69) (we call this model CFBA, and here the helium ground state is highly correlated, but its single continuum final state is still loosely correlated). Numerical calculations

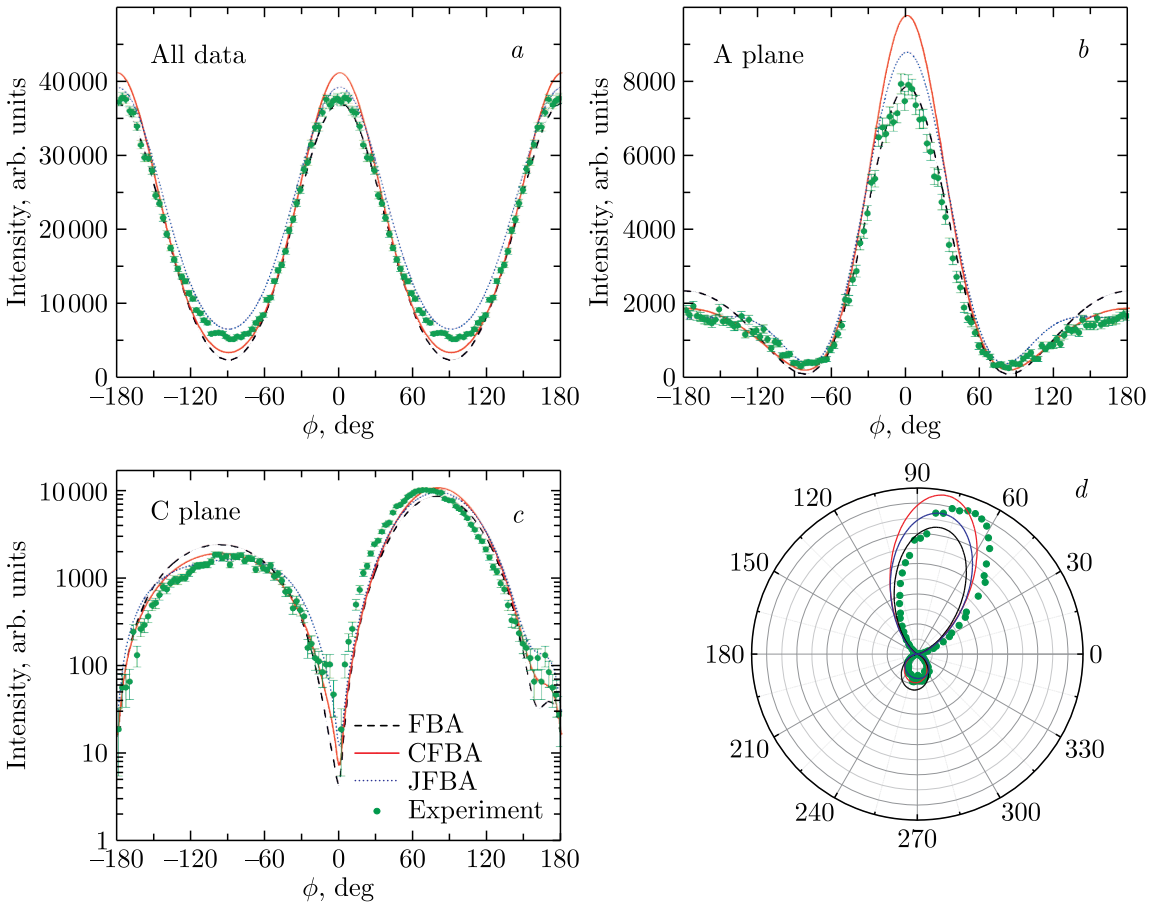

Figure 9. Experimental (green dots) and calculated (FBA, black line, JFBA, blue line, CFBA, red line) electron angular distribution for $E_e = 6.5\,\text{eV}$, $q = 0.75\,\text{au}$. (a) All data; (b) azimuthal plane ($\theta_e = 90° \pm 10°$); (c), (d) coplanar geometry ($\phi_e = 90° \pm 10°$).

of $\Phi_i(\boldsymbol{r}_1, \boldsymbol{r}_2)$ and $\Phi_f^-(\boldsymbol{r}_1, \boldsymbol{r}_2; \boldsymbol{p}_e)$ within the J-matrix approach [138] (JFBA, where both the ground and final state wave functions are highly correlated) are also performed.

The angular distribution integrated over θ_e as a function of ϕ_e is shown in Figure 9, *a*. For quantitative comparison, the experimental data are normalized to the integral of CFBA calculations. The FBA calculation has a slightly lower (7 %) total cross section, while the JFBA theory has a slightly larger (8 %) total cross section. Figure 9, *c* shows the electron angular distribution in the coplanar geometry, also known as the scattering plane. To illustrate good agreement between experiment and theory, the data are presented on a logarithmic scale (and as a polar plot in Figure 9, *d*).

Figure 9, *b* shows the angular distribution in the azimuthal plane. The simple FBA best agrees with the experimental data. It should be pointed out that due to the tilt of the binary lobes between theory and experiment, the direct comparison does not reflect its quality in this plane. The deviation is simply the result of different tilts.

4.1.3. Numerical results: Compton scattering near the threshold

In this section, the Compton ionization of helium, as described in [135], is considered. The photon energy is $E_1 = 2.1$ keV, and the energies of the emitted electrons range from 1 to 50 eV. The corresponding experiment was performed at the P04 beamline of the PETRA III synchrotron at DESY in Hamburg, Germany.

The energy and momentum conservation laws are of the form

$$E_1 = E_2 + I_p + E_e + E_{\rm ion}, \quad \boldsymbol{p}_1 = \boldsymbol{p}_2 + \boldsymbol{p}_e + \boldsymbol{p}_{\rm ion}, \tag{84}$$

where $I_p = 0.9$ au is the ionization potential, E_e ($\boldsymbol{p}_e$) is the energy (momentum) of the escaped electron, $E_{\rm ion}$ ($\boldsymbol{p}_{\rm ion}$) is the energy (momentum) of the residual ion, and E_1 ($\boldsymbol{p}_1$), E_2 ($\boldsymbol{p}_2$) are the energies (momenta) of the incoming and outgoing photons, respectively. For the given keV photon energy range, the momenta are of the order $p_i = E_i/c \sim 1$ au ($i = 1, 2$) with the speed of light $c = \alpha^{-1}$. Since $M_{\rm ion} \gg 1$, the ionic kinetic energy $E_{\rm ion} = \boldsymbol{p}_{\rm ion}^2/(2M_{\rm ion})$ can be neglected. Hence, the photon energy is nearly unchanged and the ratio of the photon energy after and before the collision is

$$t = \frac{E_2}{E_1} = 1 - \frac{I_p + E_e + E_{\rm ion}}{E_1} \approx 1. \tag{85}$$

The transferred momentum from the photon to the atomic system is given by $\boldsymbol{Q} = \boldsymbol{p}_1 - \boldsymbol{p}_2 = \boldsymbol{p}_e + \boldsymbol{p}_{\rm ion}$. The magnitude and direction of the transferred momentum $\boldsymbol{Q}$ can be expressed as a function of the scattering angle θ between the incoming and outgoing photons.

Under the above kinematic conditions, one can use a non-relativistic description and only the so-called A^2 (seagull) term from the total second-order Kramers-Heisenberg-Waller matrix element, well presented, for example, in [139]. In this case, the fully differential cross section (FDCS) can be written as

$$\frac{d^3\sigma}{dE_e\, d\Omega_e\, d\Omega_2} = r_e^2\, p_e\, t\, \frac{1}{(2\pi)^3} |M(\boldsymbol{Q}, \boldsymbol{p}_e)|^2, \tag{86}$$

with the classical electron radius r_e. The matrix element has the form

$$M(\boldsymbol{Q}, \boldsymbol{p}_e) = (\boldsymbol{e}_1 \cdot \boldsymbol{e}_2) \left\langle \Psi_f^{(-)}(\boldsymbol{r}_1, \boldsymbol{r}_2; \boldsymbol{p}_e) \left| \sum_{j=1}^{2} e^{\imath \boldsymbol{Q}\cdot\boldsymbol{r}_j} \right| \Psi_i(\boldsymbol{r}_1, \boldsymbol{r}_2) \right\rangle, \tag{87}$$

where $\boldsymbol{e}_1$, $\boldsymbol{e}_2$ are the polarization vectors of the incoming and outgoing photons. Here the initial state $\Psi_i(\boldsymbol{r}_1, \boldsymbol{r}_2)$ is the helium ground state wave function, and the final state is the scattering state wave function $\Psi_f^{(-)}(\boldsymbol{r}_1, \boldsymbol{r}_2; \boldsymbol{p}_e)$ with the one-electron continuum state (corresponding to the asymptotic electron momentum $\boldsymbol{p}_e$), while the second helium electron remains bound.

Assuming the incoming photon beam is unpolarized and the final polarization state of the outgoing photon is not detected, we additionally average over the initial polarization and sum up the probabilities corresponding to both possible final polarizations. Under these assumptions, the FDCS can be written as

$$\frac{d^3\sigma}{dE_e\, d\Omega_e\, d\Omega_2} = \left(\frac{d\sigma}{d\Omega_2}\right)_{\rm Th} p_e\, t\, \frac{1}{(2\pi)^3} |M_e(\boldsymbol{Q}, \boldsymbol{p}_e)|^2 \tag{88}$$

with the Thompson cross section

$$\left(\frac{d\sigma}{d\Omega_2}\right)_{\rm Th} = \frac{1}{2} r_e^2 (1 + \cos^2\theta) \tag{89}$$

for photons scattered off a single free electron and the electronic matrix element

$$M_e(\boldsymbol{Q}, \boldsymbol{p}_e) = \left\langle \Psi_f^{(-)}(\boldsymbol{r}_1, \boldsymbol{r}_2; \boldsymbol{p}_e) \left| \sum_{j=1}^{2} e^{\imath \boldsymbol{Q}\cdot\boldsymbol{r}_j} \right| \Psi_i(\boldsymbol{r}_1, \boldsymbol{r}_2) \right\rangle. \tag{90}$$

It should be noted that, the A^2 approximation resembles the first Born approximation (FBA) for the scattering of a fast particle on an atom. Therefore, the observed effects have an analogous interpretation and can be described in familiar terms. However, the Compton ionization has some advantages over traditional mechanisms such as $(e, 2e)$ ionization, namely:

1. the contribution of other second-order terms is very small so that the A^2 approximation is often accurate;
2. the photon has no charge so that it is necessary to consider only the evolution of the field-free system of charged particles;
3. the transferred momentum $\boldsymbol{Q}$ can vary in a wide range so that different regimes are accessible.

Complementary approaches are used to calculate electronic matrix elements. **Approach I** describes both electrons and takes into account correlation in the ground state, but uses Coulomb waves as scattering states. In contrast, **Approach II** uses a single-active-electron description, but includes accurate one-electron scattering states.

In **Approach I**, the initial state is given by the correlated symmetric two-electron ground state wave function $\Psi_i(\boldsymbol{r}_1, \boldsymbol{r}_2)$ (69). To approximate the final state, the main idea is that one-electron remains bound in the ionic ground state wave function given by $\psi_0^{\mathrm{He}^+}(\boldsymbol{r})$ (82), and the free electron can be approximated by the Coulomb wave function $\psi^C(\boldsymbol{r}; \boldsymbol{p}_e)$ (83). Since the correct scattering state wave function $\Psi_f^{(-)}(\boldsymbol{r}_1, \boldsymbol{r}_2; \boldsymbol{p}_e)$ must be orthogonal to the initial bound state wave function $\Psi_i(\boldsymbol{r}_1, \boldsymbol{r}_2)$, for the resulting symmetrized final state wave function

$$\tilde{\Psi}_f^{(-)}(\boldsymbol{r}_1, \boldsymbol{r}_2; \boldsymbol{p}_e) = \frac{1}{\sqrt{2}} \left(\psi^C(\boldsymbol{r}_1; \boldsymbol{p}_e)\, \psi_0^{\mathrm{He}^+}(\boldsymbol{r}_2) + \psi^C(\boldsymbol{r}_2; \boldsymbol{p}_e)\, \psi_0^{\mathrm{He}^+}(\boldsymbol{r}_1) \right) \tag{91}$$

the following orthogonalization condition is used:

$$\Psi_f^{(-)}(\boldsymbol{r}_1, \boldsymbol{r}_2; \boldsymbol{p}_e) = \tilde{\Psi}_f(\boldsymbol{r}_1, \boldsymbol{r}_2; \boldsymbol{p}_e) - \left\langle \tilde{\Psi}_f^{(-)}(\boldsymbol{r}_1, \boldsymbol{r}_2; \boldsymbol{p}_e) \middle| \Psi_i(\boldsymbol{r}_1, \boldsymbol{r}_2) \right\rangle \Psi_i(\boldsymbol{r}_1, \boldsymbol{r}_2). \tag{92}$$

In **Approach II**, the non-correlated RHF helium ground state wave function [121] is used; thus, only the "kicked" electron can escape, while the other electron stays frozen at the core. To model the influence of the remaining electron on the escaping electron, a single-active-electron effective potential [139] is employed. This potential has an asymptotic charge of $Z = 2$ for $r \to 0$, which is screened by the second electron such that asymptotically for large r, it reaches $Z = 1$. The one-electron ground state function $\psi_i(\boldsymbol{r})$ and the one-electron continuum state wave function $\psi_f^{(-)}(\boldsymbol{r}; \boldsymbol{p}_e)$ with incoming boundary conditions are calculated numerically via solving the radial Schrödinger equation. Hence, the electronic matrix element in Eq. (90) is approximated as

$$M_e(\boldsymbol{Q}, \boldsymbol{p}_e) = \sqrt{2} \left\langle \psi_f^{(-)}(\boldsymbol{r}; \boldsymbol{p}_e) \middle| e^{\imath \boldsymbol{Q} \cdot \boldsymbol{r}} \middle| \psi_i(\boldsymbol{r}) \right\rangle. \tag{93}$$

This expression is calculated using a plane wave expansion of $e^{\imath \boldsymbol{Q} \cdot \boldsymbol{r}}$ and an expansion of the scattering states $\psi_f^{(-)}(\boldsymbol{r}; \boldsymbol{p}_e)$ in terms of spherical harmonics.

Within the A^2 approximation, the magnitude of the energy transfer is determined by energy conservation. It is worth mentioning that, under the present conditions, the photon loses only a few percent of its primary energy. Thus, the momentum transfer is largely a consequence of the angular deflection of the photon and not a consequence of its change in energy. This can be seen by inspecting the energy distribution of the ejected electron in Figure 10, *a*. The electron energy distribution peaks at zero and falls off exponentially. For electron forward

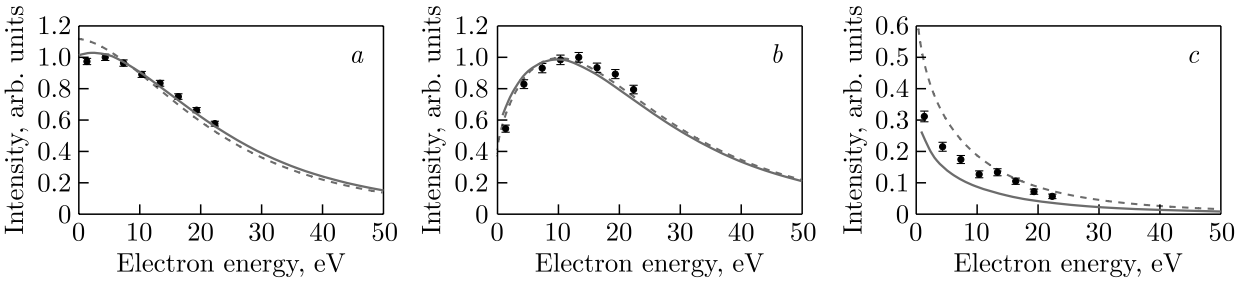

Figure 10. Electron energy distribution. The scattering angle for the outgoing photon is restricted to $140° < \theta < 180°$ in all panels. *a*) The electron energy spectrum is shown independent of the electron emission direction. *b*) The electron emission angle is restricted to forward scattering ($0° < \theta_e < 40°$). *c*) The electron emission angle is restricted to backward scattering ($140° < \theta_e < 180°$). The black dots are the experimental data. The error bars are the standard statistical error. The solid lines represent the theoretical results of **Approach I**, and the dashed lines represent the results of **Approach II**. The experimental data in panels (*a*) and (*b*) are normalized such that the maximum intensity is 1; the theory is normalized such that the integrals of the experimental data and the theoretical curves are equal. The normalization factors in panel (*c*) are identical to the ones in panel (*b*), since here the forward/backward direction of the same distribution is depicted.

emission (Figure 10, *b*), it peaks at 11 eV for photon back-scattering, while the backward-emitted electrons for the same conditions are much lower in energy (Figure 10, *c*). This also manifests itself in the FDCS showing the electron angular distribution for a fixed electron energy and a fixed photon scattering angle of $150° \pm 20°$.

4.1.4. Summary to Section 4.1

The influence of Kato's cusp conditions on the DCSs of the ionization processes of helium by fast electron and proton impact, determined by different types of variational helium ground state wave functions, is studied. It is observed that all wave functions that provide a good accuracy of the energy give very similar results, while wave functions that provide a poor accuracy of the energy give different results. It follows that for DCS calculations it is important to use correlated variational wave functions, which give a good accuracy of the ground state energy, regardless of whether they satisfy Kato's cusp conditions or not. Based on this, an optimized helium ground state wave function on the exponential basis (69) containing only 20 terms, taking into account the two-electron symmetry, and providing an accuracy of the ground state energy to 10^{-7} is constructed and applied. Using this wave function, several important physical results are obtained for the single and double ionization processes of helium by fast electron and proton impact.

Section 4.1.2 presents theoretical calculations of experimental work with high momentum resolution on the single ionization of helium induced by 1 MeV protons. The overall agreement is strikingly good, and even the FBA yields good agreement between theory and experiment. This has been expected for several decades, but so far has not been accomplished. The influence of projectile coherence effects on the measured data is briefly discussed in terms of an ongoing dispute on the existence of nodal structures in electron angular emission distributions.

Section 4.1.3 illustrates the theoretical calculations of the FDCSs for Compton scattering at a gas-phase atom, unveiling the mechanism of nearthreshold Compton scattering. Our theoretical results show good agreement with experimental work. The coincidence detection of ions and electrons, as demonstrated here, paves the road to exploit Compton scattering for imaging molecular wave functions not only averaged over the molecular axis, but also in the body-fixed frame of the molecule.

4.2. Spectrum of the beryllium dimer in the ground $X^1\Sigma_g^+$ state

Over the last decade, theoretical studies [140–145] have shown twelve vibrational bound states in the beryllium dimer, whereas eleven states were extracted from the experimental data of laser pump-probe spectroscopy. Traditionally, potential energy curves (PECs) are numerically tabulated on a non-uniform grid and continued at large interatomic distances using additional information about the interaction of atoms comprising the diatomic molecule. The dominant term of the PEC at large distances is given by the van der Waals interaction, inversely proportional to the sixth power of the independent variable with the constant, determined from theory [146, 147]. The problems of matching the asymptotic expansion of the PEC with its tabulated numerical values and correctly calculating the required sets of bound and metastable states are studied in [36].

4.2.1. Mathematical statement of the problem

To describe the beryllium dimer in the adiabatic approximation (in which the diagonal nonadiabatic correction is not taken into account), commonly referred to as the Born–Oppenheimer (BO) approximation, in [36, 148], the Schrödinger equation is used in the form

$$\left(-s_2\frac{1}{r^2}\frac{d}{dr}r^2\frac{d}{dr}+s_2\frac{J(J+1)}{r^2}+V(r)-E\right)\Phi_J(r)=0. \tag{94}$$

Here J is the total angular momentum quantum number, r is expressed in Å, and $s_2 = 3.741151852$ cm^{-1}. E is the energy in cm^{-1} and $V(r)$ is the PEC in cm^{-1}.

In [36], the potential $V(r)$ (in cm^{-1}) is given by the modified expanded Morse oscillator (MEMO) potential function, which is an approximation of MEMO tabular values. It should be noted that the tabular values give a smooth approximation up to $r = 12$, where the approximate PEC matches with the asymptotic potential $V_{\rm as}^{\rm BO}(r) = s_2U_{\rm as}^{\rm BO}(r)$ given analytically by the expansions [146]

$$U_{\rm as}^{\rm BO}(r)=s_1\tilde{V}_{\rm as}^{\rm BO}(r),\quad \tilde{V}_{\rm as}^{\rm BO}(r)=-\left(\frac{214}{Z^6}+\frac{10230}{Z^8}+\frac{504300}{Z^{10}}\right), \tag{95}$$

where $s_1 = {\rm aue}/s_2 = 58664.99239$, $Z = r/s_3$ and $s_3 = 0.52917$ is the Bohr radius in Å. This fact allows considering the interval $r \in [r_{\rm match} \geqslant 12, \infty)$ as possible for using the asymptotic potential $V_{\rm as}^{\rm BO}(r)$ at large r and executing conventional calculations based on the tabular values of $V(r)$ in the finite interval $r \in [r_1 = 1.5, r = 12]$ (see also [145]).

In [145], the potential $V(r)$ (in cm^{-1}) is given by the BO potential function plus the relativistic potential function, marked as STO, with tabular values. In the interval $r \in [r_{\rm match} = 14.552, \infty)$, the potential $V_{\rm as}(r) = s_2U_{\rm as}(r)$ is approximated by the asymptotic expansion

$$\begin{aligned} &U_{\rm as}(r)=s_1\tilde{V}_{\rm as}(r),\quad \tilde{V}_{\rm as}(r)=\tilde{V}_{\rm as}^{\rm BO}(r)+\tilde{V}_{\rm as}^{\rm rel}(r),\\ &\tilde{V}_{\rm as}^{\rm rel}(r)=-\left(\frac{1.839\cdot10^{-4}}{Z^4}+\frac{0.11944}{Z^6}+\frac{19.582}{Z^8}-\frac{1323.5}{Z^{10}}\right), \end{aligned} \tag{96}$$

where $\tilde{V}_{\rm as}^{\rm BO}(r)$ and $\tilde{V}_{\rm as}^{\rm rel}(r)$ are given by (95) and [145], respectively.

4.2.2. Numerical results

The vibrational-rotational spectrum of the real-valued eigenenergies $E_{\nu J}$ and the corresponding eigenfunctions $\Phi_{\nu J}(r)$ of the bound states of the BVP for Eq. (94) are calculated using the FEM KANTBP 4M [71] and KANTBP 3.0 [150] programs on the finite interval $[r_{\min} = 1.9, r_{\max} = 40]$, with the Neumann boundary conditions on the boundary points

$$\frac{d}{dr}\Phi_{\nu J}(r) = 0, \quad r = r_{\min}, \quad r = r_{\max}. \tag{97}$$

The potential functions MEMO and STO $V(r)$ from $J = 0$ to $J = 36$ support 252 and 253 vibrational-rotational energy levels $E_{\nu J}$, respectively. The calculated $\nu = 1 - 10$ vibrational spectra $E_{\nu J=0} - E_{\nu=0 J=0}$ (in cm^{-1}) are in good agreement with the energies known from the literature [140, 142–144] and experimental results [149] (see Table 4). It should be pointed out that there is no energy level $E_{\nu=8,J=14}$ for the MEMO PEC while $E_{\nu=8,J=14} = -1.4$ (in cm^{-1}) for the STO PEC. Figure 11, *a* (black dots) also shows the vibrational-rotational spectrum $E_{\nu J}$ (in cm^{-1}) of the beryllium dimer vs J for the MEMO PEC.

The rotational-vibrational spectrum of the complex-valued eigenenergies $E^M_{J\nu}$ and the corresponding eigenfunctions $\Phi^M_{J\nu}(r)$ of the bound states of the BVP for Eq. (94) is solved using the FEM KANTBP 4M [71] and KANTBP 5M [72] programs on the finite interval $[r_{\min} = 1.9, r_{\max} = 20]$, with the Neumann boundary condition (97) at the left boundary point $r = r_{\min} = 1.90$ and the Robin boundary condition at the right boundary point $r = r_{\max} = 20$ with a logarithmic derivative for $\Phi_J(kr) \equiv \Phi^M_{J\nu}(kr)$

$$\frac{d\Phi_J(kr)}{dr} - \mathcal{R}\Phi_J(kr) = 0, \quad \mathcal{R} = \frac{1}{\Phi^+_{as}(kr)}\frac{d\Phi^+_{as}(kr)}{dr}, \tag{98}$$

Table 4. Comparison of the vibrational spectra $E_{\nu J=0} - E_{\nu=0 J=0}$ (in cm^{-1}) for the $X^1\Sigma^+_g$ state of the beryllium dimer: eigenenergies $E_{\nu J=0}$ of vibrational-rotational bound states (in cm^{-1}) calculated by means of the STO and MEMO PECs and experimental (Exp) results [149]. Here D_e is the well depth and $D_0 = -E_{\nu=0 J=0}$ is the dissociation energy in cm^{-1}, r_e is the equilibrium internuclear distance in Å, rms is the root-mean-square discrepancy between the theoretical and experimental data.

ν	STO	MEMO	Exp
r_e	2.447	2.4534	2.4536
D_e	934.4	929.804	929.7 ± 2
D_0	807.7	806.07	807.4
1	223.5	222.50	222.6
2	398.2	397.34	397.1
3	519.3	517.71	518.1
4	595.7	594.89	594.8
5	652.2	651.91	651.5
6	699.3	698.92	698.8
7	738.1	737.72	737.7
8	768.6	768.27	768.2
9	790.1	789.74	789.9
10	802.6	801.66	802.6
11	807.2	805.74	
rms	0.7	0.4	

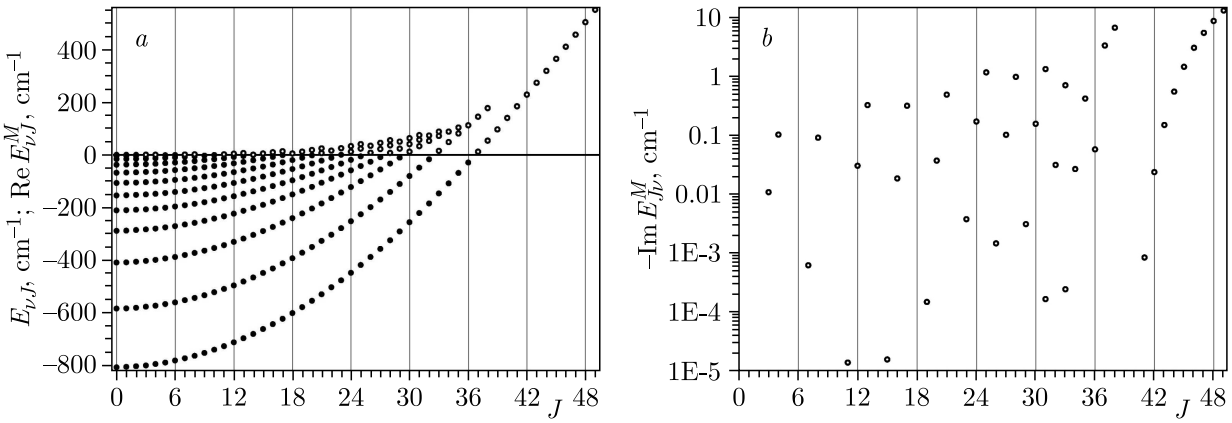

Figure 11. *a*) Eigenenergies $E_{\nu J}$ of vibrational-rotational bound states (black dots), the real part Re $E^M_{J\nu}$ (empty circles) and *b*) minus the imaginary part $-$Im $E^M_{J\nu}$ of the complex eigenenergies $E^M_{J\nu}$ of rotational-vibrational metastable states in cm^{-1}

which follows from the asymptotic solution only for the outgoing wave [32, 151, 152]

$$\Phi^+_{as}(kr) = \sqrt{k} h^{(1)}_J(kr) = -\imath \frac{\exp\left(+\imath(kr - \pi J/2)\right)}{\sqrt{kr}} + O(k^{-3/2} r^{-2}). \tag{99}$$

Here complex-valued $k \equiv k^M_{J\nu} = \sqrt{E^M_{J\nu}/s_2}$ in units of Å^{-1} is the wave number, $E^M_{J\nu} = s_2 \mathcal{E}^M_{J\nu}$ cm^{-1}, $h^{(1)}_J(z)$ is the spherical Hankel function of the first kind [153].

The metastable state problem is reduced by FEM to the algebraic generalized eigenvalue problem (33), where the elements of the matrix $\mathbf{A}(\lambda)$ follow boundary conditions (98) and depend on the spectral parameter λ. Then, Eq. (33) is solved by the CANM algorithm with the optimal choice of the iteration parameter described in section 2.4.2, which is implemented in the KANTBP 4M [71] and KANTBP 5M [72] programs.

The potential functions MEMO and STO $V(r)$ at $J = 3, 4, 7, 8, 9, 11, \ldots, 49$ support 62 rotational-vibrational metastable energy levels $E^M_{J\nu}$ [148]. The rotational-vibrational metastable spectrum $E^M_{J\nu}$ (in cm^{-1}) vs J for the MEMO PEC is shown in Figure 11, *a* (the real parts Re $E^M_{J\nu}$ are empty circles) and Figure 11, *b* (minus the imaginary parts Im $E^M_{J\nu}$).

4.2.3. Summary to Section 4.2

Calculations of the spectrum of the bound vibrational-rotational state were performed by a standard approach, while the spectrum of the metastable rotational-vibrational state having complex-valued eigenenergies was calculated by CANM. Therefore, this approach is important for modeling the near-surface diffusion of beryllium dimers in connection with the well-known multifunctional use of beryllium alloys in modern technologies of electronic space and nuclear industries [154], and, in particular, the ITER project [155, 156].

4.3. Iterative scheme for solving a continuous minimax optimization problem and its application

The Rayleigh–Ritz variational expansion method to eigenvalue problems for semi-bounded operators has found numerous applications in non-relativistic atomic and molecular structure calculations. For the Schrödinger Hamiltonian the method is based on the Hylleraas-Undheim theorem [120], which leads to the minimization problem of the Rayleigh quotient on the set of admissible trial functions.

Relativistic approaches oriented to the calculation of properties of heavy atoms (e.g. relativistic many-body perturbation theory, Dirac–Fock self consistent field method), which start with the Dirac Hamiltonian encounter difficulties directly related to the presence of the negative-energy continuum in the Dirac spectrum.

Since the Dirac operator is not bounded, the application of the variational technique to the relativistic Hamiltonian requires modification. One of them is the breakdown of the standard variational method using, for example, the kinetic balance approach [157]. In [158–160], various kinetic balanced variational basis functions, which do not give spurious solutions, are constructed. However, the disadvantage of these basis functions is the low convergence rate. Even the wave function of the exact solvable Dirac equation with a one-center Coulomb potential cannot be expressed analytically in terms of kinetic balanced variational basis functions.

In [161–164], the minimax formulation of the Dirac equation with a central potential, one- and two-center Coulomb potential is used. A condition for constructing a finite number of variational basis functions without using kinetic balance, which do not give spurious solutions, is established.

4.3.1. Mathematical statement of the continuous minimax optimization problem

The formulation of the continuous minimax problem is as follows [165]:

$$\min_{\boldsymbol{x}\in\mathcal{X}} \max_{\boldsymbol{y}\in\mathcal{Y}} f(\boldsymbol{x},\boldsymbol{y}), \tag{100}$$

where $f(\boldsymbol{x},\boldsymbol{y})$: $\mathcal{X}\times\mathcal{Y}\subset\mathbb{R}^N\times\mathbb{R}^M\to\mathbb{R}$ is a twice continuously differentiable function in the region of space $\mathcal{X}\times\mathcal{Y}\subset\mathbb{R}^N\times\mathbb{R}^M$.

When considering it, the following notation is used for the gradient $\mathbf{G}$ and the Hessian $\mathbf{H}$

$$\nabla f(\boldsymbol{x},\boldsymbol{y}) = \mathbf{G} = \begin{pmatrix} \mathbf{G}_{\boldsymbol{x}} \\ \mathbf{G}_{\boldsymbol{y}} \end{pmatrix}, \quad \nabla^2 f(\boldsymbol{x},\boldsymbol{y}) = \mathbf{H} = \begin{pmatrix} \mathbf{H}_{\boldsymbol{xx}} & \mathbf{H}_{\boldsymbol{xy}} \\ \mathbf{H}_{\boldsymbol{yx}} & \mathbf{H}_{\boldsymbol{yy}} \end{pmatrix}, \tag{101}$$

where $\mathbf{G}_{\boldsymbol{x}}$ and $\mathbf{G}_{\boldsymbol{y}}$ are the vectors of length N and M, $\mathbf{H}_{\boldsymbol{xx}}$, $\mathbf{H}_{\boldsymbol{xy}}$, $\mathbf{H}_{\boldsymbol{yx}}$, and $\mathbf{H}_{\boldsymbol{yy}}$ are the matrices of dimensions $N\times N$, $N\times M$, $M\times N$, and $M\times M$, and the matrix $\mathbf{H}$ is symmetric.

The necessary and sufficient conditions for the local Nash equilibrium and the local minimax of the twice continuously differentiable function $f(\boldsymbol{x},\boldsymbol{y})$ at the point $(\boldsymbol{x}^\star,\boldsymbol{y}^\star)$ are as follows:

Proposition 1 *(First-order necessary condition). Any local Nash equilibrium and minimax point* $(\boldsymbol{x}^\star,\boldsymbol{y}^\star)$ *satisfy*

$$\mathbf{G} = \mathbf{0}. \tag{102}$$

Proposition 2 *(Second-order necessary condition). Any stationary point* $(\boldsymbol{x}^\star,\boldsymbol{y}^\star)$ *satisfying the conditions*

$$\mathbf{H}_{\boldsymbol{xx}} \succ \mathbf{0}, \quad \mathbf{H}_{\boldsymbol{yy}} \prec \mathbf{0} \tag{103}$$

is a local Nash equilibrium.

Proposition 3 *(Second-order necessary condition). Any stationary point* $(\boldsymbol{x}^\star,\boldsymbol{y}^\star)$ *satisfying the conditions*

$$\mathbf{H}_{\boldsymbol{yy}} \prec \mathbf{0}, \tag{104}$$

$$\mathbf{H}_{\boldsymbol{xx}} - \mathbf{H}_{\boldsymbol{xy}}\mathbf{H}_{\boldsymbol{yy}}^{-1}\mathbf{H}_{\boldsymbol{yx}} \succ \mathbf{0} \tag{105}$$

is a local minimax point.

Here $\succ\mathbf{0}$ and $\prec\mathbf{0}$ denote the positive and negative definiteness of the matrix, respectively.

4.3.2. Numerical approach

Within the gradient descent method and its modifications, there are many algorithms used to find local Nash equilibrium points in a convex-concave domain. However, the disadvantage of this method is the low convergence rate and the impossibility of directly checking the conditions (103). There are also several package programs for the discrete minimax problem, for example, FSQP program [166], but there are no package programs for the continuous minimax problem. Therefore, we developed a new iterative scheme based on the Newton-type method for minimization [118] in combination with negative curvature direction methods for nonconvex-nonconcave, convex-nonconcave, and nonconvex-concave domains [118, 167].

Algorithm:

1. Set the initial approximation $\boldsymbol{z}^0 = (\boldsymbol{x}^0, \boldsymbol{y}^0)^T$, where "$T$" is the transpose of the vector; the required accuracy $\epsilon > 0$, $\epsilon_1 \gg \epsilon$; the maximum step h correction; $0 < \alpha < 1$; and $n = 0$.

2. If $\|\mathbf{G}\| \leqslant \epsilon$ and conditions (104), (105) are satisfied for $\boldsymbol{z}^n = (\boldsymbol{x}^n, \boldsymbol{y}^n)^T$, then the iterative process terminates.

3. Find a diagonal matrix $\mathbf{D}_{\boldsymbol{y}}$ that satisfies the condition

$$\bar{\mathbf{H}}_{\boldsymbol{yy}} = \mathbf{H}_{\boldsymbol{yy}} + \mathbf{D}_{\boldsymbol{y}} \prec \mathbf{0}, \tag{106}$$

and an additional vector $\boldsymbol{v}_{\boldsymbol{y}}$ to use the negative curvature direction method that satisfies the conditions

$$\mathbf{G}_{\boldsymbol{y}}^T \boldsymbol{v}_{\boldsymbol{y}} \geqslant 0, \quad \boldsymbol{v}_{\boldsymbol{y}}^T \mathbf{H}_{\boldsymbol{yy}} \boldsymbol{v}_{\boldsymbol{y}} > 0. \tag{107}$$

If condition (104) is satisfied, then $\mathbf{D}_{\boldsymbol{y}} = \mathbf{0}$ and $\boldsymbol{v}_{\boldsymbol{y}} = \mathbf{0}$.

3.1 If $\|\mathbf{G}\| \leqslant \epsilon_1$ and condition (104) is not satisfied (the so-called "nonconcave" case), then set

$$\delta \boldsymbol{z}^n = \tau \begin{pmatrix} \mathbf{0} \\ \boldsymbol{v}_{\boldsymbol{y}} \end{pmatrix}. \tag{108}$$

Here $\tau = h/\|\boldsymbol{v}_{\boldsymbol{y}}\|$. Next, the inequality

$$f(\boldsymbol{x}^n, \boldsymbol{y}^n) \leq f(\boldsymbol{x}^n, \tilde{\boldsymbol{y}}^{n+1}), \quad \tilde{\boldsymbol{y}}^{n+1} = \boldsymbol{y}^n + \tau \boldsymbol{v}_{\boldsymbol{y}}. \tag{109}$$

is checked. If it is not satisfied, then $\delta \boldsymbol{z}^n = \alpha \delta \boldsymbol{z}^n$ is set. This procedure is repeated until condition (109) is satisfied. If condition (109) is satisfied, then go to Step **7**.

4. Find an additional vector $\boldsymbol{v}_{\boldsymbol{x}}$ to use the negative curvature direction method that satisfies the conditions

$$\mathbf{G}_{\boldsymbol{x}}^T \boldsymbol{v}_{\boldsymbol{x}} \leqslant 0, \quad \boldsymbol{v}_{\boldsymbol{x}}^T \mathbf{H}_{\boldsymbol{xx}} \boldsymbol{v}_{\boldsymbol{x}} < 0. \tag{110}$$

If the condition $\mathbf{H}_{\boldsymbol{xx}} \succ \mathbf{0}$ is satisfied, then $\boldsymbol{v}_{\boldsymbol{x}} = \mathbf{0}$.

5. Find a diagonal matrix $\mathbf{D}_{\boldsymbol{x}}$ that satisfies the condition

$$\bar{\mathbf{H}}_{\boldsymbol{xx}} + \mathbf{D}_{\boldsymbol{x}} \succ \mathbf{0}, \tag{111}$$

where $\bar{\mathbf{H}}_{\boldsymbol{xx}} = \mathbf{H}_{\boldsymbol{xx}} - \mathbf{H}_{\boldsymbol{xy}} \bar{\mathbf{H}}_{\boldsymbol{yy}}^{-1} \mathbf{H}_{\boldsymbol{yx}}$. If condition $\bar{\mathbf{H}}_{\boldsymbol{xx}} \succ \mathbf{0}$ is satisfied, then $\mathbf{D}_{\boldsymbol{x}} = \mathbf{0}$.

5.1 If $\|\mathbf{G}\| \leqslant \epsilon_1$ and only condition (104) is satisfied (the so-called "nonconvex-concave" case), then set

$$\delta \boldsymbol{z}^n = \tau \begin{pmatrix} \boldsymbol{v}_{\boldsymbol{x}} \\ \mathbf{0} \end{pmatrix}, \tag{112}$$

where $\tau = h/\|\boldsymbol{v}_{\boldsymbol{x}}\|$. Next, the inequality

$$f(\tilde{\boldsymbol{x}}^{n+1}, \boldsymbol{y}^n) \le f(\boldsymbol{x}^n, \boldsymbol{y}^n), \quad \tilde{\boldsymbol{x}}^{n+1} = \boldsymbol{x}^n + \tau \boldsymbol{v}_{\boldsymbol{x}}. \tag{113}$$

is checked. If it is not satisfied, then $\delta\boldsymbol{z}^n = \alpha\delta\boldsymbol{z}^n$ is set. This procedure is repeated until condition (113) is satisfied. If condition (113) is satisfied, then go to Step **7**.

6. If $\|\mathbf{G}\| > \epsilon_1$ or conditions (104), (105) are satisfied (the so-called "convex-concave" case), then $\delta\boldsymbol{z}^n = (\delta\boldsymbol{x}^n, \delta\boldsymbol{y}^n)^T$ is calculated using the modified Newton method

$$\delta\boldsymbol{z}^n = -\begin{pmatrix} \mathbf{H}_{\boldsymbol{xx}} + \mathbf{D}_{\boldsymbol{x}} & \mathbf{H}_{\boldsymbol{xy}} \\ \mathbf{H}_{\boldsymbol{yx}} & \mathbf{H}_{\boldsymbol{yy}} + \mathbf{D}_{\boldsymbol{y}} \end{pmatrix}^{-1} \begin{pmatrix} \mathbf{G}_{\boldsymbol{x}} \\ \mathbf{G}_{\boldsymbol{y}} \end{pmatrix}, \tag{114}$$

Next, the inequality

$$\mathbf{G}_{\boldsymbol{x}}^T \delta\boldsymbol{x}^n \leqslant 0, \quad \mathbf{G}_{\boldsymbol{y}}^T \delta\boldsymbol{y}^n \geqslant 0. \tag{115}$$

is checked. If at least one of them is not satisfied, then we set $(\mathbf{D}_{\boldsymbol{x}})_{jj} = 2\max\left((\mathbf{D}_{\boldsymbol{x}})_{jj}, \epsilon_1\right)$, $(\mathbf{D}_{\boldsymbol{y}})_{jj} = 2\min\left((\mathbf{D}_{\boldsymbol{y}})_{jj}, -\epsilon_1\right)$, and recalculate $\delta\boldsymbol{z}^n$ from (114). This procedure is repeated until both conditions (115) are satisfied.

7. Set $\boldsymbol{z}^{n+1} = \boldsymbol{z}^n + \delta\boldsymbol{z}^n$ and $n = n + 1$. Go to Step **2**.

There are two main algorithms for computing the diagonal matrices $\mathbf{D}_{\boldsymbol{x}}$ and $\mathbf{D}_{\boldsymbol{y}}$.
In the first algorithm, we choose

$$\mathbf{D}_{\boldsymbol{x}} = -\lambda_{\boldsymbol{x}}\mathbf{I}_{\boldsymbol{x}}, \quad \mathbf{D}_{\boldsymbol{y}} = -\lambda_{\boldsymbol{y}}\mathbf{I}_{\boldsymbol{y}}, \tag{116}$$

where $\mathbf{I}_{\boldsymbol{x}}$ and $\mathbf{I}_{\boldsymbol{y}}$ are unit matrices; $\lambda_{\boldsymbol{x}}$ is a negative number less than the smallest negative eigenvalue of $\bar{\mathbf{H}}_{\boldsymbol{xx}} \not\succ \mathbf{0}$; and $\lambda_{\boldsymbol{y}}$ is a positive number greater than the largest positive eigenvalue of $\mathbf{H}_{\boldsymbol{yy}} \not\prec \mathbf{0}$.

In the second algorithm, the matrices $\mathbf{D}_{\boldsymbol{x}}$ and $\mathbf{D}_{\boldsymbol{y}}$ are calculated using the modified Cholesky factorization [118]

$$\bar{\mathbf{H}}_{\boldsymbol{xx}} + \mathbf{D}_{\boldsymbol{x}} = \tilde{\mathbf{L}}\tilde{\mathbf{D}}\tilde{\mathbf{L}}^T, \tag{117}$$

$$\mathbf{H}_{\boldsymbol{yy}} + \mathbf{D}_{\boldsymbol{y}} = \hat{\mathbf{L}}\hat{\mathbf{D}}\hat{\mathbf{L}}^T, \tag{118}$$

where $\tilde{\mathbf{L}}$ and $\hat{\mathbf{L}}$ are lower triangular matrices, $\tilde{\mathbf{D}}$ and $\hat{\mathbf{D}}$ are diagonal matrices, all elements of which must be negative and positive, respectively.

The second algorithm is more efficient since the matrices $\mathbf{D}_{\boldsymbol{x}}$ and $\mathbf{D}_{\boldsymbol{y}}$ are more sensitive to the matrices $\bar{\mathbf{H}}_{\boldsymbol{xx}}$ and $\mathbf{H}_{\boldsymbol{yy}}$, respectively.

4.3.3. Negative curvature direction method

One of the key steps in finding a local minimax point is to leave the domain of the spurious minimax point for $\|\mathbf{G}\| < \epsilon_1$. In this case, Newton's method and any of its modifications are ineffective. The negative curvature direction method is one of the most effective.

There are also two main algorithms for computing the additional vectors $\boldsymbol{v}_{\boldsymbol{x}}$ and $\boldsymbol{v}_{\boldsymbol{y}}$.

In the first algorithm [167], the vector $\boldsymbol{v}_{\boldsymbol{x}}$ is chosen as the eigenvector corresponding to the minimum negative eigenvalue $\lambda_{\min}$ of the matrix $\mathbf{H}_{\boldsymbol{xx}}$. Then from (113)

$$\begin{aligned} f(\tilde{\boldsymbol{x}}^{n+1}, \boldsymbol{y}^n) - f(\boldsymbol{x}^n, \boldsymbol{y}^n) &= \mathbf{G}_{\boldsymbol{x}}^T \delta\boldsymbol{x}^n + \frac{(\delta\boldsymbol{x}^n)^T \mathbf{H}_{\boldsymbol{xx}} \delta\boldsymbol{x}^n}{2} + O\left(\|\delta\boldsymbol{x}^n\|^3\right) = \\ &= \alpha\tau \mathbf{G}_{\boldsymbol{x}}^T \boldsymbol{v}_{\boldsymbol{x}} + \alpha^2\tau^2 \frac{\boldsymbol{v}_{\boldsymbol{x}}^T \mathbf{H}_{\boldsymbol{xx}} \boldsymbol{v}_{\boldsymbol{x}}}{2} + O\left(\|\delta\boldsymbol{x}^n\|^3\right) = \\ &= \alpha\tau \mathbf{G}_{\boldsymbol{x}}^T \boldsymbol{v}_{\boldsymbol{x}} + \frac{\lambda_{\min}\alpha^2\tau^2}{2} + O\left(\|\delta\boldsymbol{x}^n\|^3\right). \end{aligned} \tag{119}$$

Taking into account (110), we obtain

$$f(\tilde{\boldsymbol{x}}^{n+1}, \boldsymbol{y}^n) - f(\boldsymbol{x}^n, \boldsymbol{y}^n) < 0 \tag{120}$$

at $\alpha = \alpha^* < 1$. Similarly, $\boldsymbol{v_y}$ is chosen as the eigenvector corresponding to the maximum positive eigenvalue $\lambda_{\max}$ of the matrix $\mathbf{H_{yy}}$, after which we find the parameter $\alpha = \alpha^* < 1$ subject to the condition

$$f(\boldsymbol{x}^n, \tilde{\boldsymbol{y}}^{n+1}) - f(\boldsymbol{x}^n, \boldsymbol{y}^n) > 0. \tag{121}$$

In the second algorithm, the vectors $\boldsymbol{v_x}$ and $\boldsymbol{v_y}$ are chosen as solutions to the systems

$$\tilde{\mathbf{L}}^T \boldsymbol{v_x} = \boldsymbol{e}_{s_x}, \quad \hat{\mathbf{L}}^T \boldsymbol{v_y} = \boldsymbol{e}_{s_y}. \tag{122}$$

Here $\boldsymbol{e}_{s_x}$, $\boldsymbol{e}_{s_y}$ are vectors which have all elements are equal to zero, except $e_{s_x} = e_{s_y} = 1$ and s_x, s_y are integers such that

$$\begin{aligned} &\phi_{s_x} \leqslant \phi_j, \quad \phi_j = (\mathbf{H_{xx}})_{jj} - \sum_{r=1}^{j-1} \tilde{l}_{jr}^2 \tilde{d}_r, \quad j = 1, 2, \ldots, N, \\ &\phi_{s_y} \geqslant \phi_j, \quad \phi_j = (\mathbf{H_{yy}})_{jj} - \sum_{r=1}^{j-1} \hat{l}_{jr}^2 \hat{d}_r, \quad j = 1, 2, \ldots, M. \end{aligned} \tag{123}$$

The matrices $\tilde{\mathbf{L}}$ and $\tilde{\mathbf{D}}$ are calculated by formula (117), where the matrix $\bar{\mathbf{H}}_{\boldsymbol{xx}}$ is replaced by $\mathbf{H_{xx}}$, and the matrices $\hat{\mathbf{L}}$ and $\hat{\mathbf{D}}$ are preserved by formula (118). In [118], it is proved that the vector $\boldsymbol{v_x}$ and consequently the vector $\boldsymbol{v_y}$ define the negative curvature direction.

4.3.4. Mathematical statement of the one-electron two-center Coulomb Dirac equation

The one-electron wave function $\Psi(\boldsymbol{r})$ is a solution of the stationary Dirac equation

$$H_D \Psi(\boldsymbol{r}) = E \Psi(\boldsymbol{r}), \tag{124}$$

where $E = E_R$ is the relativistic energy, and H_D is the two-center Dirac Hamiltonian:

$$H_D = c\, \boldsymbol{\alpha} \cdot \boldsymbol{p} + m_e c^2 \boldsymbol{\beta} + U(\boldsymbol{r}) \mathbf{I}. \tag{125}$$

Here c is the speed of light, m_e is the mass of the electron, and $\boldsymbol{p}$ is the momentum operator:

$$\boldsymbol{p} = \left(-\imath\hbar \frac{\partial}{\partial x}, -\imath\hbar \frac{\partial}{\partial y}, -\imath\hbar \frac{\partial}{\partial z} \right), \tag{126}$$

$\boldsymbol{\alpha}$, $\boldsymbol{\beta}$ are the well-known 4×4 Dirac matrices:

$$\boldsymbol{\alpha} = \begin{pmatrix} \mathbf{0} & \boldsymbol{\sigma} \\ \boldsymbol{\sigma} & \mathbf{0} \end{pmatrix}, \quad \boldsymbol{\beta} = \begin{pmatrix} \boldsymbol{I} & \mathbf{0} \\ \mathbf{0} & -\boldsymbol{I} \end{pmatrix}, \tag{127}$$

$\boldsymbol{\sigma} = (\boldsymbol{\sigma}_x, \boldsymbol{\sigma}_y, \boldsymbol{\sigma}_z)$ are the Pauli matrices:

$$\boldsymbol{\sigma}_x = \begin{pmatrix} 0 & 1 \\ 1 & 0 \end{pmatrix}, \quad \boldsymbol{\sigma}_y = \begin{pmatrix} 0 & -\imath \\ \imath & 0 \end{pmatrix}, \quad \boldsymbol{\sigma}_z = \begin{pmatrix} 1 & 0 \\ 0 & -1 \end{pmatrix}, \tag{128}$$

$\mathbf{I}$ and $\boldsymbol{I}$ are the 4×4 and 2×2 unit matrices:

$$\mathbf{I} = \begin{pmatrix} \boldsymbol{I} & \mathbf{0} \\ \mathbf{0} & \boldsymbol{I} \end{pmatrix}, \quad \boldsymbol{I} = \begin{pmatrix} 1 & 0 \\ 0 & 1 \end{pmatrix}. \tag{129}$$

The two-center attractive Coulomb potential $U(\boldsymbol{r})$ is defined by

$$U(\boldsymbol{r}) = V(\boldsymbol{r}_1) + V(\boldsymbol{r}_2), \quad V(\boldsymbol{r}) = -\frac{Z}{r},$$

where Z is the point charge of the centers 1 and 2, $\boldsymbol{r}_1 = \boldsymbol{r} + \boldsymbol{\rho}/2$, $\boldsymbol{r}_2 = \boldsymbol{r} - \boldsymbol{\rho}/2$, $\boldsymbol{\rho} = (0, 0, \rho)$, and ρ is the internuclear distance.

Below, atomic units $e = m_e = \hbar = 1$ are used.

The Slater-type spinor orbitals centered on the nuclei are given as in [168] by

$$\psi_{njlm}(\boldsymbol{r}) \equiv \psi_{n\kappa m}(\boldsymbol{r}) = \begin{cases} \imath P_{n\kappa}(r)\Omega_{+\kappa m}(\theta,\varphi), \\ Q_{n\kappa}(r)\Omega_{-\kappa m}(\theta,\varphi). \end{cases} \tag{130}$$

Here $j = |\kappa| - 1/2$ and $\Omega_{jlm}(\theta,\varphi) \equiv \Omega_{\kappa m}(\theta,\varphi)$ are the spinor spherical harmonics [168]:

$$\Omega_{\kappa m}(\theta,\varphi) = \begin{cases} \begin{cases} +\sqrt{\dfrac{l+m+1/2}{2l+1}}Y_{lm-1/2}(\theta,\varphi), \\ +\sqrt{\dfrac{l-m+1/2}{2l+1}}Y_{lm+1/2}(\theta,\varphi), \end{cases} & \kappa < 0, \quad l = -\kappa - 1, \\ \begin{cases} -\sqrt{\dfrac{l-m+1/2}{2l+1}}Y_{lm-1/2}(\theta,\varphi), \\ +\sqrt{\dfrac{l+m+1/2}{2l+1}}Y_{lm+1/2}(\theta,\varphi), \end{cases} & \kappa > 0, \quad l = \kappa, \end{cases} \tag{131}$$

where $Y_{lm\pm1/2}(\theta,\varphi)$ are the spherical harmonics.

When the potential $U(\boldsymbol{r}) \equiv V(r)$ is spherically symmetrical, the large $P_{n\kappa}(r)$ and small $Q_{n\kappa}(r)$ radial components satisfy the following coupled equations

$$\begin{cases} +c\left(\dfrac{d}{dr} + \dfrac{1-\kappa}{r}\right) Q_{n\kappa}(r) + \left(V(r) + c^2 - E_{n\kappa}\right) P_{n\kappa}(r) = 0, \\ -c\left(\dfrac{d}{dr} + \dfrac{1+\kappa}{r}\right) P_{n\kappa}(r) + \left(V(r) - c^2 - E_{n\kappa}\right) Q_{n\kappa}(r) = 0. \end{cases} \tag{132}$$

The peculiarity of our approach is that, for the two-center problem considered, the one center basis large $P_{n\kappa}(r)$ and small $Q_{n\kappa}(r)$ radial components located on each center are chosen in the form

$$P_{n\kappa}(r) = (-1)^l \sum_{n_p=1}^{n_{p\kappa}^{\max}} c_{n_p\kappa} p_{n_p\kappa}(r), \quad Q_{n\kappa}(r) = (-1)^l \sum_{n_q=1}^{n_{q\kappa}^{\max}} d_{n_q\kappa} q_{n_q\kappa}(r). \tag{133}$$

Here $(-1)^l$ insures the inversion symmetry for the Dirac wave function. $p_{n_p\kappa}(r)$ and $q_{n_q\kappa}(r)$ are the normalized Slater-type orbitals with non-integer principal quantum numbers (NISTOs):

$$\begin{aligned} p_{n_p\kappa}(r) &= \frac{(2\lambda_\kappa)^{\gamma_\kappa+n_p-1/2}}{\sqrt{\Gamma(2\gamma_\kappa+2n_p-1)}} r^{\gamma_\kappa+n_p-2}\exp\left(-\lambda_\kappa r\right), \\ q_{n_q\kappa}(r) &= \frac{(2\mu_\kappa)^{\gamma_\kappa+n_q-1/2}}{\sqrt{\Gamma(2\gamma_\kappa+2n_q-1)}} r^{\gamma_\kappa+n_q-2}\exp\left(-\mu_\kappa r\right), \end{aligned} \tag{134}$$

Table 5. Total numbers N_{total} of NISTOs depending on the maximal principal quantum number $N_{\max}$.

κ	States	$N_{\max}=2$		$N_{\max}=3$		$N_{\max}=4$		$N_{\max}=5$	
		$n_{p\kappa}^{\max}$	$n_{q\kappa}^{\max}$	$n_{p\kappa}^{\max}$	$n_{q\kappa}^{\max}$	$n_{p\kappa}^{\max}$	$n_{q\kappa}^{\max}$	$n_{p\kappa}^{\max}$	$n_{q\kappa}^{\max}$
-1	$s_{1/2}$	2	2	3	3	4	4	5	5
1	$p_{1/2}$	2	3	3	4	4	5	5	6
-2	$p_{3/2}$	1	1	2	2	3	3	4	4
2	$d_{3/2}$			2	3	3	4	4	5
-3	$d_{5/2}$			1	1	2	2	3	3
3	$f_{5/2}$					2	3	3	4
-4	$f_{7/2}$					1	1	2	2
4	$g_{7/2}$							2	3
-5	$g_{9/2}$							1	1
N_{total}		11		24		41		62	

where λ_κ and μ_κ are positive variational parameters. These functions satisfy the following uncoupled system of equations

$$\begin{cases} \left(\dfrac{d}{dr}+\dfrac{1+\kappa}{r}\right) p_{n_p\kappa}(r) = \left(-\lambda_\kappa + \dfrac{\gamma_\kappa + n_p + \kappa - 1}{r}\right) p_{n_p\kappa}(r), \\ \left(\dfrac{d}{dr}+\dfrac{1-\kappa}{r}\right) q_{n_q\kappa}(r) = \left(-\mu_\kappa + \dfrac{\gamma_\kappa + n_q - \kappa - 1}{r}\right) q_{n_q\kappa}(r). \end{cases} \tag{135}$$

The non-integer parameter γ_κ is chosen from the asymptotic behavior of the large $P_{n\kappa}(r)$ and small $Q_{n\kappa}(r)$ components near the corresponding center

$$\gamma_\kappa = \gamma_{-\kappa} = \sqrt{\kappa^2 - \frac{Z^2}{c^2}}. \tag{136}$$

The total Slater-type spinor function centered on the nucleus has the following compact form [169]

$$\psi_{N_{\max}}(\boldsymbol{r}) = \begin{cases} \imath \displaystyle\sum_{n=1}^{N_{\max}} \sum_{\kappa=-n,\,\kappa\neq 0}^{n-1} P_{n\kappa}(r)\Omega_{+\kappa m}(\theta,\varphi), \\ \displaystyle\sum_{n=1}^{N_{\max}} \sum_{\kappa=-n,\,\kappa\neq 0}^{n-1} Q_{n\kappa}(r)\Omega_{-\kappa m}(\theta,\varphi), \end{cases} \tag{137}$$

where $N_{\max}$ is the maximal principal quantum number. To avoid spurious solutions the highest $n_{p\kappa}^{\max}$, $n_{q\kappa}^{\max}$ powers of r of Eq. (133) are chosen as [162]

$$n_{p\kappa}^{\max} = n - |\kappa| + 1, \quad n_{q\kappa}^{\max} = \begin{cases} n_{p\kappa}^{\max}, & \kappa < 0, \\ n_{p\kappa}^{\max} + 1, & \kappa > 0. \end{cases} \tag{138}$$

The total numbers N_{total} of NISTOs depending on $N_{\max} = 2-5$ are presented in Table 5. It can be seen that the number of each of the nonlinear parameters λ_κ and μ_κ is equal to $2N_{\max}-1$, i.e., the total number of nonlinear parameters is equal to $4N_{\max}-2$.

The one-electron ground state wave function $\Psi(\boldsymbol{r})$ for Eq. (124) has the form

$$\Psi(\boldsymbol{r}) = \psi_{N_{\max}}(\boldsymbol{r}_1) + \psi_{N_{\max}}(\boldsymbol{r}_2). \tag{139}$$

Finally, the minimax formulation [161] of the Dirac equation (124) is

$$-c^2 \leqslant E_R = \min_{P_{n\kappa}(r)\neq 0} \max_{Q_{n\kappa}(r)} \frac{\langle \Psi(\boldsymbol{r})|H_D|\Psi(\boldsymbol{r})\rangle}{\langle \Psi(\boldsymbol{r})|\Psi(\boldsymbol{r})\rangle} = \min_{\boldsymbol{\lambda}_\kappa} \max_{\boldsymbol{\mu}_\kappa} \frac{\langle \Psi(\boldsymbol{r})|H_D|\Psi(\boldsymbol{r})\rangle}{\langle \Psi(\boldsymbol{r})|\Psi(\boldsymbol{r})\rangle} \leqslant c^2. \tag{140}$$

Making the Rayleigh quotient (140) stationary with respect to the variations in $c_{n_p\kappa}$ and $d_{n_q\kappa}$, leads to the generalized eigenvalue problem

$$\mathbf{A}\begin{pmatrix} \boldsymbol{c} \\ \boldsymbol{d} \end{pmatrix} = E_R \mathbf{B}\begin{pmatrix} \boldsymbol{c} \\ \boldsymbol{d} \end{pmatrix}. \tag{141}$$

The matrix elements $\mathbf{A}$ and $\mathbf{B}$ of dimension $N_{\text{total}} \times N_{\text{total}}$ matrices are expressed by three-dimensional integrals and are reduced to one-dimensional integrals by means of the Fourier transform. It is noteworthy that the ground state energy of the Dirac equation (124) corresponds to the $(m+1)$-th smallest eigenvalue of Eq. (141). Here

$$m = \sum_{n=1}^{N_{\max}} \sum_{\kappa=-n,\,\kappa\neq 0}^{n-1} n_{q\kappa}^{\max} \tag{142}$$

is the total number of the basis functions of the small radial component in (137) (see Table 5), i.e., the dimension of the vector $\boldsymbol{d}$. Therefore, problem (141) is solved using the generalized Jacobi method for diagonalization.

4.3.5. Numerical results

In all our calculations, the speed of light c is 137.0359895 [164]. First of all, the relativistic energy E_R of the $1\sigma_g$ state of the lightest ion H_2^+ is determined. Since the binding energy $E_e = E_R - c^2$ and the non-relativistic energy are close for light ions, the initial estimates of the nonlinear parameters λ_κ, μ_κ (134) for all κ are chosen

$$\lambda_\kappa = \mu_\kappa = c^{-1}\sqrt{c^4 - E_R^2} \equiv c^{-1}\sqrt{-E_e(2c^2 + E_e)} \approx \sqrt{-2E_e}. \tag{143}$$

Then the relativistic $1\sigma_g$ state energy E_R of other ions is calculated step-by-step, using calculated λ_κ, μ_κ for the previous ion with charge Z_{old} multiplied by the factor Z/Z_{old} as the initial estimates of the new nonlinear parameters for ion with charge Z.

Table 6 presents the calculated relativistic $1\sigma_g$ state energy E_e for different ions at the "chemical" internuclear distance $\rho = 2/Z$ versus the number $N_{\max}$ and compared to the results given in [170]. For the cases $N_{\max} = 2$ and $N_{\max} = 3$, the same relativistic energies with a charge step of 1 and with the difference of charges, presented in the Table, are obtained. For the cases $N_{\max} = 4$ and $N_{\max} = 5$, there are many minimax solutions; therefore, the relativistic energies with a charge step of 1 are first calculated, then they are recalculated with different corrections of the nonlinear parameters λ_κ and μ_κ.

From the results presented in Table 6, it is evident that our calculated energies give the upper bounds of the exact energies with monotonic convergence with increasing $N_{\max}$. For $N_{\max} = 5$ our results are comparable to those in [170] (used almost 600 Gaussian-type basis functions) with a relative error of 10^{-7}–10^{-8}.

Table 6. Relativistic $1\sigma_g$ state energy $E_e = E_R - c^2$ at the "chemical" internuclear distance $\rho = 2/Z$.

Z	Ion	$N_{\max}$	Energy	Energy [170]
1	H_2^+	2	−1.102 248 990	
		3	−1.102 624 606	
		4	−1.102 640 853	
		5	−1.102 641 574	−1.102 641 581
2	He_2^{3+}	2	−4.409 083 664	
		3	−4.410 586 724	
		4	−4.410 651 814	
		5	−4.410 654 700	−4.410 654 728
10	Ne_2^{19+}	2	−110.297 363 139	
		3	−110.335 418 709	
		4	−110.337 130 064	
		5	−110.337 203 677	−110.337 204 410
20	Ca_2^{39+}	2	−442.073 489 140	
		3	−442.231 839 925	
		4	−442.239 683 071	
		5	−442.239 984 905	−442.239 997 265
30	Zn_2^{59+}	2	−998.024 713 682	
		3	−998.404 961 752	
		4	−998.426 014 019	
		5	−998.426 773 718	−998.426 763 032
40	Zr_2^{79+}	2	−1782.802 217 068	
		3	−1783.539 606 894	
		4	−1783.585 615 512	
		5	−1783.587 315 610	−1783.587 355 445
50	Sn_2^{99+}	2	−2803.286 356 845	
		3	−2804.566 122 743	
		4	−2804.656 452 590	
		5	−2804.659 770 918	−2804.659 807 931
60	Nd_2^{119+}	2	−4069.063 950 398	
		3	−4071.139 360 212	
		4	−4071.304 123 628	
		5	−4071.309 804 433	−4071.309 830 161
70	Yb_2^{139+}	2	−5593.251 717 146	
		3	−5596.462 436 297	
		4	−5596.746 534 092	
		5	−5596.754 858 416	−5596.754 864 752
80	Hg_2^{159+}	2	−7393.964 617 394	
		3	−7398.751 717 018	
		4	−7399.218 916 979	
		5	−7399.228 761 754	−7399.228 805 892
90	Th_2^{179+}	2	−9497.103 757 814	
		3	−9504.013 069 800	
		4	−9504.748 342 655	
		5	−9504.756 578 763	−9504.756 746 927

Continuation of Table 6.

Z	Ion	$N_{\max}$	Energy	Energy [170]
92	U_2^{183+}	2	−9957.149 867 657	
		3	−9964.557 040 570	
		4	−9965.357 892 685	
		5	−9965.365 278 947	−9965.365 468 058
100	Fm_2^{199+}	2	−11942.178 005 611	
		3	−11951.832 987 584	
		4	−11952.939 381 324	
		5	−11952.941 727 610	−11952.941 940 110
110	Ds_2^{219+}	2	−14796.324 879 456	
		3	−14809.322 202 267	
		4	−14810.852 901 248	
		5	−14810.898 911 675	
118	Og_2^{235+}	2	−17461.232 762 069	
		3	−17477.122 912 713	
		4	−17479.073 413 320	
		5	−17479.125 249 624	
121	$\square_2^{241+}$	2	−18577.427 339 685	
		3	−18594.349 381 894	
		4	−18596.454 717 052	
		5	−18596.509 996 585	

4.3.6. Summary to Section 4.3

A new computational scheme based on a modified Newton-type method in combination with negative curvature methods is developed for solving the minimax (or maximin) problem. The effectiveness of the proposed scheme is confirmed by numerical experiments solving benchmark problems. The corresponding iterative processes converge to the desired minimax points, not only for initial approximations given in the convex-concave domain, but also for those given in the nonconvex-nonconcave, convex-nonconcave, and nonconvex-concave domains.

A new computational scheme is developed for the high accuracy calculation of upper estimations for the ground state energy in the relativistic approximation of the Dirac equation with a one-electron two-center Coulomb potential. In calculations for the large and small radial components of each Dirac spinor orbital, independent linear combinations of non-integer Slater-type spinor orbitals are used. The efficiency of using such independent large and small components enables the use of minimax optimization, thereby eliminating spurious solutions without using any additional conditions. Our numerical results show that to achieve an electron energy accuracy of the order of 10^{-8} in the relativistic approximation with charges $Z = 1 - 121$ of atomic nuclei, only 62 basis functions are required, which is significantly less than those used in previous calculations concerning the two-center Dirac equation.

5. Conclusion

One can conclude that, despite its nearly 60-year history, numerical schemes based on CANM remain in demand and are actively used to solve a wide range of computational problems within nonlinear models of complex physical systems studied at JINR and other scientific

centres. The results of CANM-based investigations, obtained at JINR in different years, served a basis for the theoretical studies of complex nonlinear processes in nuclear physics, condensed matter physics, quantum mechanics, quantum-field phenomena, astrophysics, etc.

As mentioned in Section 1, the first numerically obtained energy levels of mesomolecule states gave a starting point for further studies in this field. The experimental confirmation of the existence of numerically predicted in [16–18] weakly bound states in muonic molecules of deuterium and tritium at the Dzhelepov Laboratory of Nuclear Problems of JINR and, as a consequence, the high efficiency of muon catalysis in a mixture of deuterium and tritium stimulated work on muon-catalyzed fusion throughout the world. These CANM-based calculations fostered the development of other computational methods in application to the problem: different variants of variational calculations, the hyperspherical approach, and others.

Numerically obtained stationary polaron states were used within numerical simulations of the hydrated electron states formation, see [171] and references therein. Interest in theoretical studies and CANM-based algorithms for the numerical study of QCD-inspired quarconium models [2] has been renewed in recent years in the context of the planned experiments of the NICA megascience project [172]. CANM-based numerical analysis [173, 174] allowed one to identify and classify the instabilities of gap solitons, which confirmed theoretical predictions in [173]. These results were later reproduced numerically and theoretically by other authors. A new physical phenomenon numerically predicted by T. L. Boyadzhiev and co-authors — a specific dependence of the critical current on the magnetic field in a nonuniform long Josephson junction [13] — was confirmed experimentally [175]. The use of CANM iteration within the original numerical continuation procedure made it possible to obtain new stable stationary complexes of light [77] and dark [88, 89] solitons in a parametrically driven, damped nonlinear Schrödinger equation. This computational scheme was later adapted for the numerical study of travelling ac-driven and parametrically driven solitons [23, 74, 75]. This approach was also extended to the case of time-periodic solitons as solutions of the corresponding two-dimensional BVP. This enabled, within a unified approach, to obtain new insights into the full complexity of coexisting stable localised states [23, 24].

The application of the constructed highly correlated helium ground state wave function on the exponential basis, which provides a good accuracy of the energy, yielded several important physical results for the single and double ionization processes of the helium in collisions with an electron and a proton, presented in [128–137] and others. Using CANM, the entire rotational-vibrational spectrum of narrow-band metastable states of the beryllium dimer was firstly calculated [36]. A new computational scheme based on a modified Newton-type method in combination with negative curvature methods was developed for solving the minimax (or maximin) problem. This scheme was applied to the high accuracy calculation of upper estimations for the ground state energy in the relativistic approximation of the Dirac equation with a one-electron two-center Coulomb potential. The obtained numerical results show that minimax optimization is more efficient than minimization for calculating the energies of the Dirac equation [169].

The viability and effectiveness of CANM in the XXI century is confirmed by the fact that it was the primary numerical research tool in 11 candidate and doctoral theses defended between 2000 and 2025 by MLIT staff and colleagues from the JINR Member States working at MLIT.

Finally, we will list the program complexes implementing the CANM numerical solution of various nonlinear problems, which were elaborated at MLIT JINR and are available via the JINR program library JINRLIB.

- SLIP1 — program of the numerical solution of the Sturm–Liouville problem basing on the continuous analog of the Newton's method[2] [57]
- SLIPS2 — program complex for numerical solution of the Sturm–Liouville problem for the system of differential equations[3] [68]
- SLIPH4 — program complex for numerical solution of the Sturm–Liouville problem[4] [55]
- SNIDE — program complex for solving the eigenvalue problem for integro-differential equation on the basis of CANM[5] [61]
- SYSINT(SISINTM) — program complex for numerical solution of the eigenvalue problem for the system of integral equations[6] [69]
- CONTIN-NLIN — program complex for CANM-based numerical continuation[7], [70]
- SCATTERH6 — the calculations for a phase shift and wave functions of the Schrödinger equations for a one-dimensional scattering problem[8]
- CANM — a program for numerical solution of a system of nonlinear equations using the continuous analog of Newton's method[9] [176]
- NINE — a program for numerical solution of the boundary problems for nonlinear differential equations on the basis of CANM[10] [41]
- SLIPM — a MAPLE package for numerical solution of Sturm-Liouville partial problems based on the continuous analog of Newton's method[11] [20]
- SLIPH4M — MAPLE program for numerical solution of the Sturm-Liouville problem[12] [21]
- KANTBP 4M — program for solving boundary problems of the self-adjoint system of ordinary second order differential equations[13] [71]

Acknowledgements

The authors are grateful to the Directorate of JINR and MLIT for the honourable proposal to write this review article on the occasion of the 70th Anniversary of the Joint Institute for Nuclear Research and the 60th Anniversary of the Meshcheryakov Laboratory of Information Technologies of JINR. We thank S. I. Vinitsky, A. A. Gusev, Yu. V. Popov, B. B. Joulakian, I. V. Barashenkov, N. A. Alexeeva, A. A. Bogolubskaya, M. V. Bashashin, V. L. Derbov, and A. V. Mitin in collaboration with whom a number of results presented in Sections 3 and 4 were obtained. We are grateful to T. P. Puzynina, T. Zhanlav, and V. T. Thach for their contribution to the development of new algorithms for calculating the CANM iteration parameter described in Sections 2.2.1, 2.2.2, 2.4.1, and 2.4.2.

We express our gratitude to T. A. Strizh, V. S. Melezhik, P. G. Akishin, Yu. L. Kalinovsky, A. A. Gusev, Yu. V. Popov, and B. B. Joulakian for their useful comments and recommendations during the writing of this review article.

[2] http://wwwinfo.jinr.ru/programs/jinrlib/slip/indexe.html#SLIP1
[3] http://wwwinfo.jinr.ru/programs/jinrlib/slip/indexe.html#SLIPS2
[4] http://wwwinfo.jinr.ru/programs/jinrlib/slip/indexe.html#SLIPH4
[5] http://wwwinfo.jinr.ru/programs/jinrlib/snide/indexe.html
[6] http://wwwinfo.jinr.ru/programs/jinrlib/sysint/indexe.html
[7] http://wwwinfo.jinr.ru/programs/jinrlib/contin-nlin/indexe.html
[8] http://wwwinfo.jinr.ru/programs/jinrlib/scatterh6/indexe.html
[9] https://data.mendeley.com/datasets/4v5cwrxfh6/1
[10] http://wwwinfo.jinr.ru/programs/jinrlib/nine/indexe.html
[11] http://wwwinfo.jinr.ru/programs/jinrlib/slipm/indexe.html
[12] http://wwwinfo.jinr.ru/programs/jinrlib/sliph4m/indexe.html
[13] http://wwwinfo.jinr.ru/programs/jinrlib/kantbp4m/indexe.html

Most of the numerical calculations presented in Sections 3 and 4 were performed on the computational resources of the JINR Multifunctional Information and Computing Complex (MICC), including the HybriLIT heterogeneous computing platform and the "Govorun" supercomputer. We are thankful to the MICC and HybriLIT teams for their support.

We would like to highlight the significant contribution of Professor Igor Viktorovich Puzynin to the field of theoretical research and practical developments of CANM and express our gratitude to him.

Author contributions

The contributions of the authors are equal.

Funding

The results of the numerical study presented in Section 3 were obtained under partial support within the long-term RSA-JINR Cooperation Program. The results presented in Section 4 were partially supported by the grants of the RFFI and the Ministry of Education, Culture, Science and Sports of Mongolia (No. 20-51-44001); the Ministry of Education and Science of Mongolia (No. ShuG 2021/137); the Foundation of Science and Technology of Mongolia (No. SST_007/2015); the JINR Bogoliubov-Infeld program; the JINR Hulubei-Meshcheryakov program; and the Peoples' Friendship University of Russia (RUDN) Strategic Academic Leadership program (No. 021934-0-000).

Conflicts of Interest

The authors declare no conflicts of interest.

References

[1] E. P. Zhidkov, G. I. Makarenko, I. V. Puzynin, Continuous analog of the Newton method in non-linear physical problems, Soviet Journal of Particles and Nuclei 4 (1) (1973) 53.

[2] I. V. Puzynin, I. V. Amirkhanov, E. Zemlyanaya, V. N. Pervushin, T. P. Puzynina, T. A. Strizh, V. D. Lakhno, The generalized continuous analog of Newton's method for the numerical study of some nonlinear quantum-field models, Physics of Particles and Nuclei 30 (1) (1999) 87–110. doi:10.1134/1.953099.

[3] E. P. Zhidkov, I. V. Puzynin, A method for introducing a parameter when solving boundary value problems for second-order nonlinear ordinary differential equations, USSR Computational Mathematics and Mathematical Physics 7 (5) (1967) 157–170.

[4] M. K. Gavurin, Nonlinear functional equations and continuous analogues of iterative methods, Izvestiya Vysshikh Uchebnykh Zavedenii. Matematika 5 (6) (1958) 18–31, (in Russian).

[5] I. V. Puzynin, T. L. Boyadzhiev, S. I. Vinitskii, E. V. Zemlyanaya, T. P. Puzynina, O. Chuluunbaatar, Methods of computational physics for investigation of models of complex physical systems, Physics of Particles and Nuclei 38 (1) (2007) 70–116. doi:10.1134/s1063779607010030.

[6] F. Gareev, S. A. Goncharov, E. P. Zhidkov, I. V. Puzynin, B. N. Khoromskii, R. M. Yamaleev, The scattering problem in quantum mechanics as an eigenvalue problem, USSR Computational Mathematics and Mathematical Physics 17 (2) (1977) 116–128.

[7] J. Bang, F. A. Gareev, I. V. Puzynin, R. M. Jamalejev, Single-particle quasistationary states in spherical and deformed nuclei, Nuclear Physics A 261 (1) (1976) 59–76.

[8] L. I. Ponomarev, I. V. Puzynin, T. P. Puzynina, L. N. Somov, The scattering problem in quantum mechanics as an eigenvalue problem, Annals of Physics 110 (2) (1978) 274–286.

[9] A. T. Filippov, I. V. Puzynin, D. P. Mavlo, Numerical methods for solving some singular boundary value problems of quantum mechanics and quantum field theory. I, Journal of Computational Physics 22 (2) (1976) 150–170. doi:10.1016/0021-9991(76)90073-5.

[10] V. S. Melezhik, Continuous analog of Newton method in the multichannel scattering problem, Journal of Computational Physics 65 (1) (1986) 1–17. doi:10.1016/0021-9991(86)90001-x.

[11] V. S. Melezhik, New method for solving multidimensional scattering problem, Journal of Computational Physics 92 (1) (1991) 67–81. doi:10.1016/0021-9991(91)90292-s.

[12] S. I. Vinitskii, I. V. Puzynin, Yu. S. Smirnov, High-precision calculations of the multichannel scattering problem for processes involving mesic atoms, Physics of Atomic Nuclei 55 (12) (1992) 1830–1838.

[13] A. T. Filippov, Yu. S. Gal'pern, T. L. Boyadjiev, I. V. Puzynin, Critical currents in Josephson junctions with microinhomogeneities attracting solitons, Physics Letters A 120 (1) (1987) 47–50. doi:10.1016/0375-9601(87)90262-3.

[14] I. V. Barashenkov, T. L. Boyadjiev, I. V. Puzynin, T. Zhanlav, Stability of moving bubbles in a system of interacting bosons, Physics Letters A 135 (2) (1989) 125–128. doi:10.1016/0375-9601(89)90658-0.

[15] L. I. Ponomarev, Muon catalysed fusion, Contemporary Physics 31 (4) (1990) 219–245. doi:10.1080/00107519008222019.

[16] S. I. Vinitskii, V. S. Melezhik, L. I. Ponomarev, I. V. Puzynin, T. P. Puzynina, L. N. Somov, N. F. Truskova, Calculation of the energy levels of μ-mesic molecules of hydrogen isotopes in the adiabatic representation of the three-body problem, Soviet Journal of Experimental and Theoretical Physics 52 (1980) 353–360.

[17] V. S. Melezhik, I. V. Puzynin, T. P. Puzynina, L. N. Somov, Numerical solution of a system of integrodifferential equations arising from the quantum mechanical three-body problem with Coulomb interaction, Journal of Computational Physics 54 (2) (1984) 221–236. doi:10.1016/0021-9991(84)90115-3.

[18] A. D. Gocheva, V. V. Gusev, V. S. Melezhik, L. I. Ponomarev, I. V. Puzynin, T. P. Puzynina, L. N. Somov, S. I. Vinitsky, High accuracy energy-level calculations of the rotational-vibrational weakly bound states of ddμ and dtμ mesic molecules, Physics Letters B 153 (6) (1985) 349–352. doi:10.1016/0370-2693(85)90470-8.

[19] T. Zhanlav, I. V. Puzynin, An evolutionary Newton procedure for solving nonlinear equations, Computational Mathematics and Mathematical Physics 32 (1) (1992) 1–9.

[20] I. V. Puzynin, T. P. Puzynina, V. T. Thach, SLIPM – Maple programm for numerical solution of Sturm-Liouville partial problem with the help of the continuous analogue of Newton's method, Bulletin of Peoples' Friendship University of Russia. Mathematics, Information sciences. Physics 2 (2) (2010) 90–98, (in Russian).

[21] V. T. Thach, T. P. Puzynina, SLIPH4M — Program for numerical solution of the Sturm–Liouville partial problem, Journal of Software and Systems 95 (3) (2011) 75–80, (in Russian).

[22] T. Zhanlav, O. Chuluunbaatar, New Developments of Newton-Type Iterations for Solving Nonlinear Problems, Springer Nature Switzerland, 2024. doi:10.1007/978-3-031-63361-4.

[23] I. V. Barashenkov, E. V. Zemlyanaya, Travelling solitons in the externally driven nonlinear Schrödinger equation, Journal of Physics A: Mathematical and Theoretical 44 (46) (2011) 465211. doi:10.1088/1751-8113/44/46/465211.

[24] I. V. Barashenkov, E. V. Zemlyanaya, T. C. van Heerden, Time-periodic solitons in a damped-driven nonlinear Schrödinger equation, Physical Review E 83 (5) (2011) 056609. doi:10.1103/physreve.83.056609.

[25] I. V. Barashenkov, E. V. Zemlyanaya, Soliton complexity in the damped-driven nonlinear Schrödinger equation: Stationary to periodic to quasiperiodic complexes, Physical Review E 83 (5) (2011) 056610. doi:10.1103/physreve.83.056610.

[26] N. V. Alexeeva, I. V. Barashenkov, A. A. Bogolubskaya, E. V. Zemlyanaya, Understanding oscillons: Standing waves in a ball, Physical Review D 107 (7) (2023) 076023. doi:10.1103/physrevd.107.076023.

[27] P. Kh. Atanasova, T. L. Boyadjiev, Yu. M. Shukrinov, E. V. Zemlyanaya, Numerical modeling of long Josephson junctions in the frame of double sine-Gordon equation, Mathematical Models and Computer Simulations 3 (3) (2011) 389–398. doi:10.1134/s2070048211030033.

[28] P. Kh. Atanasova, T. L. Boyadjiev, E. V. Zemlyanaya, Yu. M. Shukrinov, Numerical study of magnetic flux in the LJJ model with double sine-Gordon equation, Lecture Notes in Computer Sciences 6046 (2011) 347–352. doi:10.1007/978-3-642-18466-6_41.

[29] P. Kh. Atanasova, T. L. Boyadjiev, Yu. M. Shukrinov, E. V. Zemlyanaya, P. Seidel, Influence of Josephson current second harmonic on stability of magnetic flux in long junctions, Journal of Physics: Conference Series 248 (2010) 012044. doi:10.1088/1742-6596/248/1/012044.

[30] P. Kh. Atanasova, E. V. Zemlyanaya, Yu. M. Shukrinov, Interconnection between static regimes in the LJJs described by the double sine-Gordon equation, Journal of Physics: Conference Series 393 (2012) 012023. doi:10.1088/1742-6596/393/1/012023.

[31] P. Kh. Atanasova, E. V. Zemlyanaya, Numerical investigation of bifurcations in long Josephson junctions with second harmonic in the current-phase relation, Comptes Rendus de l'Académie Bulgare des Sciences 68 (12) (2015) 1483–1490.

[32] A. A. Gusev, L. L. Hai, O. Chuluunbaatar, V. Ulziibayar, S. I. Vinitsky, V. L. Derbov, A. Góźdź, V. A. Rostovtsev, Symbolic-numeric solution of boundary-value problems for the Schrödinger equation using the finite element method: Scattering problem and resonance states, Lecture Notes in Computer Science 9301 (2015) 182–197. doi:10.1007/978-3-319-24021-3_14.

[33] A. A. Gusev, V. P. Gerdt, L. L. Hai, V. L. Derbov, S. I. Vinitsky, O. Chuluunbaatar, Symbolic-numeric algorithms for solving bvps for a system of odes of the second order: Multichannel scattering and eigenvalue problems, Lecture Notes in Computer Science 9890 (2016) 212–227. doi:10.1007/978-3-319-45641-6_14.

[34] A. A. Gusev, S. I. Vinitsky, O. Chuluunbaatar, A. Góźdź, V. L. Derbov, P. M. Krassovitskiy, Adiabatic representation for atomic dimers and trimers in collinear configuration, Physics of Atomic Nuclei 81 (6) (2018) 945–970. doi:10.1134/s1063778818060169.

[35] A. A. Gusev, O. Chuluunbaatar, V. Derbov, R. Nazmitdinov, S. Vinitsky, P. Wen, C. Lin, H. M. Jia, L. L. Hai, Symbolic-numerical algorithm for solving the problem of heavy ion collisions in an optical model with a complex potential, Lecture Notes in Computer Science 14139 (2023) 128–140. doi:10.1007/978-3-031-41724-5_7.

[36] V. L. Derbov, G. Chuluunbaatar, A. A. Gusev, O. Chuluunbaatar, S. I. Vinitsky, A. Góźdź, P. M. Krassovitskiy, I. Filikhin, A. V. Mitin, Spectrum of beryllium dimer in ground $X^1\Sigma_g^+$ state, Journal of Quantitative Spectroscopy and Radiative Transfer 262 (2021) 107529. doi:10.1016/j.jqsrt.2021.107529.

[37] I. Hristov, R. Hristova, I. Puzynin, T. Puzynina, Z. Sharipov, Z. Tukhliev, New families of periodic orbits for the planar three-body problem computed with high precision, CEUR Workshop Proceedings 3191 (2022) 45–50.

[38] I. Hristov, R. Hristova, I. Puzynin, T. Puzynina, Z. Sharipov, Z. Tukhliev, Searching for new nontrivial choreographies for the planar three-body problem, Physics of Particles and Nuclei 55 (3) (2024) 495–497. doi:10.1134/s1063779624030444.

[39] R. V. Polyakova, I. P. Yudin, Continuous analogue of Newton method in beam dynamics problems, Bulletin of Peoples' Friendship University of Russia. Mathematics, Information sciences. Physics (2) (2011) 83–91.

[40] T. Tóth, M. Dovica, J. Buša, J. Buša Jr., Verification of coordinate measuring machine using a gauge block, Measurment Science Review 24 (6) (2024) 225–233. doi:10.2478/msr-2024-0030.

[41] B. Batgerel, E. V. Zemlyanaya, I. V. Puzynin, NINE: computer code for numerical solu-

tion of the boundary problems for nonlinear differential equations on the basis of CANM, Computer Research and Modeling 2 (2) (2012) 315–324, (in Russian). doi:10.20537/2076-7633-2012-4-2-315-324.

[42] M. Bordag, D. N. Voskresensky, Generation of a scalar vortex in a rotational frame, Physical Review D 112 (8) (2025) 085026. doi:10.1103/y2lc-27pn.

[43] T. Kato, Perturbation Theory for Linear Operators, Springer-Verlag Berlin, 1995.

[44] J. M. Ortega, W. C. Reinboldt, Iterative solution of nonlinear equations in several variables, New-York-London, Academic Press, 1970.

[45] D. F. Davidenko, On application of method of variation of parameter to the theory of nonlinear functional equations, Ukrainian Mathematical Journal 7 (1) (1955) 18–28, (in Russian).

[46] D. A. Kirzhnits, N. Z. Takibaev, New approach to 3 and more body problem, Soviet Journal of Nuclear Physics 25 (1) (1977) 370–376.

[47] G. I. Marchuk, Splitting Methods, Moscow: Nauka, 1988, (in Russian).

[48] G. I. Marchuk, V. V. Shaidurov, Difference Methods and Their Extrapolations, Springer New York, 1983. doi:10.1007/978-1-4613-8224-9.

[49] L. Alexandrov, Regularized trajectories of Newton-type approximation for solving of nonlinear equations, Differencial'nye Uravnenija 13 (7) (1977) 1281–1292, (in Russian).

[50] E. K. Blum, A. F. Chang, A numerical method for the solution of the double eigenvalue problem, IMA Journal of Applied Mathematics 22 (1) (1978) 29–42. doi:10.1093/imamat/22.1.29.

[51] L. Bracci, G. Fiorentini, Mesic molecules and muon catalysed fusion, Physics Reports 86 (4) (1982) 169–216. doi:10.1016/0370-1573(82)90095-3.

[52] I. V. Puzynin, S. I. Vinitsky, Energy levels of mesic molecule, Journal of Muon Catalyzed Fusion 3 (1988) 307–320.

[53] T. Zhanlav, I. V. Puzynin, The convergence of iterations based on a continuous analogue of Newton's method, Computational Mathematics and Mathematical Physics 32 (6) (1992) 729–737.

[54] O. Yu. Kul'chitskii, L. I. Shimelevich, Determination of the initial approximation for Newton's method, USSR Computational Mathematics and Mathematical Physics 14 (4) (1974) 188–190. doi:10.1016/0041-5553(74)90083-4.

[55] I. V. Puzynin, T. P. Puzynina, T. A. Strizh, SLIPH4 — Program for numerical solution of Sturm–Liouville problem, JINR Communication P11-87-332, Dubna, (in Russian) (1987).

[56] E. V. Zemlyanaya, I. V. Puzynin, T. P. Puzynina, PROGS2H4 — Program for solution of boundary problem for system of differential equations, JINR Communication P11-97-414, Dubna, (in Russian) (1997).

[57] I. V. Puzynin, T. P. Puzynina, Program of approximate solution of Sturm–Liouville problem using the continuous analog of Newton's method, Collection of Scientific Papers in Collaboration of JINR (Dubna, USSR) and Central Research Institute for Physics (Hungary, Budapest) (1974) 93–112.

[58] K. A. Lebedev, A method of finding the initial approximation for Newton's method, Computational Mathematics and Mathematical Physics 36 (3) (1996) 283–289.

[59] V. V. Ermakov, N. N. Kalitkin, The optimal step and regularization for Newton's method, USSR Computational Mathematics and Mathematical Physics 21 (2) (1981) 235–242. doi:10.1016/0041-5553(81)90022-7.

[60] S. I. Vinitskii, L. I. Ponomarev, I. V. Puzynin, T. P. Puzynina, Newton's process in perturbation theory with continuous inclusion of interaction, JINR Communication P4-10942, Dubna, (in Russian) (1977).

[61] I. V. Amirkhanov, E. V. Zemlyanaya, T. P. Puzynina, SNIDE – Program package for solution of characteristic constant problems for integral-differential equation on the base of CANM, JINR Communication P11-91-87, Dubna, (in Russian) (1991).

[62] S. I. Vinitskii, I. V. Puzynin, Yu. S. Smirnov, Solution of the scattering problem on the basis of multiparameter Newton schemes – single-channel scattering, Soviet Journal of Nuclear Physics 52 (10) (1990) 746–754.

[63] I. V. Barashenkov, Yu. S. Smirnov, N. V. Alexeeva, Bifurcation to multisoliton complexes in the ac-driven, damped nonlinear Schrödinger equation, Physical Review E 57 (2) (1998) 2350–2364. doi:10.1103/physreve.57.2350.

[64] G. N. Chuev, V. D. Lakhno, Perspectives of Polarons, World Scientific, 1996. doi:10.1142/3208.

[65] P. G. Akishin, I. V. Puzynin, Yu. S. Smirnov, The Newtonian continuation method for numerical study of 3D polaron problem, Lecture Notes in Computer Science 1196 (1997) 1–8. doi:10.1007/3-540-62598-4_72.

[66] I. V. Amirkhanov, I. V. Puzynin, T. P. Puzynina, T. A. Strizh, E. V. Zemlyanaya, CANM in numerical investgation of QCD problems, Lecture Notes in Computer Science 1196 (1997) 9–16. doi:10.1007/3-540-62598-4_73.

[67] L. V. Kantorovich, Approximate solution of functional equations, Uspehi Mathematicheskih Nauk 11 (6) (1956) 99–116, (in Russian).

[68] T. P. Puzynina, SLIPS2 — Program for numerical solution of Sturm-Liouville problem for system of differential equations, JINR Communication P11-89-728, Dubna, (in Russian) (1989).

[69] E. V. Zemlyanaya, SYSINT(SYSINTM) — Program complex for numerical solution of characteristic constant problems for system of integral equations, JINR Communications P11-94-120, Dubna, (in Russian) (1994).

[70] E. V. Zemlyanaya, I. V. Barashenkov, Numerical study of travelling solitons in parametrically driven, damped nonlinear Shcrödinger equation, Matematicheskoe Modelirovanie 17 (1) (2005) 65–78, (in Russian).

[71] G. Chuluunbaatar, A. A. Gusev, O. Chuluunbaatar, S. I. Vinitsky, L. L. Hai, KANTBP 4M — Program for solving the scattering problem for a system of ordinary second-order differential equations, EPJ Web of Conferences 226 (2020) 02008. doi:10.1051/epjconf/202022602008.

[72] G. Chuluunbaatar, A. A. Gusev, V. L. Derbov, S. I. Vinitsky, L. L. Hai, O. Chuluunbaatar, V. V. Gerdt, A Maple implementation of the finite element method for solving boundary-value problems for systems of second-order ordinary differential equations, Maple Conference 2020 1414 (2021) 152–166. doi:10.1007/978-3-030-81698-8_11.

[73] E. V. Zemlyanaya, I. V. Barashenkov, Numerical study of the multisoliton complexes in the damped-driven NLS, Matematicheskoe Modelirovanie 16 (3) (2004) 3–14, (in Russian).

[74] I. V. Barashenkov, E. V. Zemlyanaya, M. Bár, Traveling solitons in the parametrically driven nonlinear Schrödinger equation, Physical Review E 64 (1) (2001) 016603. doi:10.1103/physreve.64.016603.

[75] E. V. Zemlyanaya, I. V. Barashenkov, Traveling solitons in the damped-driven nonlinear Schrödinger equation, SIAM Journal on Applied Mathematics 64 (3) (2004) 800–818. doi:10.1137/s0036139903424837.

[76] I. V. Barashenkov, M. M. Bogdan, V. I. Korobov, Stability diagram of the phase-locked solitons in the parametrically driven, damped nonlinear Schrödinger equation, Europhysics Letters (EPL) 15 (2) (1991) 113–118. doi:10.1209/0295-5075/15/2/001.

[77] I. V. Barashenkov, E. V. Zemlyanaya, Stable complexes of parametrically driven, damped nonlinear Schrödinger solitons, Physical Review Letters 83 (13) (1999) 2568–2571. doi:10.1103/physrevlett.83.2568.

[78] N. V. Alexeeva, I. V. Barashenkov, D. E. Pelinovsky, Dynamics of the parametrically driven NLS solitons beyond the onset of the oscillatory instability, Nonlinearity 12 (1) (1999) 103–140. doi:10.1088/0951-7715/12/1/007.

[79] M. Bondila, I. V. Barashenkov, M. M. Bogdan, Topography of attractors of the parametrically driven nonlinear Schrödinger equation, Physica D: Nonlinear Phenomena 87 (1–4) (1995) 314–

320. doi:10.1016/0167-2789(95)00126-o.

[80] E. V. Zemlyanaya, I. V. Barashenkov, N. V. Alexeeva, Temporally-periodic solitons of the parametrically driven damped nonlinear Schrödinger equation, Lecture Notes in Computer Science 5434 (2009) 139–150. doi:10.1007/978-3-642-00464-3_13.

[81] E. V. Zemlyanaya, N. V. Alexeeva, Oscillating solitons of the driven, damped nonlinear Schrödinger equation, Theoretical and Mathematical Physics 159 (3) (2009) 870–876. doi:10.1007/s11232-009-0075-6.

[82] E. Zemlyanaya, N. Alexeeva, Numerical study of stationary, time-periodic, and quasiperiodic two-soliton complexes in the damped-driven nonlinear Schrödinger equation, Lecture Notes in Computer Science 7125 (2012) 240–245. doi:10.1007/978-3-642-28212-6_27.

[83] N. V. Alexeeva, E. V. Zemlyanaya, Breathers in a damped-driven nonlinear Schrödinger equation, Theoretical and Mathematical Physics 168 (1) (2011) 858–864. doi:10.1007/s11232-011-0069-z.

[84] E. V. Zemlyanaya, N. V. Alexeeva, Numerical study of time-periodic solitons in the damped-driven NLS, International Journal of Numerical Analysis and Modeling, Series B. 2 (2–3) (2011) 248–261.

[85] R. Seydel, From equilibrium to chaos. Practical bifurcation and stability analysis, Elsevier Science Publishing Co., 1988.

[86] A. A. Samarskii, P. N. Vabishchevich, Computational Heat Transfer, Volume 1: Mathematical Modelling, Viley, 1996.

[87] E. L. Allgower, K. Georg, Numerical Continuation Methods, Springer Berlin Heidelberg, 1990. doi:10.1007/978-3-642-61257-2.

[88] I. V. Barashenkov, S. R. Woodford, E. V. Zemlyanaya, Parametrically driven dark solitons, Physical Review Letters 90 (5) (2003) 054103. doi:10.1103/physrevlett.90.054103.

[89] I. V. Barashenkov, S. R. Woodford, E. V. Zemlyanaya, Interactions of parametrically driven dark solitons. I. Néel-Néel and Bloch-Bloch interactions, Physical Review E 75 (2) (2007) 026604. doi:10.1103/physreve.75.026604.

[90] I. V. Barashenkov, N. V. Alexeeva, E. V. Zemlyanaya, Two- and three-dimensional oscillons in nonlinear Faraday resonance, Physical Review Letters 89 (10) (2002) 104101. doi:10.1103/physrevlett.89.104101.

[91] N. V. Alexeeva, E. V. Zemlyanaya, Nodal two-dimensional solitons in nonlinear parametric resonance, Lecture Notes in Computer Science 3401 (2005) 91–99. doi:10.1007/978-3-540-31852-1_9.

[92] N. A. Voronov, I. Y. Kobzarev, N. B. Konyukhova, Possibility of the existence of X mesons of a new type, Journal of Experimental and Theoretical Physics Letters 22 (1975) 290–291.

[93] I. L. Bogolyubskii, V. G. Makhankov, Lifetime of pulsating solitons in certain classical models, Journal of Experimental and Theoretical Physics Letters 24 (1976) 12–14.

[94] I. L. Bogolyubskii, V. G. Makhankov, Dynamics of spherically symmetrical pulsons of large amplitude, Journal of Experimental and Theoretical Physics Letters 25 (1977) 107–110.

[95] M. Gleiser, Pseudostable bubbles, Physical Review D 49 (6) (1994) 2978–2981. doi:10.1103/physrevd.49.2978.

[96] E. J. Copeland, M. Gleiser, H.-R. Müller, Oscillons: Resonant configurations during bubble collapse, Physical Review D 52 (4) (1995) 1920–1933. doi:10.1103/physrevd.52.1920.

[97] E. P. Honda, M. W. Choptuik, Fine structure of oscillons in the spherically symmetric φ^4 Klein–Gordon model, Physical Review D 65 (8) (2002) 084037. doi:10.1103/physrevd.65.084037.

[98] G. Fodor, P. Forgács, P. Grandclément, I. Rácz, Oscillons and quasi-breathers in the ϕ^4 Klein–Gordon model, Physical Review D 74 (12) (2006) 124003. doi:10.1103/physrevd.74.124003.

[99] I. V. Barashenkov, N. V. Alexeeva, Variational formalism for the Klein-Gordon oscillon, Physical Review D 108 (9) (2023) 096022. doi:10.1103/physrevd.108.096022.

[100] N. V. Alexeeva, I. V. Barashenkov, A. Dika, R. De Sousa, The energy-frequency diagram of the (1+1)-dimensional ϕ^4 oscillon, Journal of High Energy Physics 2024 (10) (2024) 136. doi:10.1007/jhep10(2024)136.

[101] E. V. Zemlyanaya, A. A. Bogolubskaya, M. V. Bashashin, N. V. Alexeeva, The ϕ^4 oscillons in a ball: Numerical approach and parallel implementation, Physics of Particles and Nuclei 55 (3) (2024) 505–508. doi:10.1134/s106377962403095x.

[102] E. V. Zemlyanaya, A. A. Bogolubskaya, M. V. Bashashin, N. V. Alexeeva, Numerical study of the ϕ^4 standing waves in a ball of finite radius, Discrete and Continuous Models and Applied Computational Science 32 (1) (2024) 106–111. doi:10.22363/2658-4670-2024-32-1-106-111.

[103] E. V. Zemlyanaya, A. A. Bogolubskaya, M. V. Bashashin, N. V. Alexeeva, ϕ^4 oscillons as standing waves in a ball: A numerical study, Physics of Particles and Nuclei 56 (6) (2025) 1655–1659. doi:10.1134/S1063779625701047.

[104] C. Chicone, Ordinary Differential Equations with Applications. Texts in Applied Mathematics, Vol. 34, Springer, New York, 2006. doi:10.1007/0-387-35794-7.

[105] L. U. Ancarani, T. Montagnese, C. Dal Cappello, Role of the helium ground state in $(e, 3e)$ processes, Physical Review A 70 (1) (2004) 012711. doi:10.1103/physreva.70.012711.

[106] S. Jones, J. H. Macek, D. H. Madison, Test of the Pluvinage wave function for the helium ground state, Physical Review A 70 (1) (2004) 012712. doi:10.1103/physreva.70.012712.

[107] S. Jones, J. H. Macek, D. H. Madison, Three-Coulomb-wave Pluvinage model for Compton double ionization of helium in the region of the cross-section maximum, Physical Review A 72 (1) (2005) 012718. doi:10.1103/physreva.72.012718.

[108] S. Jones, D. H. Madison, Role of the ground state in electron-atom double ionization, Physical Review Letters 91 (7) (2003) 073201. doi:10.1103/physrevlett.91.073201.

[109] M. Brauner, J. S. Briggs, H. Klar, Triply-differential cross sections for ionisation of hydrogen atoms by electrons and positrons, Journal of Physics B: Atomic, Molecular and Optical Physics 22 (14) (1989) 2265–2287. doi:10.1088/0953-4075/22/14/010.

[110] P. Pluvinage, Fonction d'onde approchée à un paramètre pour l'état fondamental des atomes à deux électrons, Annales de Physique 12 (5) (1950) 145–152. doi:10.1051/anphys/195012050145.

[111] P. Pluvinage, Nouvelle famille de solutions approchées pour certaines équations de Schrödinger non séparables. application à l'état fondamental de l'hélium, Journal de Physique et le Radium 12 (8) (1951) 789–792. doi:10.1051/jphysrad:01951001208078900.

[112] T. Kato, On the eigenfunctions of many-particle systems in quantum mechanics, Communications on Pure and Applied Mathematics 10 (2) (1957) 151–177. doi:10.1002/cpa.3160100201.

[113] A. Lahmam-Bennani, I. Taouil, A. Duguet, M. Lecas, L. Avaldi, J. Berakdar, Origin of dips and peaks in the absolute fully resolved cross sections for the electron-impact double ionization of He, Physical Review A 59 (5) (1999) 3548–3555. doi:10.1103/physreva.59.3548.

[114] A. M. Frolov, Two-stage strategy for high-precision variational calculations, Physical Review A 57 (4) (1998) 2436–2439. doi:10.1103/physreva.57.2436.

[115] V. I. Korobov, Nonrelativistic ionization energy for the helium ground state, Physical Review A 66 (2) (2002) 024501. doi:10.1103/physreva.66.024501.

[116] Yu. V. Popov, L. U. Ancarani, Rigorous mathematical study of the He bound states, Physical Review A 62 (4) (2000) 042702. doi:10.1103/physreva.62.042702.

[117] C. L. Sech, Accurate analytic wavefunctions for two-electron atoms, Journal of Physics B: Atomic, Molecular and Optical Physics 30 (2) (1997) L47–L50. doi:10.1088/0953-4075/30/2/003.

[118] P. E. Gill, W. Murray, Newton-type methods for unconstrained and linearly constrained optimization, Mathematical Programming 7 (1) (1974) 311–350. doi:10.1007/bf01585529.

[119] O. Chuluunbaatar, I. V. Puzynin, S. I. Vinitsky, Uncoupled correlated calculations of helium isoelectronic bound states, Journal of Physics B: Atomic, Molecular and Optical Physics 34 (14)

(2001) L425–L432. doi:10.1088/0953-4075/34/14/101.

[120] E. A. Hylleraas, B. Undheim, Numerische berechnung der 2S-terme von ortho- und par-helium, Zeitschrift für Physik 65 (11–12) (1930) 759–772. doi:10.1007/bf01397263.

[121] E. Clementi, C. Roetti, Roothaan-Hartree-Fock atomic wavefunctions, Atomic Data and Nuclear Data Tables 14 (3–4) (1974) 177–478. doi:10.1016/s0092-640x(74)80016-1.

[122] E. A. Hylleraas, Neue berechnung der energie des heliums im grundzustande, sowie des tiefsten terms von ortho-helium, Zeitschrift für Physik 54 (5–6) (1929) 347–366. doi:10.1007/bf01375457.

[123] C. Eckart, The theory and calculation of screening constants, Physical Review 36 (5) (1930) 878–892. doi:10.1103/physrev.36.878.

[124] S. Chandrasekhar, Some remarks on the negative hydrogen ion and its absorption coefficient, The Astrophysical Journal 100 (1944) 176–180. doi:10.1086/144654.

[125] J. N. Silverman, O. Platas, F. A. Matsen, Simple configuration-interaction wave functions. i. two-electron ions: A numerical study, The Journal of Chemical Physics 32 (5) (1960) 1402–1406. doi:10.1063/1.1730930.

[126] J. Mitroy, I. E. McCarthy, E. Weigold, A natural orbital analysis of the helium $(e, 2e)$ spectrum, Journal of Physics B: Atomic and Molecular Physics 18 (20) (1985) 4149–4157. doi:10.1088/0022-3700/18/20/017.

[127] R. A. Bonham, D. A. Kohl, Simple correlated wavefunctions for the ground state of heliumlike atoms, The Journal of Chemical Physics 45 (7) (1966) 2471–2473. doi:10.1063/1.1727963.

[128] M. S. Schöffler, O. Chuluunbaatar, Yu. V. Popov, S. Houamer, J. Titze, T. Jahnke, L. Ph. H. Schmidt, O. Jagutzki, A. G. Galstyan, A. A. Gusev, Transfer ionization and its sensitivity to the ground-state wave function, Physical Review A 87 (3) (2013) 032715. doi:10.1103/physreva.87.032715.

[129] M. S. Schöffler, O. Chuluunbaatar, S. Houamer, A. Galstyan, J. N. Titze, L. Ph. H. Schmidt, T. Jahnke, H. Schmidt-Böcking, R. Dörner, Yu. V. Popov, A. A. Gusev, C. Dal Cappello, Two-dimensional electron-momentum distributions for transfer ionization in fast proton-helium collisions, Physical Review A 88 (4) (2013) 042710. doi:10.1103/physreva.88.042710.

[130] M. S. Schöffler, H.-K. Kim, O. Chuluunbaatar, S. Houamer, A. G. Galstyan, J. N. Titze, T. Jahnke, L. Ph. H. Schmidt, H. Schmidt-Böcking, R. Dörner, Yu. V. Popov, A. A. Bulychev, Transfer excitation reactions in fast proton-helium collisions, Physical Review A 89 (3) (2014) 032707. doi:10.1103/physreva.89.032707.

[131] H. Gassert, O. Chuluunbaatar, M. Waitz, F. Trinter, H.-K. Kim, T. Bauer, A. Laucke, Ch. Müller, J. Voigtsberger, M. Weller, J. Rist, M. Pitzer, S. Zeller, T. Jahnke, L. Ph. H. Schmidt, J. B. Williams, S. A. Zaytsev, A. A. Bulychev, K. A. Kouzakov, H. Schmidt-Böcking, R. Dörner, Yu. V. Popov, M. S. Schöffler, Agreement of experiment and theory on the single ionization of helium by fast proton impact, Physical Review Letters 116 (7) (2016) 073201. doi:10.1103/physrevlett.116.073201.

[132] O. Chuluunbaatar, S. A. Zaytsev, K. A. Kouzakov, A. Galstyan, V. L. Shablov, Yu. V. Popov, Fully differential cross sections for singly ionizing 1-Mev p +He collisions at small momentum transfer: Beyond the first born approximation, Physical Review A 96 (4) (2017) 042716. doi:10.1103/physreva.96.042716.

[133] O. Chuluunbaatar, K. A. Kouzakov, S. A. Zaytsev, A. S. Zaytsev, V. L. Shablov, Yu. V. Popov, H. Gassert, M. Waitz, H.-K. Kim, T. Bauer, A. Laucke, Ch. Müller, J. Voigtsberger, M. Weller, J. Rist, K. Pahl, M. Honig, M. Pitzer, S. Zeller, T. Jahnke, L. Ph. H. Schmidt, H. Schmidt-Böcking, R. Dörner, M. S. Schöffler, Single ionization of helium by fast proton impact in different kinematical regimes, Physical Review A 99 (6) (2019) 062711. doi:10.1103/physreva.99.062711.

[134] A. S. Zaytsev, D. S. Zaytseva, S. A. Zaytsev, L. U. Ancarani, O. Chuluunbaatar, K. A. Kouzakov,

Yu. V. Popov, Single ionization of helium by protons of various energies in the parabolic quasi-Sturmians approach, Atoms 11 (10) (2023) 124. doi:10.3390/atoms11100124.

[135] M. Kircher, F. Trinter, S. Grundmann, I. Vela-Perez, S. Brennecke, N. Eicke, J. Rist, S. Eckart, S. Houamer, O. Chuluunbaatar, Yu. V. Popov, I. P. Volobuev, K. Bagschik, M. N. Piancastelli, M. Lein, T. Jahnke, M. S. Schöffler, R. Dörner, Kinematically complete experimental study of Compton scattering at helium atoms near the threshold, Nature Physics 16 (7) (2020) 756–760. doi:10.1038/s41567-020-0880-2.

[136] O. Chuluunbaatar, S. Houamer, Yu. V. Popov, I. Volobuev, M. Kircher, R. Dörner, Compton ionization of atoms as a method of dynamical spectroscopy, Journal of Quantitative Spectroscopy and Radiative Transfer 272 (2021) 107820. doi:10.1016/j.jqsrt.2021.107820.

[137] M. Kircher, F. Trinter, S. Grundmann, G. Kastirke, M. Weller, I. Vela-Perez, A. Khan, C. Janke, M. Waitz, S. Zeller, T. Mletzko, D. Kirchner, V. Honkimäki, S. Houamer, O. Chuluunbaatar, Yu. V. Popov, I. P. Volobuev, M. S. Schöffler, L. Ph. H. Schmidt, T. Jahnke, R. Dörner, Ion and electron momentum distributions from single and double ionization of helium induced by Compton scattering, Physical Review Letters 128 (5) (2022) 053001. doi:10.1103/physrevlett.128.053001.

[138] S. A. Zaytsev, V. A. Knyr, Yu. V. Popov, A. Lahmam-Bennani, Application of the J-matrix method to Faddeev-Merkuriev equations for $(e, 2e)$ reactions: Beyond pseudostates, Physical Review A 75 (2) (2007) 022718. doi:10.1103/physreva.75.022718.

[139] X. M. Tong, C. D. Lin, Empirical formula for static field ionization rates of atoms and molecules by lasers in the barrier-suppression regime, Journal of Physics B: Atomic, Molecular and Optical Physics 38 (15) (2005) 2593–2600. doi:10.1088/0953-4075/38/15/001.

[140] K. Patkowski, V. Špirko, K. Szalewicz, On the elusive twelfth vibrational state of beryllium dimer, Science 326 (5958) (2009) 1382–1384. doi:10.1126/science.1181017.

[141] A. V. Mitin, Ab initio calculations of weakly bonded He_2 and Be_2 molecules by MRCI method with pseudo-natural molecular orbitals, International Journal of Quantum Chemistry 111 (11) (2010) 2560–2567. doi:10.1002/qua.22691.

[142] J. Koput, The ground-state potential energy function of a beryllium dimer determined using the single-reference coupled-cluster approach, Physical Chemistry Chemical Physics 13 (45) (2011) 20311. doi:10.1039/c1cp22417d.

[143] A. V. Mitin, Unusual chemical bonding in the beryllium dimer and its twelve vibrational levels, Chemical Physics Letters 682 (2017) 30–33. doi:10.1016/j.cplett.2017.05.071.

[144] V. V. Meshkov, A. V. Stolyarov, M. C. Heaven, C. Haugen, R. J. LeRoy, Direct-potential-fit analyses yield improved empirical potentials for the ground $X^1\Sigma_g^+$ state of Be_2, The Journal of Chemical Physics 140 (6) (2014) 064315. doi:10.1063/1.4864355.

[145] M. Lesiuk, M. Przybytek, J. G. Balcerzak, M. Musiał, R. Moszynski, Ab initio potential energy curve for the ground state of beryllium dimer, Journal of Chemical Theory and Computation 15 (4) (2019) 2470–2480. doi:10.1021/acs.jctc.8b00845.

[146] S. G. Porsev, A. Derevianko, High-accuracy calculations of dipole, quadrupole, and octupole electric dynamic polarizabilities and van der waals coefficients C_6, C_8, and C_{10} for alkaline-earth dimers, Journal of Experimental and Theoretical Physics 102 (2) (2006) 195–205. doi:10.1134/s1063776106020014.

[147] X. W. Sheng, X. Y. Kuang, P. Li, K. T. Tang, Analyzing and modeling the interaction potential of the ground-state beryllium dimer, Physical Review A 88 (2) (2013) 022517. doi:10.1103/physreva.88.022517.

[148] A. V. Mitin, A. A. Gusev, G. Chuluunbaatar, O. Chuluunbaatar, S. I. Vinitsky, V. L. Derbov, H. L. Luong, Dual nature of chemical bond and vibration-rotation spectrum of the Be_2 molecule in the ground $X^1\Sigma_g^+$ state, Chemical and Materials Sciences: Research Findings 2 (2025) 100–133. doi:10.9734/bpi/cmsrf/v2/4945.

[149] J. M. Merritt, V. E. Bondybey, M. C. Heaven, Beryllium dimer-caught in the act of bonding, Science 324 (5934) (2009) 1548–1551. doi:10.1126/science.1174326.

[150] A. A. Gusev, O. Chuluunbaatar, S. I. Vinitsky, A. G. Abrashkevich, KANTBP 3.0: New version of a program for computing energy levels, reflection and transmission matrices, and corresponding wave functions in the coupled-channel adiabatic approach, Computer Physics Communications 185 (12) (2014) 3341–3343. doi:10.1016/j.cpc.2014.08.002.

[151] V. I. Kukulin, V. M. Krasnopol'sky, J. Horáček, Theory of Resonances, Springer Netherlands, 1989. doi:10.1007/978-94-015-7817-2.

[152] A. J. F. Siegert, On the derivation of the dispersion formula for nuclear reactions, Physical Review 56 (8) (1939) 750–752. doi:10.1103/physrev.56.750.

[153] M. L. Goldberger, K. M. Watson, Collision Theory, John Wiley, New York, 1964.

[154] K. A. Walsh, Beryllium Chemistry and Processing, ASM International, 2009. doi:10.31399/asm.tb.bcp.9781627082983.

[155] A. Allouche, C. Linsmeier, Quantum study of tungsten interaction with beryllium (0001), Journal of Physics: Conference Series 117 (2008) 012002. doi:10.1088/1742-6596/117/1/012002.

[156] A. Lasa, D. Dasgupta, M. J. Baldwin, M. A. Cusentino, P. Hatton, D. Perez, B. P. Uberuaga, L. Yang, B. D. Wirth, Assessment of the literature about Be-W mixed material layer formation in the fusion reactor environment, Materials Research Express 11 (3) (2024) 032002. doi:10.1088/2053-1591/ad2c3c.

[157] V. M. Shabaev, I. I. Tupitsyn, V. A. Yerokhin, G. Plunien, G. Soff, Dual kinetic balance approach to basis-set expansions for the Dirac equation, Physical Review Letters 93 (13) (2004) 130405. doi:10.1103/physrevlett.93.130405.

[158] W. Schwarz, H. Wallmeier, Basis set expansions of relativistic molecular wave equations, Molecular Physics 46 (5) (1982) 1045–1061. doi:10.1080/00268978200101771.

[159] W. Kutzelnigg, Basis set expansion of the Dirac operator without variational collapse, International Journal of Quantum Chemistry 25 (1) (1984) 107–129. doi:10.1002/qua.560250112.

[160] S. P. Goldman, Variational representation of the Dirac-Coulomb Hamiltonian with no spurious roots, Physical Review A 31 (6) (1985) 3541–3549. doi:10.1103/physreva.31.3541.

[161] J. D. Talman, Minimax principle for the Dirac equation, Physical Review Letters 57 (9) (1986) 1091–1094. doi:10.1103/physrevlett.57.1091.

[162] A. Kolakowska, J. D. Talman, K. Aashamar, Minimax variational approach to the relativistic two-electron problem, Physical Review A 53 (1) (1996) 168–177. doi:10.1103/physreva.53.168.

[163] A. Kolakowska, Application of the minimax principle to the Dirac-Coulomb problem, Journal of Physics B: Atomic, Molecular and Optical Physics 29 (20) (1996) 4515–4527. doi:10.1088/0953-4075/29/20/010.

[164] L. LaJohn, J. D. Talman, Variational solution of the single-particle Dirac equation in the field of two nuclei using relativistically adapted slater basis functions, Theoretical Chemistry Accounts: Theory, Computation, and Modeling (Theoretica Chimica Acta) 99 (5) (1998) 351–356. doi:10.1007/s002140050346.

[165] G. Chuluunbaatar, Computational schemes for solving quantum-mechanical problems, Candidate thesis, Peoples' Friendship University of Russia, Moscow, (in Russian) (2022).

[166] J. L. Zhou, A. L. Tits, User's guide for FFSQP Version 3.5: A Fortran code for solving constrained nonlinear minimax optimization problems, generating iterates satisfying all inequality and linear constraints (1992).

[167] L. Adolphs, H. Daneshmand, A. Lucchi, T. Hofmann, Local saddle point optimization: A curvature exploitation approach, Proceedings of the Twenty-Second International Conference on Artificial Intelligence and Statistics 89 (2019) 486–495.

[168] W. Johnson, K. Cheng, M. Chen, Accurate relativistic calculations including qed contributions for few-electron systems, Relativistic Electronic Structure Theory - Part 2. Applications 14 (2004)

120–187. doi:10.1016/s1380-7323(04)80030-x.

[169] O. Chuluunbaatar, B. B. Joulakian, G. Chuluunbaatar, J. Buša Jr., G. O. Koshcheev, Accurate calculations for the Dirac electron in the field of two-center Coulomb field: Application to heavy ions, Chemical Physics Letters 784 (2021) 139099. doi:10.1016/j.cplett.2021.139099.

[170] I. I. Tupitsyn, D. V. Mironova, Relativistic calculations of ground states of single-electron diatomic molecular ions, Optics and Spectroscopy 117 (3) (2014) 351–357. doi:10.1134/s0030400x14090252.

[171] V. D. Lakhno, I. V. Amirkhanov, A. V. Volokhova, E. V. Zemlyanaya, I. V. Puzynin, T. P. Puzynina, V. S. Rikhvitskii, M. V. Bashashin, Dynamic model of the polaron for studying electron hydration, Physics of Particles and Nuclei 54 (5) (2023) 869–883. doi:10.1134/s1063779623050167.

[172] A. Friesen, Y. Kalinovsky, A. Khmelev, Mesons in nonlocal model with four-dimensional separable kernel, The European Physical Journal A 62 (1) (2026) article number 6. doi:10.1140/epja/s10050-025-01772-6.

[173] I. V. Barashenkov, D. E. Pelinovsky, E. V. Zemlyanaya, Vibrations and oscillatory instabilities of gap solitons, Physical Review Letters 80 (23) (1998) 5117–5120. doi:10.1103/physrevlett.80.5117.

[174] I. V. Barashenkov, E. V. Zemlyanaya, Oscillatory instabilities of gap solitons: a numerical study, Computer Physics Communications 126 (1–2) (2000) 22–27. doi:10.1016/s0010-4655(99)00241-6.

[175] A. N. Vystavkin, Yu. F. Drachevskii, V. P. Koshelets, I. L. Serpuchenko, First observation of static bound states of fluxons in long Josephson junctions with inhomogeneities, Soviet Journal of Low Temperature Physics 14 (6) (1988) 357–358. doi:10.1063/10.0031962.

[176] A. Abrashkevich, I. V. Puzynin, CANM, a program for numerical solution of a system of nonlinear equations using the continuous analog of Newton's method, Computer Physics Communications 156 (2) (2004) 154–170. doi:10.1016/s0010-4655(03)00461-2.